NASA Contractor Report 4642

Development of a Multicomponent Force and Moment Balance for Water Tunnel Applications, Volume I

Carlos J. Suárez, Gerald N. Malcolm, Brian R. Kramer,
Brooke C. Smith, Bert F. Ayers
Eidetics International, Inc.
Torrance, California

Prepared for
NASA Dryden Flight Research Center
Contract NAS2-13571

National Aeronautics and
Space Administration

Office of Management

Scientific and Technical
Information Program

1994

Use of trade names or names of manufacturers in this report does not constitute an official endorsement of such products or manufacturers, either expressed or implied, by the National Aeronautics and Space Administration.

TABLE OF CONTENTS

LIST OF FIGURES

ABSTRACT

The principal objective of this research effort was to develop a multicomponent strain gauge balance to measure forces and moments on models tested in flow visualization water tunnels. An internal balance was designed that allows measuring normal and side forces, and pitching, yawing and rolling moments (no axial force). The five-components to applied loads, low interactions between the sections and no hysteresis. Static experiments (which are discussed in this Volume) were conducted in the Eidetics water tunnel with delta wings and a model of the F/A-18. Experiments with the F/A-18 model included a thorough baseline study and investigations of the effect of control surface deflections and of several Forebody Vortex Control (FVC) techniques. Results were compared to wind tunnel data and, in general, the agreement is very satisfactory. The results of the static tests provider confidence that loads can be measured accurately in the water tunnel with a relatively simple multi-component internal balance. Dynamic experiments were also performed using the balance, and the results are discussed in detail in Volume II of this report.

NOMENCLATURE

A_{ref}	Reference wing area
b	Wing span
Co	Root chord
$\bar{c}$	Mean aerodynamic chord
YM_1	Yawing moment section #1
YM_2	Yawing moment section #2
PM_1	Pitching moment section #1
PM_2	Pitching moment section #2
RM	Rolling moment section
LP	Load point
α	Angle of attack
β	Sideslip angle
ϕ	Roll angle
Q_∞	Free stream dynamic pressure
V_∞	Free stream velocity
Re	Reynolds number
C_N	Normal force coefficient
C_m	Pitching moment coefficient (body axis)
C_Y	Side force coefficient (body axis)
C_n	Yawing moment coefficient (body axis)
C_l	Rolling moment coefficient (body axis)
$CY\beta$	$\frac{\partial CY}{\partial \beta}$
$Cn\beta$	$\frac{\partial Cn}{\partial \beta}$
$Cl\beta$	$\frac{\partial Cl}{\partial \beta}$
ΔC_n	Increment in yawing moment coefficient
ΔC_l	Increment in rolling moment coefficient
δr	Rudder deflection (+, trailing edge left)
δa	Aileron deflection (+, right aileron up, left aileron down)
C_μ	Blowing coefficient $= \frac{\dot{m}\ Vj}{Q_\infty\ Aref}$
$\dot{m}$	Mass flow rate of the blowing jet
V_j	Exit velocity of the blowing jet
Φ	Strake angle (from the windward meridian)
$\Delta\Phi$	Separation angle between dual strakes
LEX	Leading edge extension
LFV	Left forebody vortex
RFV	Right forebody vortex

DEVELOPMENT OF A MULTI-COMPONENT FORCE AND MOMENT BALANCE FOR WATER TUNNEL APPLICATIONS

Volume I - Balance Description and Static Water Tunnel Tests

1.0 INTRODUCTION

Water tunnels have been utilized in one form or another to explore fluid mechanics and aerodynamics phenomena since the days of Leonardo da Vinci. Many studies (Refs. 1-6) have shown that the flow fields and the hydrodynamic forces in water tunnels are equivalent to the aerodynamic flow fields and forces for models in wind tunnels for the incompressible flow regime (i.e., Mach numbers less than 0.3). Only in recent years, however, have water tunnels been recognized as highly useful facilities for critical evaluation of complex flow fields on many modern vehicles such as high performance aircraft. In particular, water tunnels have filled a unique role as research facilities for understanding the complex flows dominated by vortices and vortex interactions. Flow visualization in water tunnels provides an excellent means for detailed observation of the flow around a wide variety of configurations. The free stream flow and the flow field dynamics are low-speed, allowing real-time visual assessment of the flow patterns using a number of techniques including dye flow through ports in the model, hydrogen bubble generation from strategic locations on the model, laser light sheet illumination with fluorescent or opaque dyes, etc.

Water tunnel testing is attractive because of the relatively low cost and quick turn-around time to perform experiments and evaluate the results. Models are relatively inexpensive (compared to wind tunnel models) and can be built and modified as needed in a relatively short time period. The response of the flow field to changes in model geometry can be directly assessed in water tunnel experiments with flow visualization. Detailed flow visualization also is an excellent means of understanding the physics of the flow. Understanding the flow structure and how the flow field interacts with the aircraft surfaces is extremely valuable in making configuration changes to solve specific aerodynamic problems. While flow visualization is very valuable and is the primary reason for the existence of water tunnels, there are some limitations, as there are for all experimental facilities.

One of the principal limitations of a water tunnel is that the low flow speed, which provides for detailed visualization, also results in very small hydrodynamic (aerodynamic) forces on the model, which, in the past, have proven to be difficult to measure accurately. In most cases where force and moment information is essential, wind tunnel tests (usually with a different model) eventually have to be performed. The advent of semi-conductor strain gauge technology and devices associated with data acquisition such as low-noise amplifiers, electronic filters, and digital recording has made accurate measurements of very low strain levels feasible. If the water tunnel could also determine forces and moments to some level of accuracy simultaneously with the flow visualization, there would be a definite saving in time and cost in the selection and creation of the proper model to be constructed for sub-scale wind tunnel tests. Knowledge of the cause and effect of the complex flows and resulting non-linear aerodynamics at high angles of attack requires the capability to correlate what we see with what we measure in terms of airframe loads.

In addition to static force and moment measurements, the water tunnel force/moment balance may also provide a capability for dynamic measurements. The high flow speed typical of wind tunnel tests requires rapid movement of the model in order to simulate a properly scaled dynamic maneuver and the motions are mechanically difficult to implement. The fast model movement also places demanding requirements on the response of the data acquisition system to acquire data at high sample rates. In contrast, the flow speed of water tunnel tests is typically much lower (two orders of magnitude or more), and consequently, the model motion required to

simulate a dynamic maneuver is also very slow. Thus the response rates for data acquisition required for force and moment measurements during transient and dynamic situations are less demanding than in a wind tunnel.

The Phase I of this SBIR contract showed promising results with a three-component water tunnel balance, and therefore, the effort to develop, construct, and test a multi-component water tunnel balance was clearly justified. This final report, which is divided into two Volumes, summarizes the results of the Phase II research program. Volume I provides a detailed description of the balance, calibration procedures and data acquisition/reduction hardware and software, and discusses results of the calibration and of the static water tunnel tests performed on different models. Volume II describes the improvements in the water tunnel model support required to perform dynamic tests (computerized motions, new roll mechanism, rotary balance rig, etc.) and presents the results of several dynamic experiments.

2.0 REVIEW OF PHASE I RESULTS

The accomplishments of the Phase I research program and the recommendations for a Phase II program were reviewed and discussed in Ref. 7. A brief summary is presented in the following section as a background for the Phase II work.

2.1 BALANCE DESIGN AND CALIBRATION

A three-component water tunnel balance was design, built, calibrated and tested during the Phase I contract. The balance allows for simultaneous measurement of normal force, pitching moment and rolling moment (or, by rolling the balance 90° in the model, side force, yawing moment and rolling moment). The criteria used in the design was focused on obtaining a configuration with great flexibility and simplicity. It is highly desirable to be able to change configurations and the location of the individual components until the best or optimum location is found. Because of this, the idea of an integral balance was discarded. Also, the balance needed to be small in order to be accommodated inside a typical water tunnel model, that in general is smaller than a wind tunnel model.

The balance consisted of two pitching moment sections and one rolling moment section that can be assembled in different ways (Fig. 1). The measurement of two pitching moments permits calculating the pitching moment and the normal force at the reference point. Since the forces that are measured in a water tunnel are very small, semi-conductor strain gages were used. These gages are very sensitive, with gage factors (change in resistance with strain) between 100 and 150.

After the gages were bonded and the circuit (full Wheatstone bridge per section) was wired, the sections were completely covered with a silicon-rubber type material for water-proofing. When the balance was assembled and all the wires were in place, another layer of this material was applied to ensure that the balance could operate under water.

The balance was calibrated using a rig that permitted loading the balance at different locations and orientations, both with single and combined loads. The first task in the calibration was to apply a pure normal force, and readings from the three channels were recorded. The balance was later rotated 180°, and a negative pure normal force calibration was performed in the same manner. After this, the rolling moment section was calibrated. Results of the calibration of the primary gages can be seen in Fig. 2. The plots in Figs. 2a and 2b show the response of Channel 1 and Channel 2 (pitching moment sections) to the application of a pitching moment. Figure 2c shows the output of Channel 3 (torque section) in response to the application of a rolling moment. The data indicate very good linearity and a sensitivity of approximately 320 grams-cm/Volt (0.28 in-lb/Volt). As a result of the small forces generated in the water tunnel, the

interactions or errors caused by mechanical slippage or relative misalignment of the balance parts are negligible. In general, all interactions were found to be very small.

2.2 FORCE/MOMENT MEASUREMENT RESULTS

All experiments were conducted in the Eidetics 2436 Flow Visualization Water Tunnel. Most of the force measurements were performed at a flow speed of 7.6 cm/sec (0.25 ft/sec), corresponding to a Reynolds number of about 69,000/m (21,000/ft), and the data were filtered using a low pass filter (0.05 Hz). A 70° delta wing was used for all the tests. Only selected results will be discussed in this section to show the performance of the balance. Figure 3 presents normal force and pitching moment data for an angle of attack sweep at $\beta = 0°$. The normal force results compared very well to wind tunnel data (Ref. 9) at low angles of attack; however, some differences are seen at higher angles of attack (between 25° and 40°). The pitching moment curves, despite some differences in magnitude, present similar trends. Several factors, other than balance design, could have influenced the results, such as model differences (different leading edge bevel and fairings), uncertainties in dynamic pressure or angle of attack measurements, corrections applied, Reynolds number, etc.

Results of β sweeps at different angles of attack are presented in Fig. 4. The purpose of these β sweeps was to obtain a change in rolling moment to check the rolling moment gage (Channel 3). Figures 4a, b, c, and d show rolling moment coefficient at $\alpha = 0°$, 10°, 20° and 30°, respectively. Trends compared very well with wind tunnel data from Ref. 9, but some differences in magnitude are observed again, especially at $\alpha = 20°$ and 30°. In general, results can be considered to be quite acceptable. It is important to notice that discrepancies were also found among the wind tunnel data, with differences of up to 20% for the same delta wing tested in different tunnels or at different scales.

2.3 CONCLUDING REMARKS (PHASE I)

Results of the Phase I of this research effort demonstrated clearly the potential of developing a multi-component force and moment balance for application in water tunnels. The calibration of the three-component balance revealed good linearity in the primary gauges and low component interactions. Experiments on 70° delta wings showed a satisfactory agreement to wind tunnel data; therefore, force/moment measurements in a water tunnel were further explored and developed during the Phase II of this contract.

3.0 PHASE II TECHNICAL OBJECTIVES AND APPROACH

The overall objective of the Phase II research program was to design, develop and test a five-component force and moment strain gauge balance and perform both static and dynamic experiments to verify its performance. In addition to the basic balance, a complete calibration system and data acquisition hardware and software were developed and integrated. The balance needed to be capable of measuring forces and moments on 3-dimensional aircraft models that are sting mounted from the rear, similar to typical wind tunnel mounting techniques. Of special interest during this phase of the contract was the use of the balance to perform dynamic experiments, including rotary balance tests. The Eidetics water tunnel model support system, which had the capability for model motions in pitch and yaw, was expanded to perform high-fidelity dynamic motions in three axes (pitch, yaw, and roll). A roll mechanism and a rotary rig were designed and built, and the existing motors and electronics of the model support were improved. The unique capability of performing simultaneous force measurements and flow visualization during dynamic situations was of primary importance in this project.

The long-term goal of the contract was to assemble and demonstrate a complete and stand-alone force/moment data acquisition system in the Eidetics water tunnel for static and dynamic water tunnel tests. To accomplish this, the specific technical objectives of the proposed program were the following:

1. Design and build a 5-component force/moment balance compatible with Eidetics water tunnel or similar.

2. Design and build a suitable calibration rig and related hardware and software to perform an accurate balance calibration.

3. Design, purchase and assemble the necessary data acquisition system components to acquire and process the data into engineering units for display, printing and plotting. Write the required software to process, display and plot the balance data and reduced aerodynamic coefficients along with the model position and motion time history as required.

4. Perform static force and moment measurements on generic configurations (delta wings) and on an F/A-18 model, and compare results to existing wind tunnel data.

5. Increase the test capability of the Eidetics water tunnel model support system from the present two axes of motion (pitch and yaw) to three axes (including roll) and modify the model support drive control system to produce high-resolution motions in all three axes to acquire "dynamic" force and moment time-history data.

6. Develop a technique for conducting dynamic tests. Perform tests using the same models and measure time-lag response of the forces and moments to forced motions such as high-amplitude pitch-ups and body-axis roll. If possible, perform and display flow visualization and force measurements simultaneously.

7. Develop an apparatus for producing a "coning" motion, or a roll motion about the velocity vector with fixed angle of attack and sideslip, commonly performed in wind tunnel tests on a rotary-balance apparatus. Perform tests on the F/A-18 model to evaluate the test capability and compare the results to the rotary-balance data on the F/A-18 obtained by Eidetics in the Ames 7 x 10-ft wind tunnel under another SBIR Phase II contract.

The approach to develop the test capabilities outlined in the specific objectives focused on designing, building, assembling and testing a complete operational system that is tailored to the needs of a typical water tunnel user. The balance and data acquisition system were designed to be as versatile as possible in order to accommodate a wide variety of water tunnel applications. The main goal was to be able to provide a complete balance and data acquisition system that the user can install in his/her water tunnel facility without having to commit significant time and money to make it operational. The balance and the calibration equipment are the heart of the system; the remaining components, consisting of the appropriate signal conditioning and amplifying equipment, data acquisition hardware, and desktop computer are available off-the-shelf. A complete and user-friendly software package to process the balance and tunnel-related information was developed using LabView, a popular and widely used graphical programming language. All the improvements to the model support and hardware designed and built to conduct the dynamic tests, despite being customized for the Eidetics water tunnel, can be slightly modified and adapted for use in any other tunnel.

A five-component balance, a calibration rig and a copy of the data acquisition/reduction software are delivered to NASA-Dryden along with this final report. Again, discussions related to

the first four objectives are presented in this volume. Results of this research effort regarding the dynamic tests in objectives 5-7 are the main subjects of Volume II of this final report.

4.0 BALANCE DESCRIPTION

The basic concept for the five-component balance design was to make each of the components as separate elements that can be added or subtracted from the integral balance. This approach provides the capability of removing individual gauge elements without having to replace the entire balance. Specific elements may be desired to be changed because of damage, to change sensitivity or load capacity, or to change the spacing between the gauges. In addition to its versatility, the construction of the balance is simplified by machining separate sections as opposed to machining all of the elements into a one-piece chassis, saving time and cost in the manufacture of the balance.

4.1 MECHANICAL DESIGN

Data obtained in previous water tunnel tests, especially during the Phase I contract, and generic data from wind tunnel tests were used to get an estimation of the forces and moments that could be expected. Aerodynamic loads on typical water tunnel models were calculated, and the results were used to determine the strain level required to obtain the desired sensitivity. Moments of inertia and stress levels were calculated for different cross-sections and sizes, until an "optimum" section was found. This "optimum" section was defined as one that will provide the desired sensitivity and resolution when loaded in a particular plane and that will show stiffness in the other planes, therefore maximizing output and minimizing component interaction. The design approach for the five-component balance is basically the same as for the three-component balance tested in Phase I.

The balance consists of a rolling moment section, two pitching moment sections and two yawing moment sections, all 1.91 cm (3/4") in diameter. Five components will provide for the simultaneous measurement of pitching, yawing and rolling moments, and normal and side forces. Additional balance components include: sting and model adapters and spacers (Fig. 5). The moment of inertia of each section was carefully calculated in order to obtain the required stress levels that produce the desired sensitivity and resolution when the balance is loaded in the plane of interest and maximum stiffness in the other planes. All the balance components are machined from stainless steel 17-4. Each component is attached to the next by means of two 4-40 screws, and two location pins ensure the perfect alignment between components. Photographs of the balance are shown in Figs. 6 and 7.

4.1.1 Rolling Moment Section

The rolling moment component has a cruciform cross-section with four rectangular beams (two vertical and two horizontal). A notch was cut at the center of each beam to accommodate the gages; one gage was located at each beam, two in compression and two in tension. The gages were bonded at 45° with respect to the longitudinal axis of the beam because the maximum stress on the surface due to a change in torque occurs in this direction. This cruciform section is very sensitive to changes in torque, while providing stiffness when the moment is applied in the x-z or x-y planes.

4.1.2 Pitching Moment Section

This section is the most complicated of all the components because it has to provide sensitivity in the x-y plane and, at the same time, support the model weight, which also acts mostly on the x-y plane. Even though water tunnel models are usually small, the weight of these models

can be significantly greater than the aerodynamic force that is going to be measured. The gauges are located on two thin beams, offset from the centerline. The beams are thin enough to provide the required sensitivity, while the offset from the centerline increases the moment of inertia and thus the stiffness of the section in the x-y plane.

4.1.3 Yawing Moment Section

The yawing moment section has a rectangular (vertical) cross-section along the centerline in order to provide stiffness in the x-y plane and maximum sensitivity in the x-z plane. Two strain gauges are located on the left face of the beam, while the other two are on the right face. All the balance components have an inner hole, and all the wires coming from the gauges are routed through that hole.

4.1.4 Spacers

The spacers can be used in case the distance between the two pitching or yawing moment sections is not large enough to resolve the normal or side forces accurately. Also, they provide flexibility in the configuration of the balance. For the specific models and experiments conducted in this program, the spacers were not necessary, and therefore, they were not used.

4.1.5 Sting and Model Adapters

These two pieces complete the design and allow to attach the balance to the model and to the sting and C-strut in the water tunnel model support.

4.2 STRAIN GAUGES

Semi-conductor strain gauges are used to get the desired output, since they are widely acknowledged as being outstanding transduction devices. The change in resistance per unit applied strain results in an output of 50 to 100 times that of either wire or foil strain gauges. The resulting milli-Volt output in a typical transducer offers improved signal-to-noise ratios and reduced cost of signal conditioning. The gauges chosen for this project are PSI-TRONIX 1000 Ω gauges with a gage factor (GF) of 145. They are very small in size, only 0.08 cm (0.03") wide by 0.4 cm (0.16") long. Each bridge is composed of four gages, and of some standard resistors added externally. These resistors are used to compensate for differences in the strain gauge resistance and to compensate for temperature changes. The values of the resistors vary for each of the sections and are specified by the gauging company after extensive tests. Since the gauges are re-zeroed before each run, and since the temperature changes during a typical water tunnel run are almost negligible, temperature compensation for this application is not very critical.

The gauges are connected using the full Wheatstone bridge shown in Fig. 8. Five wires come from each balance section. The red and black wires are positive and negative input, respectively, while the green and white wires are positive and negative output. A 100 Ω potentiometer is connected between the black and yellow leads to balance the bridge externally. This is used when the internal potentiometer of the signal conditioner is not enough to produce a zero reading under specific loading conditions. All wires are routed through the balance inner hole, and they come out at the two side holes of the sting adapter.

4.3 WATER PROOFING

The fact that the balance has to operate under water complicates the problem significantly, and different water proofing techniques had to be tested until the optimum was found. After the gauges, terminals and wires were in place, a thin layer of Microcrystalline Wax was applied over

the gauges and terminals. The wax is an excellent water barrier, but, since it is quite fragile, is not very good for mechanical protection. In order to protect the strain gauges and to seal all the wire/terminal connections, layers of RTV (silicon rubber) were applied over the wax, covering the entire area where the gauges and terminals are located. A very thin rubber sleeve was utilized as a secondary protection.

5.0 INSTRUMENTATION AND DATA ACQUISITION/REDUCTION SYSTEM

A typical data acquisition system consists primarily of signal conditioners, amplifiers, filters, and analog-to-digital signal conversion for each of the balance channels, plus the computer system and software required to acquire, store, display and manipulate the balance information.

5.1 INSTRUMENTATION

A multi-channel system for generating conditioned high-level signals from strain gauge inputs was used. The eight-channel system, seen in Fig. 9, is a MEASUREMENTS GROUP Model 2100 Strain Gauge Conditioner and Amplifier. Principal features of this unit include: independently variable and regulated excitation for each channel (0.5 to 12 Volts), fully adjustable calibrated gain from 1 to 2100, and a digital output display. During the calibration and most of the experiments, the excitation voltage was 5 Volts and the external gain was 200 in all channels.

Figure 9 also shows a box where all the 100 Ω external potentiometers are located. These are the "pots" used to balance each bridge when the internal potentiometer of the signal conditioner does not provide the required range. Resistors used for temperature and gauge resistance compensation are also located inside this box.

The output lines for each channel are routed both to the digital display of the signal conditioner and to the A/D board inside the Macintosh Quadra 700 computer (by means of a ribbon cable). The board is a National Instruments NB-MIO-16XL, which is a high-performance multi-function analog, digital and timing I/O board for Macintosh NuBus computers. Features of this board include: fast 16-bit ADC, 16 single-ended or 8 differential channels, programmable gains, guaranteed rates up to 55 ksamples/sec, etc.

5.2 DATA ACQUISITION/REDUCTION SOFTWARE

The electrical output from the balance and the accompanying signal conditioning and amplifier equipment must be processed with the information on the gauge calibration constants and the resulting engineering units (units of forces and moments and aerodynamic coefficients based on the tests conditions and the model geometry) must be displayed, stored, printed and plotted.

The software used in this project, developed specifically for this application, was written using National Instrument's LabView (Version 3.0). The goal was to provide software that is user friendly, easy to use and modify as needed for specific applications, and is versatile in its ability to reduce and display the balance and tunnel condition data efficiently and effectively. The basic methodology for the data reduction system, particularly the treatment of the balance equations, was initiated using the same approach used for typical wind tunnel data reduction schemes.

The data acquisition/reduction software allows to perform a full balance calibration, as well as the static and dynamic experiments. The main front panel of the program is seen in Fig. 10. A description of the features of each "sub-panel" is provided in different Sections of this report (where that particular software panel or feature is utilized).

6.0 BALANCE CALIBRATION

A key to accurately acquiring data from a force/moment balance is a precise and repeatable calibration. For a multi-component balance, it is important to determine the response of each section to a load in its primary plane of action (sensitivity) and also to loads in other planes (interactions). For example, the output from a pitching moment gage will depend not only on the direct application of a pitching moment (or a normal force) but will also respond to a rolling moment or a yawing moment input. The objective is to minimize these interactive load/response characteristics, but the expense of manufacturing a balance to the tolerance levels to approach zero interactions is not warranted since the interactions can now be accounted for quite easily on modern computers. Therefore, appropriate calibration hardware, software and procedures are essential to obtain the correct sensitivities and interactions.

6.1 CALIBRATION RIG

A simple calibration apparatus, shown in Fig. 11, was designed and built to calibrate the five-component balance. Basically, the rig consists of a main aluminum support where the sting mount and balance are attached. Pulleys on each side of the balance can be used to obtain accurate side forces and rolling moments. The pulley system permits the application of a pure rolling moment provided that low friction pulleys are used and the cables are perfectly aligned. Each pulley is mounted on a shaft between two bases that slide along a side rail. The bases can be also moved up and down, so the pulley can be accurately positioned to obtain the desired load. A loading fixture attached to the balance end is used to apply the weights. Two fiberglass rods allow positioning the weight pan at the different loading point locations. The loading fixture can be rotated to get the proper configuration according to the desired type of loading (Fig. 12). The balance can also be rotated; therefore, the required loading can be obtained either by rotating the balance or the loading fixture. Levels and stainless steel pins ensure the perfect alignment of the balance and the rig throughout the calibration process.

6.2 CALIBRATION PROCEDURE

Assume the balance is configured in the following manner:

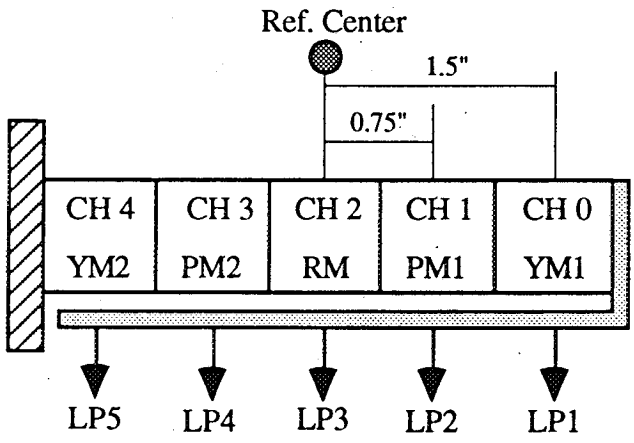

For this configuration, the calibration input matrix is presented as follows:

CALIBRATION INPUT MATRIX

$$\begin{bmatrix} YM1 \\ PM1 \\ RM \\ PM2 \\ YM2 \end{bmatrix} = \begin{bmatrix} \frac{\partial YM1}{\partial N} & \frac{\partial YM1}{\partial PM} & \frac{\partial YM1}{\partial S} & \frac{\partial YM1}{\partial YM} & \frac{\partial YM1}{\partial RM} \\ \frac{\partial PM1}{\partial N} & \frac{\partial PM1}{\partial PM} & \frac{\partial PM1}{\partial S} & \frac{\partial PM1}{\partial YM} & \frac{\partial PM1}{\partial RM} \\ \frac{\partial RM}{\partial N} & \frac{\partial RM}{\partial PM} & \frac{\partial RM}{\partial S} & \frac{\partial RM}{\partial YM} & \frac{\partial RM}{\partial RM} \\ \frac{\partial PM2}{\partial N} & \frac{\partial PM2}{\partial PM} & \frac{\partial PM2}{\partial S} & \frac{\partial PM2}{\partial YM} & \frac{\partial PM2}{\partial RM} \\ \frac{\partial YM2}{\partial N} & \frac{\partial YM2}{\partial PM} & \frac{\partial YM2}{\partial S} & \frac{\partial YM2}{\partial YM} & \frac{\partial YM2}{\partial RM} \end{bmatrix} \bullet \begin{bmatrix} N \\ PM \\ S \\ YM \\ RM \end{bmatrix}$$

N = Normal Force [lbs] S = Side Force [lbs]
PM = Pitching Moment at Ref. Center [in-lbs]
YM = Yawing Moment at Ref. Center [in-lbs]
RM = Rolling Moment at Ref. Center [in-lbs]

$\frac{\partial()}{\partial()}$ = [Volts/lbs or Volts/in-lbs]

PM_1, PM_2, YM_1, YM_2 and RM = Gage Readings [Volts]

In order to obtain the coefficients of the matrix in a systematic manner, the following procedure, developed specifically for this balance, is utilized:

1) Load the balance in the N(+) direction at the 5 load points. For each gauge, the following curves will be obtained (linear curve fit when possible):

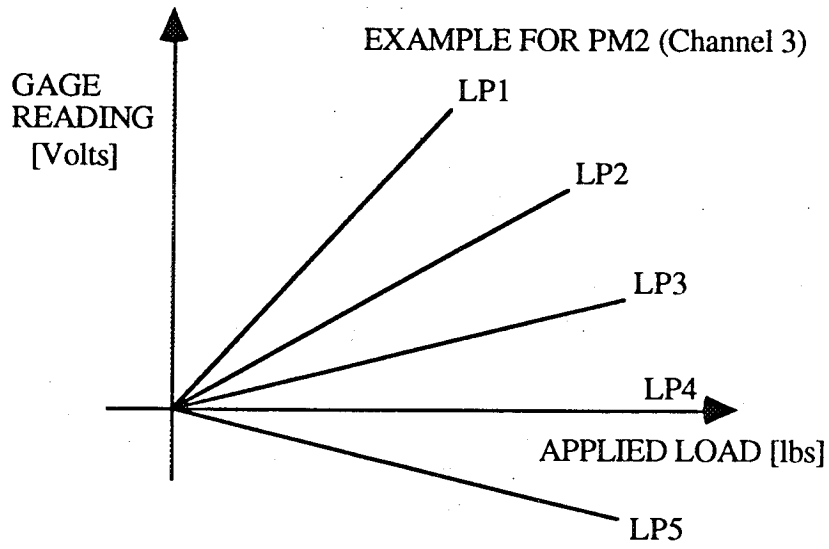

2) Load the balance in the N(-) direction at the 5 load points. Obtain the same curves for each gauge as in the N(+) case:

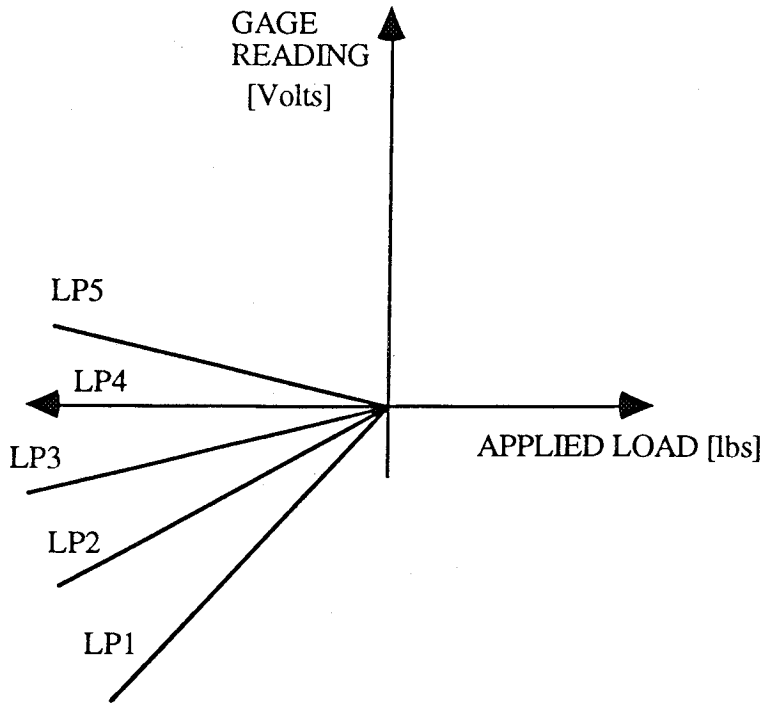

3) Find the average slope between the positive and negative loading for each of the curves (LP1-5).

4) Plot the slope of each of the average curves versus load point distance from the Reference Center (LP3 is at the Ref. Center):

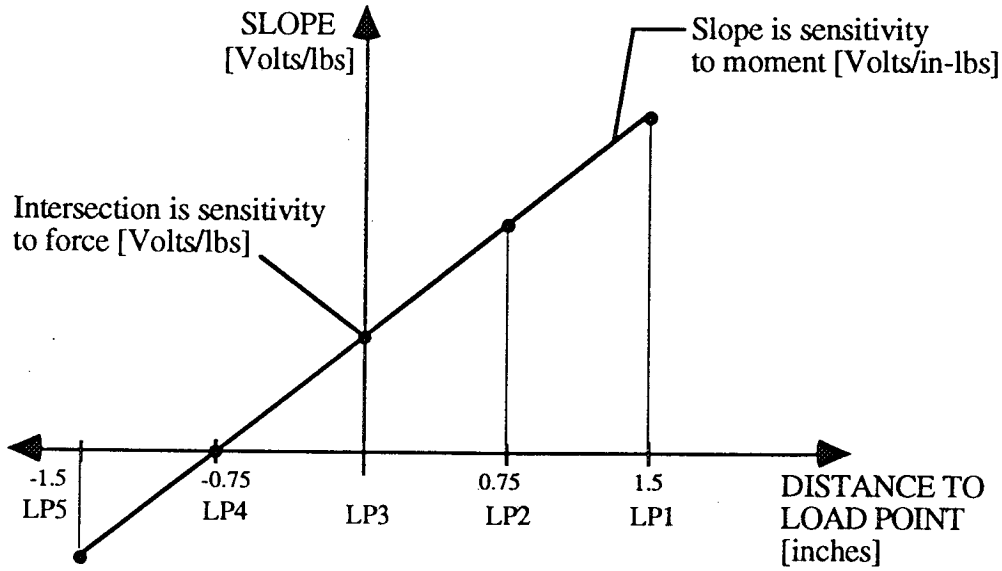

5) These two loading cases allow obtaining the coefficients of the first two columns of the calibration input matrix, i.e., the y-intercepts of the curves corresponding to each channel generate the first column, while the slopes of said curves generate the second column.

6) Load the balance in the S(-) and S(+) directions. Determine the same curves as in the previous cases; the side force loading will yield the coefficients for the third and fourth columns of the calibration input matrix.

7) Load the balance with a RM(+) at LP3 (Ref. Center). Obtain the following curve (using a linear curve fit):

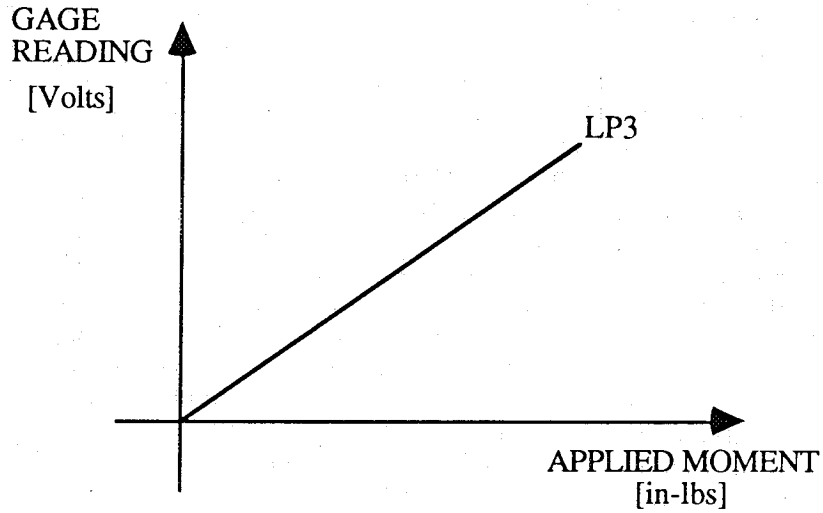

8) Load the balance with a RM(-), repeat step (7). Each sensitivity and interaction coefficient (last column of the matrix) will be the average of (7) and (8).

9) When all the coefficients have been determined, invert the matrix. The following output calibration matrix, which allows for calculating forces and moments (engineering units) from gage readings [Volts] is obtained:

OUTPUT CALIBRATION MATRIX

$$\begin{bmatrix} N \\ PM \\ S \\ YM \\ RM \end{bmatrix} = \begin{bmatrix} \frac{\partial N}{\partial YM1} & \frac{\partial N}{\partial PM1} & \frac{\partial N}{\partial RM} & \frac{\partial N}{\partial PM2} & \frac{\partial N}{\partial YM2} \\ \frac{\partial PM}{\partial YM1} & \frac{\partial PM}{\partial PM1} & \frac{\partial PM}{\partial RM} & \frac{\partial PM}{\partial PM2} & \frac{\partial PM}{\partial YM2} \\ \frac{\partial S}{\partial YM1} & \frac{\partial S}{\partial PM1} & \frac{\partial S}{\partial RM} & \frac{\partial S}{\partial PM2} & \frac{\partial S}{\partial YM2} \\ \frac{\partial YM}{\partial YM1} & \frac{\partial YM}{\partial PM1} & \frac{\partial YM}{\partial RM} & \frac{\partial YM}{\partial PM2} & \frac{\partial YM}{\partial YM2} \\ \frac{\partial RM}{\partial YM1} & \frac{\partial RM}{\partial PM1} & \frac{\partial RM}{\partial RM} & \frac{\partial RM}{\partial PM2} & \frac{\partial RM}{\partial YM2} \end{bmatrix} \bullet \begin{bmatrix} YM1 \\ PM1 \\ RM \\ PM2 \\ YM2 \end{bmatrix}$$

6.3 CALIBRATION SOFTWARE

The calibration software, part of the general data acquisition/reduction software, handles the entire calibration procedure. After all the different loading cases are performed, the program analyzes and curve fits the data and automatically provides the output matrix.

The calibration software is selected by clicking on the "Calibrate Balance" button of the main panel. Different features included in the calibration sub-panel can be seen in Fig. 13a. By opening the "Data Acquisition Setup" panel, the user can specify the order of the balance channels, the NuBus slot used in the computer, and the sampling number and rate. The "Balance and Load Fixture Geometry" button is utilized to specify the location of the strain gauges and of the load points (measured from the front of the balance). A "Monitor" front panel permits checking the five channels on-line to verify that the appropriate signals are being acquired. A "Load Balance" front panel is used to acquire and record the data. In order to perform the calibration, the user starts selecting the type of loading, for example, positive normal force at Load Point 1. The balance is loaded (the weight applied, in grams, is a keyboard input) and data are acquired at the specified rate (for this calibration, 100 samples/sec for 25 seconds which gives 500 samples/channel). The program averages the data for each channel and writes the information to the appropriate data file. After all the loading cases are completed, the user has to go to the "Process Calibration" panel, which is illustrated in Fig. 13b. The first step for processing the calibration is to load the data files ("Load Data Files" button) obtained for the different calibration cases. Once the files are loaded, the "Graph Data" panel is used to curve fit each of the plots with a linear curve fit. The "Build New Matrix" button is later utilized to automatically obtain the calibration input and output matrices, following the standard procedure discussed in the previous section. Also included in this section are two additional panels; the "Load Old Matrix" allows loading an already existing matrix from a previous calibration. A calibration matrix has to always be specified when the software is loaded, thus this particular panel has to be run at the beginning of each test. The "Calc. Check Case" button permits obtaining engineering units from a particular calibration data file. This feature is very useful to perform "check loads", i.e., apply a known weight and check if the calibration matrix is properly converting raw voltage into engineering units.

Inputs for this section of the software include:

- Balance Configuration:
  CHANNEL 0 = YM_1
  CHANNEL 1 = PM_1
  CHANNEL 2 = RM
  CHANNEL 3 = PM_2
  CHANNEL 4 = YM_2

- Distances from front of the balance to gauges:
  LP1 = 0.3875 in.
  LP2 = 1.1375 in.
  LP3 = 1.8875 in.
  LP4 = 2.6375 in.
  LP5 = 3.3875 in.

- Distances from front of the balance to load points:
  LP1 = 0.3625 in.
  LP2 = 1.1375 in.
  LP3 = 1.8875 in.
  LP4 = 2.6375 in.
  LP5 = 3.3875 in.

- Loading Fixture Moment Arm: 0.984 in.
- Balance Reference Center: 1.8875 in.

The load schedules used in this calibration were the following:

- Pitching and Yawing Moment (at each load point): 1, 3, 5, 10, 20, 30, 50, 100, 200 grams
- Rolling Moment (at LP3): 2, 6, 16, 36, 56, 96 grams

6.4 CALIBRATION RESULTS

A calibration was performed using the calibration rig, procedures and software described in the previous sections. The balance was loaded at the five load points with positive and negative normal and side forces, and at the Ref. Center (LP3) with positive and negative rolling moments.

Examples of selected loading cases are presented in Figs. 14a and 14b for normal and side force loading, respectively. Figure 14a shows the response of the five channels to a normal force applied at LP4. As expected, the largest response is seen in Channel 1, the most forward pitching moment section (PM1). Since the load is applied exactly at the location of the second pitching moment section (CH 3), this channel does not react to this particular loading. Interactions with the rolling moment gage are negligible, while the interactions with the two yawing moment gages are small. Figure 14b shows the signals from the five channels when a positive side force at LP3 (Ref. Center) is applied. Large linear responses are seen for CH 0 and CH 4 (the two yawing moment sections), while the interactions with the rest of the gages are negligible.

After all the loading cases are completed, the slopes of the output of each channel at the different load points are plotted versus the distance to said load points. Figure 15a shows one of these plots, in this case, the response of the pitching moment gages to an applied pitching moment. The slopes of the lines (approximately 0.0093 Volts/in-lb) are the sensitivity to pitching moment, while the y-intercepts are the sensitivity of these channels to a normal force. Figure 15b presents, in a similar manner, the sensitivity of the yawing moment gages to an applied yawing moment (0.026 Volts/in-lb).

In general, all the interactions were found to be very small. The largest interactions occur in the yawing moment gages under a pitching moment load and are shown in Fig. 16. As it can be seen, the interactions are small and quite linear.

The rolling moment calibration is presented in Fig. 17. Pure positive and negative rolling moments were applied at LP3, and the output at the gages in Volts is plotted versus moment for the five channels. The response of the rolling moment gage (CH 2) is linear, both for the positive and negative cases. The slope of this line represents the sensitivity of the section to rolling moment, i.e., -0.0097 Volts/in-lb (average of the slopes of the positive and negative loading cases). Interactions with the other gages are small.

After all the graphs were created, the software automatically builds the calibration input matrix. The matrix obtained in this particular calibration is the following:

$$\begin{bmatrix} YM1 \\ PM1 \\ RM \\ PM2 \\ YM2 \end{bmatrix} = \begin{bmatrix} -1.249E-3 & 7.242E-4 & -3.797E-2 & 2.653E-2 & 9.384E-5 \\ -6.756E-3 & 9.241E-3 & 2.384E-4 & -2.679E-4 & 5.059E-5 \\ 8.163E-5 & 4.456E-5 & 2.133E-4 & -3.561E-4 & -9.698E-3 \\ 6.973E-3 & 9.459E-3 & -3.821E-5 & -3.768E-4 & -1.561E-5 \\ 1.337E-3 & 8.934E-4 & 3.912E-2 & 2.665E-2 & 1.518E-4 \end{bmatrix} \bullet \begin{bmatrix} N \\ PM \\ S \\ YM \\ RM \end{bmatrix}$$

By inverting this matrix, the calibration output matrix is obtained. This matrix, which allows obtaining normal and side forces, and pitching, yawing and rolling moments from the readings in the five balance channels, is the following:

$$\begin{bmatrix} N \\ PM \\ S \\ YM \\ RM \end{bmatrix} = \begin{bmatrix} -0.128 & -73.669 & -0.495 & 71.946 & 0.398 \\ 0.799 & 54.248 & 0.214 & 52.609 & 0.496 \\ -12.998 & 2.355 & -0.093 & -2.527 & 12.929 \\ 19.064 & -1.577 & 0.469 & -1.669 & 18.513 \\ -0.983 & -0.261 & -103.131 & -0.853 & -0.390 \end{bmatrix} \bullet \begin{bmatrix} YM1 \\ PM1 \\ RM \\ PM2 \\ YM2 \end{bmatrix}$$

Hysteresis was also investigated to complete the calibration. The balance was loaded (open symbols in these plots) and then unloaded using the same increments (full symbols). All possible loading cases were investigated, i.e., positive and negative side and normal forces, and positive and negative rolling moments, but only selected cases are presented. Figure 18a shows the yawing moment sections (CH 0 and CH 4) under a negative side force load, and Fig. 18b reveals the response of the rolling moment gage to a negative rolling moment. As the plots indicate, no hysteresis effects are observed, with most of the points in the increasing load and decreasing load curves presenting almost the same values. Similar results were obtained for the other channels under primary loads.

7.0 STATIC WATER TUNNEL TESTS

Once the balance and the data acquisition/reduction system were developed, static force measurements were performed using different models, and the results were compared to existing wind tunnel data to assess the performance of the balance.

7.1 EXPERIMENTAL SETUP

7.1.1 Water Tunnel

All experiments were conducted in the Eidetics 2436 Flow Visualization Water Tunnel. The facility is a continuous horizontal flow tunnel with a test section 0.91 m (3 ft) high x 0.61 m (2 ft) wide x 1.83 m (6 ft) long. The tunnel speed can be varied from 0 to 30 cm/sec (1 ft/sec). The model is mounted inverted, and it is possible to test at angles of attack between 0° and 65°, and at sideslip angles between -25° and 25°.

7.1.2 Models

Flat plate delta wings with 70°, 76° and 80° sweep angles were used for these experiments. The extensive wind tunnel test data base (Refs. 8-13) on delta wings provided enough material for comparison. All delta wings, which are shown in Fig. 19, have a main chord of 38.1 cm (15"), have a double-beveled leading edge and are made of aluminum. The balance is located at the model centerline and the reference center is at the C/3 position, or 50% of the mean aerodynamic chord $\bar{c}$ ($\bar{c}$ is defined as 2/3C). Two fiberglass fairings (top and bottom) covered the entire balance.

Additional static experiments were performed on a 1/32nd-scale F/A-18 model. The plastic model, depicted in Fig. 20, is equipped with dye ports for flow visualization, and the balance is attached to an internal aluminum plate (moments are referenced to the 25% $\bar{c}$). The rudders and ailerons can be deflected, while the horizontal tails, flaps and leading edge flaps were fixed throughout the entire test at 0°, 0° and 34°, respectively. The nose section of the model is removable so that different Forebody Vortex Control (FVC) devices can be studied. The balance was used to assess the effect of these FVC techniques, and data were directly compared to the wind tunnel test data obtained by Eidetics on a similar configuration at the NASA Ames 7 x 10-ft tunnel. Two noses were tested in the F/A-18 model: one equipped with the ports for jet blowing and the other equipped with the mechanical FVC techniques (rotatable tip-strakes and a vertical nose strake). The jet blowing ports are located 1.73 cm from the tip of the model, at 150° azimuth from the windward meridian, and they are canted inboard 60° (Fig. 21a). The flow rate at each port is monitored with a volumetric flow meter to determine the blowing coefficient $C\mu$. This was the "optimum" jet blowing configuration found in the wind tunnel test [14]. The second nose has a rotatable tip, and both a single and a pair of strakes (separated 120°) were investigated, as in Ref. 15. The strake(s) rotate about the axis of the radome, and the size and configurations tested, seen in Fig. 21b, were the best from the wind tunnel test. The strake(s) were fixed at one particular angle and an angle of attack sweep was performed. The vertical nose strake is a small, single strake located on the leeward side, near the tip of the nose. It pivots about an axis perpendicular to the surface of the forebody, with a positive deflection defined as trailing edge left. The dimensions of the vertical nose strake are presented in Fig. 21c.

7.2 METHODOLOGY

The tests were performed following standard "wind tunnel procedures". The gauges were zeroed at the beginning of each run with the model at $\alpha = \beta = 0°$. A static "alpha" tare (or weight

tare) was performed before the actual run. This consists of an angle of attack sweep with the tunnel off ($Q_\infty = 0$) to account for gravity effects. After that, the model is always returned to $\alpha = 0°$, a zero point is taken, and the tunnel is started.

For the static tests, data were acquired at 100 samples/sec for 25 seconds (500 samples/channel), and data were not filtered. The large number of samples acquired permitted to obtain a mean value that closely represents the average gauge reading at the particular loading condition.

The water tunnel data were corrected only at high angles of attack. This correction is required as a result of a significant expansion of the wake when the wing stalls and it was developed by Cunningham (Ref. 5). It is a semi-empirical relationship based only on planform blockage and angle of attack. Equations in Ref. 5 are given only for C_N; however, since this is actually a Q_∞ correction, it was also applied to the other components in a similar manner.

The equation used is the following:

$$C_{N_{corrected}} = C_{N_{uncorrected}} \cdot \left(1 - C_w A_r \sin\alpha'\right)^2,$$

$$\alpha' = 90° \left(\frac{\alpha - \alpha_{ts}}{90° - \alpha_{ts}}\right)$$

$$Cw = 1.57$$

$$Ar = \frac{\text{Model Planform Area}}{\text{Tunnel Test Section Area}}$$

The parameter C_W is empirical and is analogous to the contraction coefficient defined for flows through an orifice plate; α_{ts} is the angle of attack at which the wing completely stalls. The correction is applied starting at $\alpha = 38°$ for the delta wings and at $\alpha = 40°$ for the F/A-18 (approximate stall angles for each configuration). Figure 22 shows uncorrected and corrected data for the 70° delta wing at zero sideslip, with the largest differences occurring in the normal and side forces.

7.3 SOFTWARE

The "Use Balance" button in the main front panel provides access to the software section used during the static water tunnel tests. The different features included in this panel are illustrated in Fig. 23a. The model constants and the tunnel speed can be specified with the "Model Constants" button. By clicking on the "Weight Tare" button, the panel seen in Fig. 23b is opened. In this particular sub-panel, the "Create New Static Tare" button is used to perform the static or weight tare. The axis of motion is selectable, since tares can be performed in any of the three axis. For these particular experiments (angle of attack sweeps), a static tare in pitch is necessary. Data are acquired for different angles of attack and then curve-fitted for the entire angle of attack range. The user can select the order of the polynomial curve fit (up to 5). The static tare will then be subtracted from the raw data at the specific angle of attack. If a tare was already taken and it can be used for the configuration being tested, it can be loaded with the "Load Old Static Tare" button. The other two buttons seen in Fig. 23b deal with rotary tares and they will be described in Volume II (rotary balance tests).

The "Static Data" panel allows to take data and monitor all the signals (Fig. 23c). The first point of every run is always a zero point, i.e., α, β, ϕ and Q_∞ are zero. After a data point is acquired, a graph of any of the channels (raw voltage) versus time can be displayed. Also displayed are the average voltage calculated for each channel and the values of the five coefficients. Data can be later reprocessed with the "Reprocess Data" button. The user has the option of reprocessing a static tare, a rotary tare or a regular run (Reprocess EU panel, Fig. 23d). The raw data file corresponding to the desired run has to be loaded first, and then other parameters are specified, giving the flexibility of re-calculating a data set with different static tares, model constants, calibration matrices, etc. Before loading the raw data, it is important to specify the nature of the run (static or rotary) that will be reprocessed.

Specific inputs for this section of the program include:

- Model Constants: Reference area, span, mean aerodynamic chord.
- Tunnel Conditions: Velocity, angle of attack α, sideslip angle β, roll angle ϕ.

7.4 70° DELTA WING MODEL RESULTS

7.4.1 Effect of Free Stream Velocity

Angle of attack sweeps (from 0° to 42.5°) were conducted at different free stream velocities, from 7.6 cm/sec (0.25 ft/sec) to 20.3 cm/sec (0.67 ft/sec). The Reynolds number (based on $\bar{c}$) for this range of velocities varied from 17,000 to 45,000. The results, shown in Fig. 24, reveal minor differences in the longitudinal characteristics. In general, there is an increase in the maximum normal force coefficient as the speed is increased. The directional characteristics are similar for the different conditions, except for the lowest speed. This particular case presents large fluctuations in side force; however, those changes in side force are not translated into yawing moment changes. The large values of the side force at $\beta = 0°$ is produced probably by interactions of the wing vortices with the balance fairings, which are relatively large and can be acting as a fuselage. The highest velocity case presents an offset in the rolling moment curve, while the other curves show very similar and small Cl values.

The large fluctuations in side force observed at the lowest speed ($V_\infty = 7.6$ cm/sec = 0.25 ft/sec) are due to the fact that, apparently, this particular speed excites the resonant frequency of the sting/balance/model system. Figure 25a shows the raw voltages for the five channels with the model at $\alpha = 20°$ and the tunnel running at 7.6 cm/sec, and the fluctuations in the yawing moment sections (CH 0 and CH 4) are evident. If the velocity is increased or decreased slightly, the fluctuations disappear and very steady signals are obtained for all the channels (Figs. 25b and c). The case at $V_\infty = 7.6$ cm/sec is presented in more detail in Fig. 25d. The frequency of the fluctuations is approximately 1.2 Hz, which is probably the resonant frequency of the system. Even though all the channels show fluctuations, the magnitudes of the oscillations in Channels 1, 2 and 3 are in the order of 20-40 milli-Volts, while the yawing moment channels (CH 0 and CH 4) reveal magnitude changes of as much as 1 Volt (note different vertical scales). Undoubtedly, this will affect the accuracy of the average value calculated for these two channels and therefore, the value of the side force.

7.4.2 Additional Investigations and Comparison with Wind Tunnel Data

The longitudinal characteristics of the 70° delta wing are presented and compared to wind tunnel data in Fig. 26. The water tunnel data (obtained at $V_\infty = 17.8$ cm/sec = 0.58 ft/sec) are

compared to similar data obtained in another water tunnel (Ref. 5), and in the KU 3x4' wind tunnel (Ref. 8), the WSU 7x10' wind tunnel (Ref. 9) and the Langley 12-ft wind tunnel (Ref. 10). The normal force coefficient agrees very well with most of the data, except for the Langley data. The differences between the 12-ft tunnel data and the other wind tunnel data are quite significant and are probably due to the type of corrections applied, mounting system, flow quality, etc. The pitching moments referenced to three different locations (30%, 40% and 50% $\bar{c}$) are seen in Fig. 26b. The software provided the moments referenced to the 50% $\bar{c}$ and then the appropriate transformations were applied to obtain the pitching moments at the other two locations. The pitching moments at 30% $\bar{c}$ and 40% $\bar{c}$ are compared to wind tunnel data in Figs. 26c and d and the agreement is satisfactory.

Unexpected large side force variations were observed at zero sideslip. Figure 27 shows C_Y at $\beta = 0°$ and large side force changes can be seen for angles of attack greater than 10°. These changes are probably caused by a small angle of sideslip, perhaps due to an imperfect alignment of the model with the free stream at the $\beta = 0°$ reference, and the large fairings used to cover the balance. The top and bottom fairings are acting as a body and therefore, pure delta wing results at non-zero sideslip cannot be expected. The water tunnel results were compared to wind tunnel data from Ref. 9, where a large bottom fairing was also used, and similar side force variations are observed. C_Y and C_n changes were also encountered during sideslip sweeps at constant angles of attack, and, again, data compare very well to data from Ref. 8 at $\alpha = 10°$ (Fig. 28). Changes in rolling moment with sideslip variations are as expected. The asymmetric vortices over the delta wing produce negative rolling moments with positive β and vice versa. Excellent agreement is observed in Fig. 29 between these data and wind tunnel data from Ref. 11 at 10° and 20° angles of attack.

The effect of sideslip was also investigated by performing angle of attack sweeps at constant β. Data for the case at $\beta = 10°$ are shown in Fig. 30, and the expected decrease in C_N is evident in the first plot. This particular sideslip angle produces a stabilizing (positive) increment in side force (for angles of attack greater than 15°), and the negative increment in the rolling moment coefficient for positive β's observed in Fig. 29 is almost constant for angles of attack greater than 10°.

7.5 76° DELTA WING MODEL RESULTS

Tests were performed on a 76° delta wing, and results for C_N and C_m are presented in Fig. 31. The water tunnel data for C_N match both wind tunnel data (from Refs. 8 and 12) up to $\alpha = 35°$. Beyond that angle of attack, large differences are observed with one of the data sets (Ref. 12), but the agreement with the other wind tunnel data set, despite being a 75° delta, is very good. The slope and trends of the pitching moment curve obtained for the 76° delta wing in the water tunnel is very similar to that corresponding to the 75° delta in the wind tunnel.

The changes in the rolling moment coefficient produced by sideslip variations at constant angles of attack are shown in Fig. 32. Trends are as expected, and, in general, the comparison to wind tunnel data (Ref. 12) is again quite acceptable.

7.6 80° DELTA WING MODEL RESULTS

Results of the tests conducted on the 80° delta wing reveal similarities with those obtained on the 76° delta wing. As seen in Fig. 33, the C_N data agree very well with results from Refs. 8

and 13, while the results reported in Ref. 12 again present higher values. The agreement between the pitching moment (at 25% $\bar{c}$) measured in the water tunnel and the wind tunnel data from Ref. 13 is remarkable.

Sideslip variations produce changes in C_l with characteristics akin to those found in Ref. 12, as Fig. 34 indicates. The tests performed in the water tunnel with this model also reveal large changes in side force and yawing moment coefficients with β sweeps, as shown in Fig. 35. These large changes in the directional characteristics are probably due again to the fairings which, in this model, appear to have a larger influence because of the reduced span of this wing. Flow visualization performed on this wing indicates the mechanism producing these changes. When a negative sideslip is introduced, the windward (left) vortex is much closer to the surface than the leeward vortex, resulting in a loss of vortex lift on the leeward (right) side with the associated positive rolling moment. However, as the angle of attack is increased, the burst point of the windward vortex moves forward. The flow visualization photo in Fig. 36 at $\alpha = 30°$ and $\beta = -10°$ reveals that the burst point of the left vortex is on the wing and therefore, the net rolling moment change starts decreasing. The effect of the burst point location is also noticed in the C_Y and C_n changes. The proximity of the windward vortex to the fairing is producing a suction on that side and thus, a negative side force (for the negative β case). When the burst point moves forward of the fairing (at about 37° angle of attack), the negative side force and yawing moment decrease significantly, as shown for the $\alpha = 40°$ case in Fig. 35. A similar mechanism occurs for positive sideslip angles.

7.7 1/32nd-SCALE F/A-18 MODEL RESULTS

An extensive investigation was conducted using the F/A-18 model, including baseline characteristics, effect of control surface deflections, and effect of various FVC methods. The majority of these tests were performed at $V_\infty = 12.7$ cm/sec = 0.42 ft/sec, corresponding to Re (based on $\bar{c}$) of 12,500.

7.7.1 Baseline F/A-18

Figure 37 shows a comparison between the water tunnel test and other wind tunnel tests for the baseline F/A-18 at $\beta = 0°$. The agreement in C_N is very good, both in slope and absolute magnitude. The data obtained in the water tunnel match not only other small-scale wind tunnel tests (Refs. 16 and 18), but the full-scale test at the NASA Ames 80x120' (Ref. 17) and the F/A-18 Aero Model used in simulation as well. Only one data set (Langley 12', Ref. 19) has much lower values than those obtained in this test. The pitching moment measurements also agree well with other data; small differences are seen between 45° and 55° angle of attack, but trends and slopes are very similar. Some differences are observed in side force, with the water and wind tunnel (Ref. 16) models showing opposite asymmetries. For reference, the differences between the two tests results are equivalent to +/-1.5° in sideslip at $\alpha = 30°$. Yawing moment agrees very well up to $\alpha = 50°$; at higher angles of attack, the water tunnel data show a much larger asymmetry. This is confirmed by the flow visualization presented in Fig. 38. The forebody vortex flow field is symmetric up to $\alpha = 50°$. At $\alpha = 55°$, however, the flow presents a strong left-vortex-high asymmetry that will produce a large positive or "nose-right" yawing moment. Sideslip variations (positive and negative β) at $\alpha = 55°$ showed a significant hysteresis effect on the forebody asymmetry orientation and resulting yawing moments. The direction of the asymmetry at $\beta = 0°$ depends on the direction of the sideslip variation, thus providing a "bi-stable" behavior of the

forebody vortices. This behavior was also observed in Ref. 20. At $\alpha = 60°$ the flow is still asymmetric but the right forebody vortex has moved away from the body surface, therefore decreasing the asymmetry and the magnitude of the yawing moment.

The disagreement in side force is not surprising considering that the forebody aerodynamics of this configuration is very sensitive to Reynolds number and to imperfections or perturbances (such as blowing ports) in the nose region. During the wind tunnel test at the NASA Ames 7x10' (Ref. 16), different values of side force were obtained (with the same model and the same Reynolds number) depending on the nose tested. Figure 39 shows the differences in C_Y for three noses: the clean nose (no FVC devices), one with small external nozzles and one with slots for blowing. Lateral/directional characteristics were also compared to data from Refs. 17 and 18, as seen in Figs. 40 and 41, for $\alpha = 30°$ and 40°, respectively. Similarities in the C_Y, C_n and C_l curves are evident, especially for sideslip angles between 10° and -10°. It should be noted that corrections due to wall proximity during sideslip sweeps were not introduced in the data reduction scheme, and therefore, small discrepancies at high β's can be expected. These comparisons show that the balance can be used effectively to measure five components of the forces and moments experienced by a "real" configuration (as opposed to "generic", as in the case of the delta wings) at this flow regime.

Results of angle of attack sweeps at different sideslip angles are presented in Figs. 42 and 43. The effect of sideslip angle in the normal force coefficient is minimum (Fig. 42), and trends in the lateral-directional characteristics are as expected (Fig. 43). One condition ($\beta = -10°$) is compared to the results of the NASA Ames 7x10' (Ref. 16) test, and small discrepancies in the magnitudes of C_Y and C_n are observed. The value of the side force measured in the water tunnel is lower than in the wind tunnel test at low angles of attack and higher at high angles of attack. This produces a lower yawing moment at low α's, and higher values of C_n at high angles of attack. It appears that the vertical tails are less effective in the water tunnel, probably because the flow is separating at lower sideslip angles than in the wind tunnel. At $\beta = -10°$, the vertical tail in the water tunnel likely generates less negative yawing moment. At higher angles of attack ($\alpha > 40°$), data indicate that the asymmetry of the forebody vortices is larger in the water tunnel than in the wind tunnel resulting in a larger positive yawing moment and a larger positive side force. The changes in the forces and moments produced by sideslip variations at constant angles of attack, from $\alpha = 0°$ to 60°, can be seen in Fig. 44. The strong asymmetry in the flow at $\alpha = 60°$ is indicated again by the non-zero values of the side force and yawing moment curves at $\beta = 0°$.

In order to complete the data analysis of the baseline F/A-18, the lateral-directional derivatives $CY\beta$, $Cn\beta$ and $Cl\beta$ were calculated (based on $\beta = \pm 10°$) using the water tunnel data, and the results were compared to the derivatives obtained using the Ames 7x10' data from Ref. 16 (Fig. 45). Even though there are some discrepancies in the magnitudes of the derivatives from the two different tests, the similarities in the trends are quite remarkable.

7.7.2 Conventional Control Surfaces

The effect of deflecting the rudders +/-30° was investigated, and the yawing moment and yawing moment increments (ΔC_n) produced by the deflections are presented in Fig. 46. The effect of the rudder is as expected; however, the magnitude of the yawing moment increments measured in the water tunnel are smaller than those observed in the NASA Ames 7x10' wind tunnel test (Ref. 16). This is very consistent with the effect of sideslip discussed in the previous section, where at low angles of attack, the changes in yawing moment were smaller than the ones measured

in the wind tunnel tests. Again, it appears that the rudder deflections in the water tunnel are not as effective as in the wind tunnel, probably because the flow is separating earlier at the lower Re. For unknown reasons, a slightly better agreement is observed between the water tunnel data and the NASA Ames 80x120' wind tunnel data (Ref. 17)

The rolling moment and the rolling moment increment (ΔC_l) produced by a $\pm 10°$ aileron deflection are shown in Fig. 47. The magnitude of the changes again are slightly smaller in the water tunnel, but the agreement is acceptable.

7.7.3 Jet Blowing

Jet blowing with the blowing nozzles located at 150° from the windward meridian and canted inboard 60° was the configuration that provided the best-behaved and most effective results in the wind tunnel test (Ref. 14). The same configuration was tested in the water tunnel, and the results are presented in Fig. 48. Jet blowing does not affect the longitudinal characteristics, C_N and C_m, as seen in the first two plots of Fig. 48. The largest effect, as expected, occurs in the directional characteristics. Blowing on the right side produces positive changes in side force and yawing moment, and trends are very well behaved with angle of attack and blowing rate up to $\alpha = 50°$. For angles of attack higher than 50°, jet blowing on the right side cannot enhance the already existing asymmetry in the forebody vortex flow field, and therefore, the effectiveness of blowing decreases.

Blowing on the left side is not as well behaved. It is relatively ineffective up to $\alpha = 40°$, then produces left yawing moments at low blowing rates and right yawing moments at $C\mu = 0.0015$, suggesting a condition of overblowing that promotes separated flow instead of attached. Blowing on the left side produces a negative change in yawing moment and completely switches the baseline asymmetry at $\alpha = 55°$ and 60°. As these results indicate, the vortex flow field at 55° angle of attack, where the natural vortex asymmetry is maximum, is very difficult to control. Changes in rolling moment are erratic and small, except at $\alpha = 35°$. Apparently, at this particular angle of attack, there are some interactions between the forebody and the LEX vortices that are producing a small change in rolling moment.

The comparison to wind tunnel test data (Ref. 14) is quite good (Fig. 48), at least in terms of trends. In general, it appears that jet blowing in the water tunnel is less efficient at angles of attack below 40°. On the other hand, for angles of attack between 40° and 60°, the water tunnel tests provide larger increments (the wind tunnel data shown correspond to the most effective runs). It is also evident that jet blowing in the water tunnel produces similar levels of yawing moment change with a much smaller $C\mu$. The reason for this could be related to differences in the flow physics: laminar vs. transitional flow, incompressible vs. compressible flow, unchoked vs. choked flow at the nozzle exit, mixing mechanism of the blowing jet and the vortices, etc.

The force/moment measurements correlate well with flow visualization. Figure 49 shows results of flow visualization at $\alpha = 50°$. The symmetric forebody vortex pattern at this angle of attack can be modified by left or right blowing with the expected results, i.e., delaying separation on the blowing side, except when blowing on the left side with a $C\mu = 0.0015$. At this condition, the blowing jet is clearly seen far away from the body surface, indicating the "overblowing" that causes an early separation on the left side with the associated positive yawing moment.

Blowing was also evaluated under sideslip conditions. Data in Fig. 50 for $\beta = -10°$ and 10° indicate that blowing is still effective within this range of sideslip angles. By applying blowing on

the windward side, the baseline (no blowing) asymmetry can be either reduced or eliminated completely. By blowing on the leeward side, the yawing moment can be increased, if desired, for additional yaw control.

7.7.4 Single Rotatable Tip-Strake

Reference 15 showed that by rotating a very small strake near the tip of the F/A-18 and along a gradient centered at $\Phi = 180°$ (the strake on top of the nose), large changes in side force and yawing moments are created. Figure 51 presents results obtained in the water tunnel for a similar configuration. The rotatable strake does not affect the normal force. When the strake is at $\Phi = 180°$, the forces and moments show that the flow field is similar to the baseline F/A-18 (no strake). By rotating the strake +/-30° about $\Phi = 180°$, positive and negative yawing moments can be obtained. In general, rotating the strake 30° from the leeward meridian towards the right side ($\Phi = 150°$) of the forebody produces a right-vortex-high pattern, with the corresponding negative or "nose-left" yawing moment. As discussed in Ref. 15, the mechanism that makes the strake so efficient when acting on this area of the forebody is not very clear. The strake is either acting as a "spoiler" and, therefore, when is rotated to the right produces an early separation on that side with the associated nose-left yawing moment, or is changing the secondary vortex structure and reattachment. Flow visualization shows the effect of the strake, but it does not show (because of the small scale) the mechanism that produces such effect. Rotating the strake to the left side of the forebody has the opposite effect and a positive yawing moment is obtained. As observed with the pneumatic FVC technique, the single strake is more effective in the wind tunnel at low angles of attack (between 30° and 45°), and more effective in the water tunnel at high angles of attack. There is a difference also (probably due to changes in the separation location) in the strake angle at which the maximum increments are obtained in the two tests: +/-30° in the water tunnel and +/-20° in the wind tunnel. Changes in rolling moment are small and proverse, i.e., a positive rotation of the strake generates both positive C_n and C_l and vice versa.

7.7.5 Dual Rotatable Tip-Strakes

By using dual strakes (a fixed pair of strakes that rotate together), it is possible to modulate the increments and obtain better-behaved directional changes. Results from Ref. 15 indicate that dual strakes with a separation angle $\Delta\Phi = 120°$ appear to be the optimum combination of all the configuration tested. The water tunnel test results on these particular strakes are shown in Fig. 52. A strake angle $\Phi = 0°$ is now defined as the angle at which the strakes are located symmetrically at +/-60° from the windward ray. At $\Phi = 0°$, the yawing moment indicates that the flow is similar to the baseline (no strakes) case, with the exception of $\alpha = 50°$, where an asymmetry is observed (baseline flow is symmetric at $\alpha = 50°$). Large changes in side force and yawing moment are induced by rotating the strakes +/-40°. A positive strake rotation (towards the right side of the fuselage) induces a negative yawing moment, and the opposite occurs when the strakes are rotated to the left. Trends are well-behaved and again the water tunnel test shows smaller increments than the wind tunnel test at low angles of attack and larger increments at angles of attack higher than 45°.

7.7.6 Vertical Nose Strake

The vertical nose strake (VNS) is a small strake mounted on the leeward side of the forebody near the tip, and it pivots about an axis perpendicular to the surface of the forebody. The presence of the VNS at $\delta = 0°$ modifies the baseline flow characteristics for angles of attack

between 50° and 60°. A right-vortex-high asymmetry, with the associate negative yawing moment, is observed in this angle of attack range. A positive VNS deflection produces a positive yawing moment and vice versa (Fig. 53). Flow visualization shows that, when the VNS is pivoted trailing edge left, a strong vortex forms at its leading edge. This leading edge vortex moves toward the left side of the forebody, and apparently, is increasing the suction on the right side and, at the same time, is pushing the left forebody vortex away from the body surface.

8.0 CONCLUSIONS

A five-component balance was designed, built and tested in the Eidetics Flow Visualization Water Tunnel. The objectives of this phase of the research program were accomplished and it was demonstrated that force and moment measurements in a water tunnel are possible and practical with today's technology. The water tunnel balance showed nearly linear response in the primary gauges and very low component interactions and hysteresis.

Results from static water tunnel experiments performed on delta wings (70°, 76° and 80° sweep angles) were compared to wind tunnel data obtained on similar configurations. In most cases, the comparisons were very satisfactory, indicating that a multi-component water tunnel balance is a valid and useful tool, especially when used in conjunction with flow visualization.

A full matrix of angles of attack and sideslip were tested for the baseline F/A-18 and data showed very good agreement with wind tunnel tests. The major differences are seen in side force and yawing moment, but that could be due to the sensitivity of this configuration to Reynolds number and to forebody geometry changes. A smaller effect of the vertical tails in the water tunnel was also evidenced by these data. The effect of conventional and non-conventional (FVC) control techniques were also investigated. Results from the water tunnel force/moment measurements showed the exact same trends as the wind tunnel tests, with minor discrepancies in the magnitudes of the changes produced by each of the techniques. The magnitudes of the effects generated by vortical behavior were invariably larger in the water tunnel than in the wind tunnel.

In general, the data obtained in this investigation show conclusively that water tunnels can be used very effectively for quantitative as well as qualitative measurements and emphasizes the importance of having the capability of performing simultaneous force/moment measurements and flow visualization.

9.0 ACKNOWLEDGMENTS

This study was supported by the NASA Dryden Flight Research Center under SBIR Phase II Contract No. NAS2-13571. The technical monitor was Mr. John Del Frate. We would also like to acknowledge Mr. Mel Heier and Mr. Patrick Mc Farland from PSI-TRONIX for the technical support and assistance during and after the balance gauging.

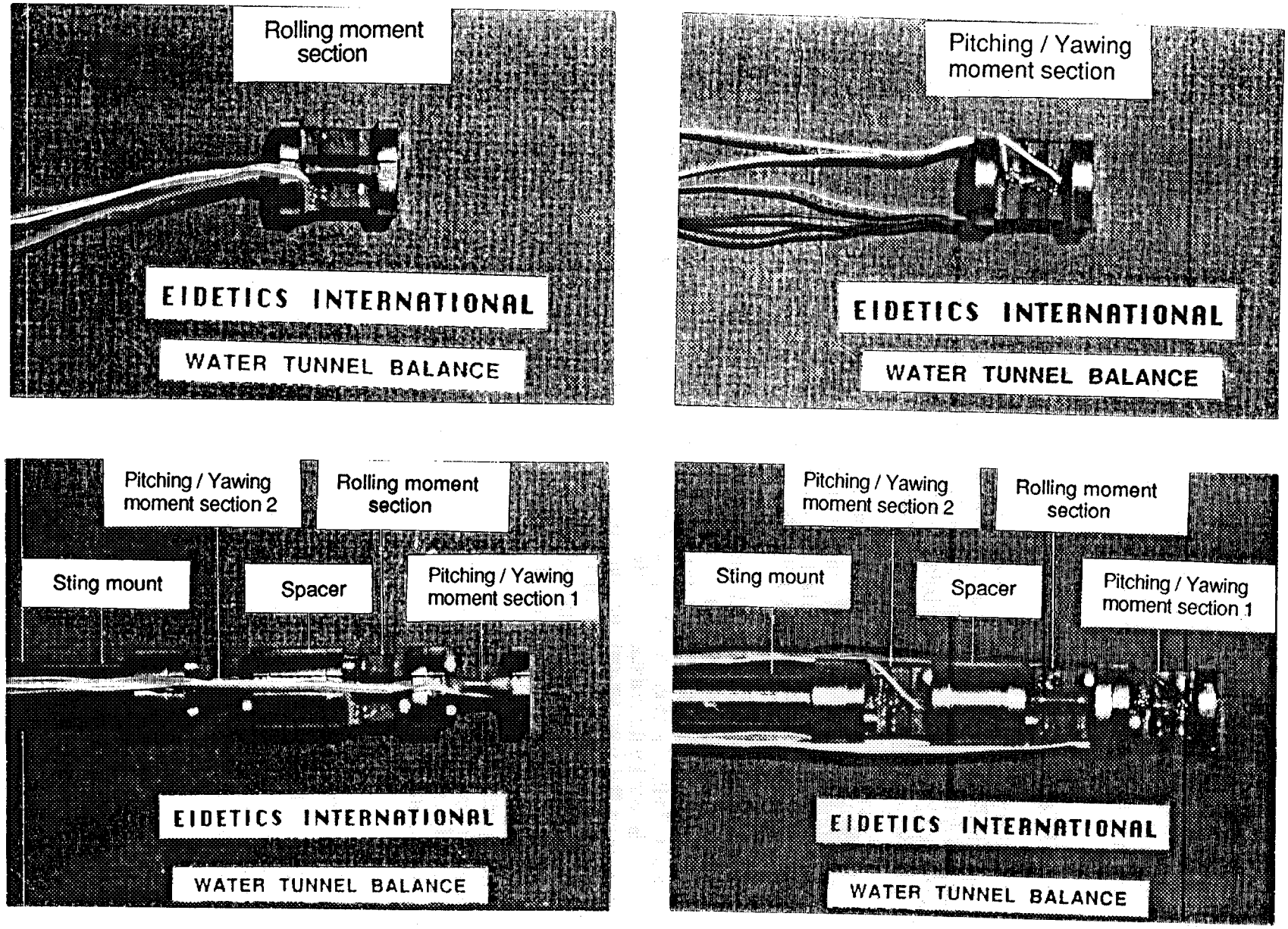

Figure 1 - Photographs of the 3-Component Balance (Phase I)

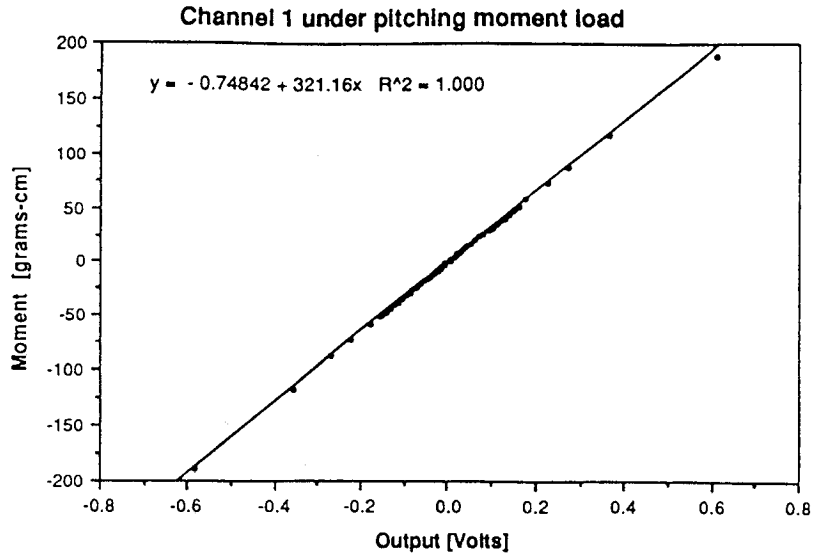

a) Channel 1 (Foreward Pitching Moment Gauge)

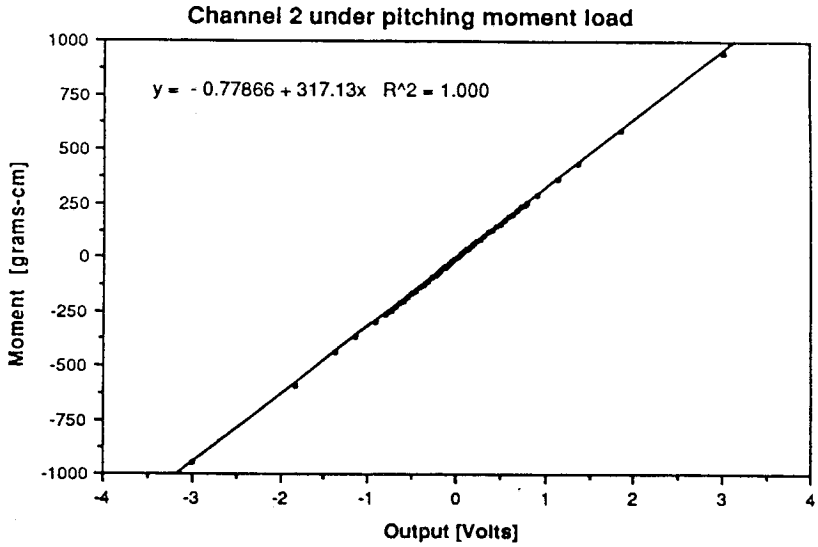

b) Channel 2 (Rearward Pitching Moment Gauge)

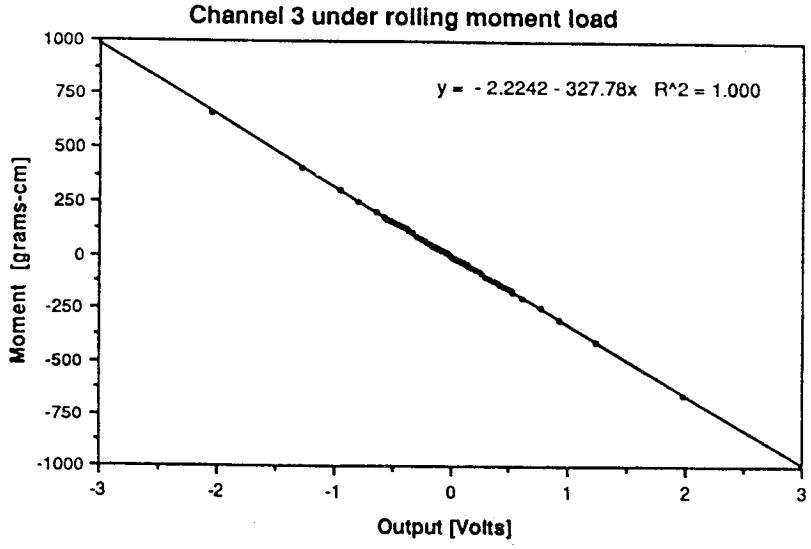

c) Channel 3 (Rolling Moment Gauge)

Figure 2 - Primary Load Calibration Results (Phase I)

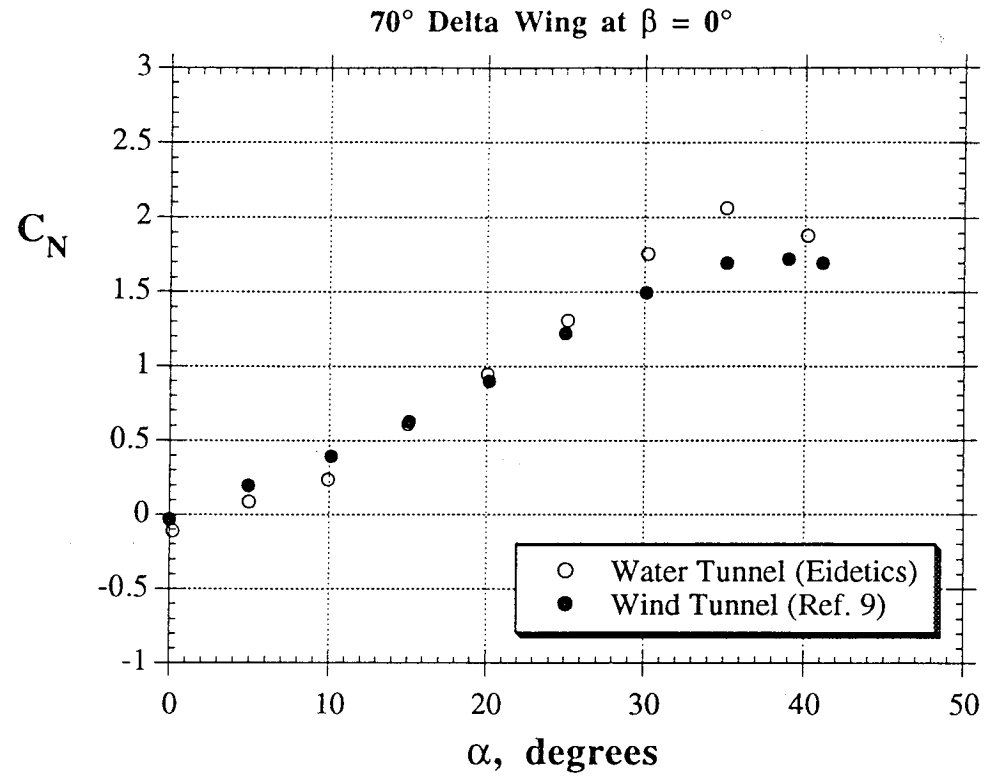

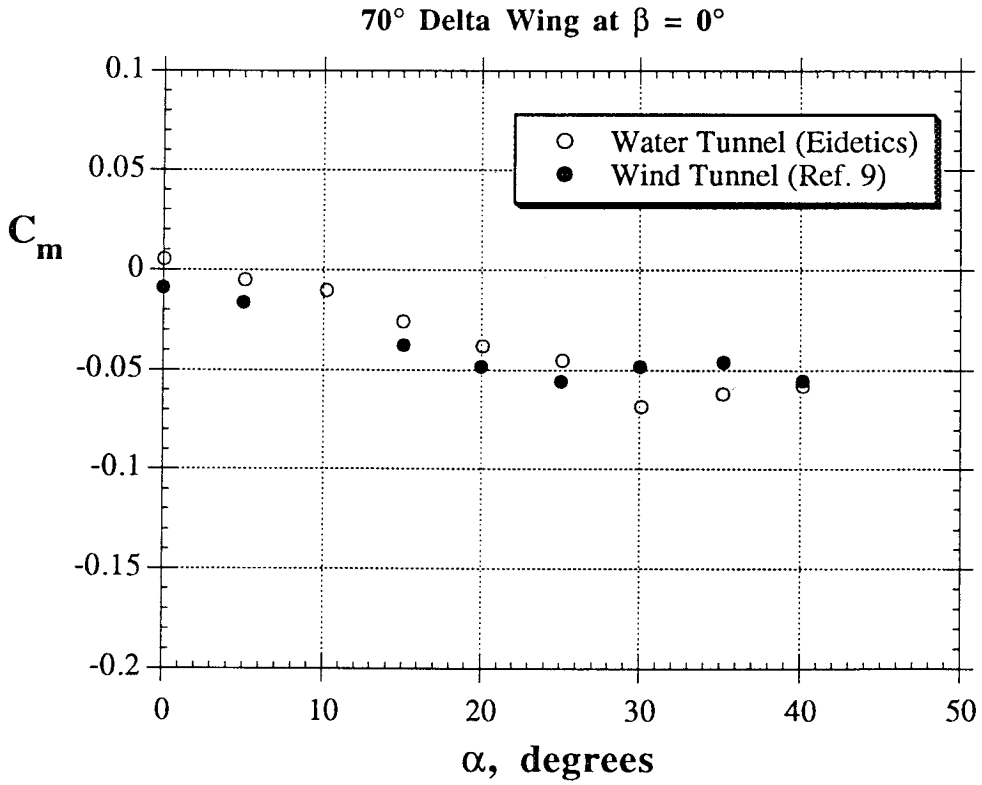

Figure 3 - Results of Force/Moment Measurements (Phase I)
(70° Delta Wing at β = 0°)

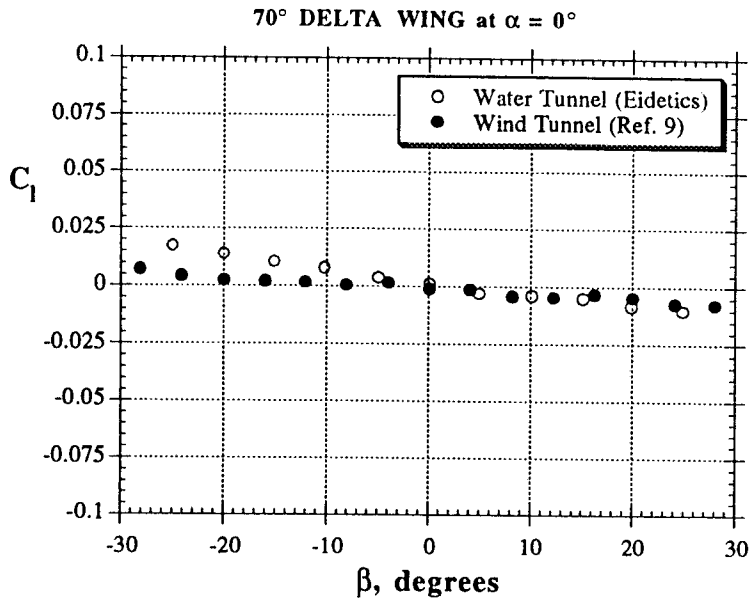

a) $\alpha = 0°$

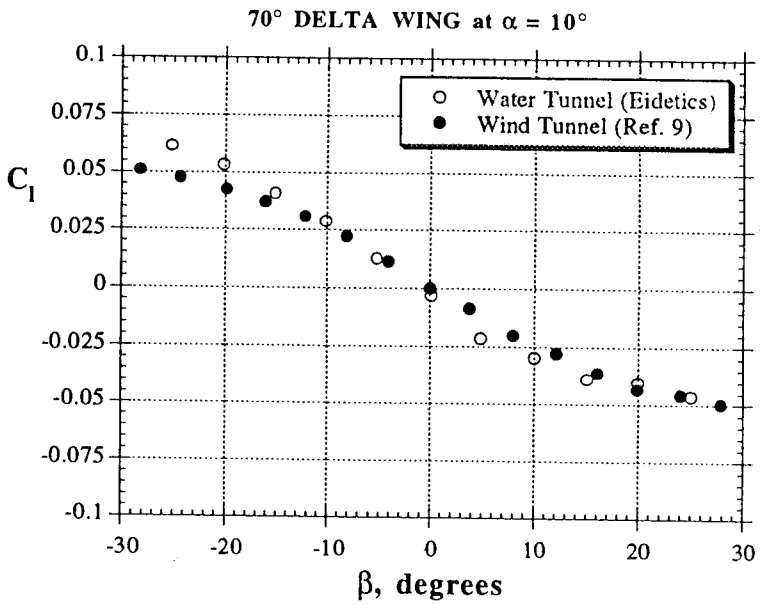

b) $\alpha = 10°$

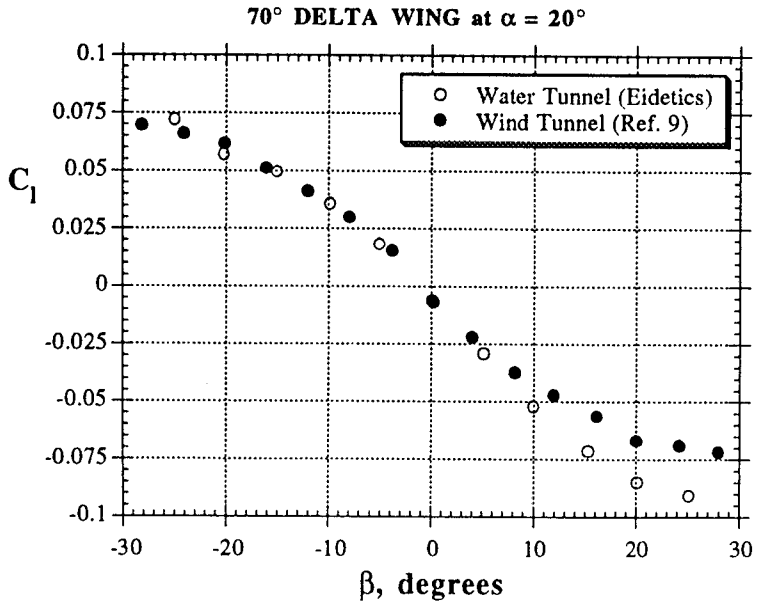

c) $\alpha = 20°$

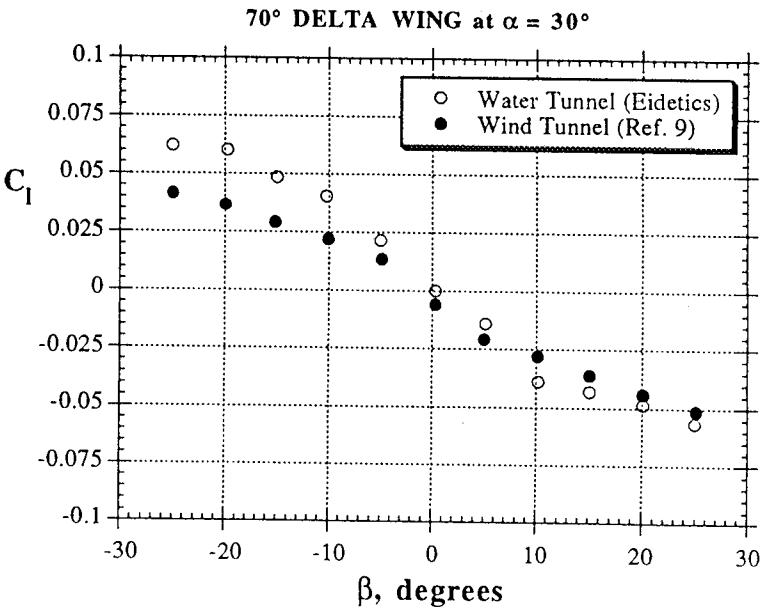

d) $\alpha = 30°$

Figure 4 - Results of Force/Moment Measurements (Phase I)
(70° Delta Wing, β Sweeps at Different Angles of Attack)

FRONT VIEW

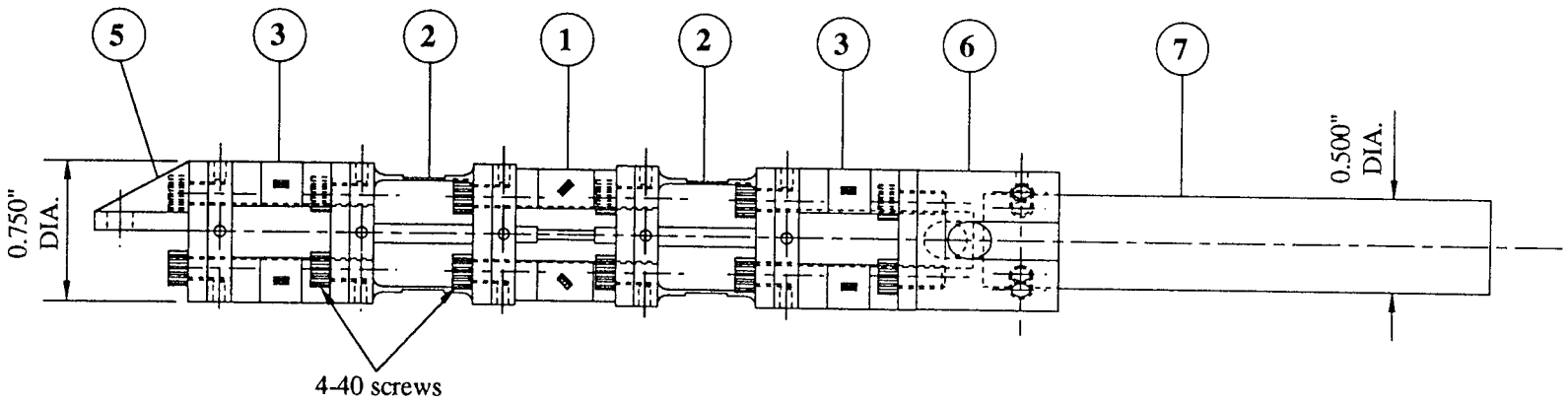

TOP VIEW

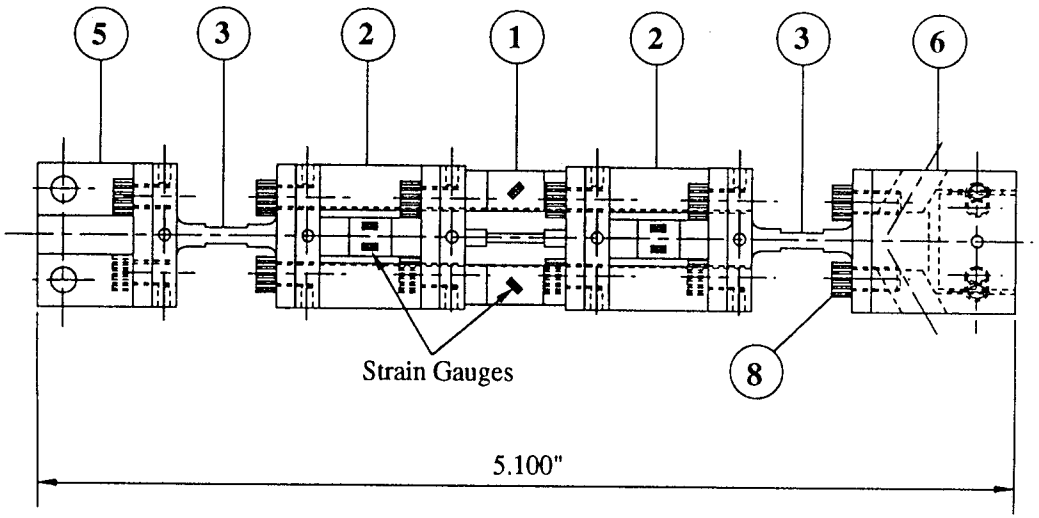

Figure 5 - Schematics of the 5-Component Water Tunnel Balance

Item	Qty.	Description	Drawing #
8	-	Additional Hardware	008
7	1	Sting	007
6	1	Sting Adapter	006
5	1	Model Adapter	005
4	2	Spacer	004
3	2	Yawing Moment Section	003
2	2	Pitching Moment Section	002
1	1	Rolling Moment Section	001

EIDETICS INTERNATIONAL

WATER TUNNEL BALANCE

Material : Stainless Steel 17-4			
Tolerances (unless noted) : x.xxx +/- 0.005			
Designed : CJS	Drawn : CJS	Date : 1/20/93	
Scale : 1:1	All dimensions in inches (unless noted)	Drawing # 102	Rev. -

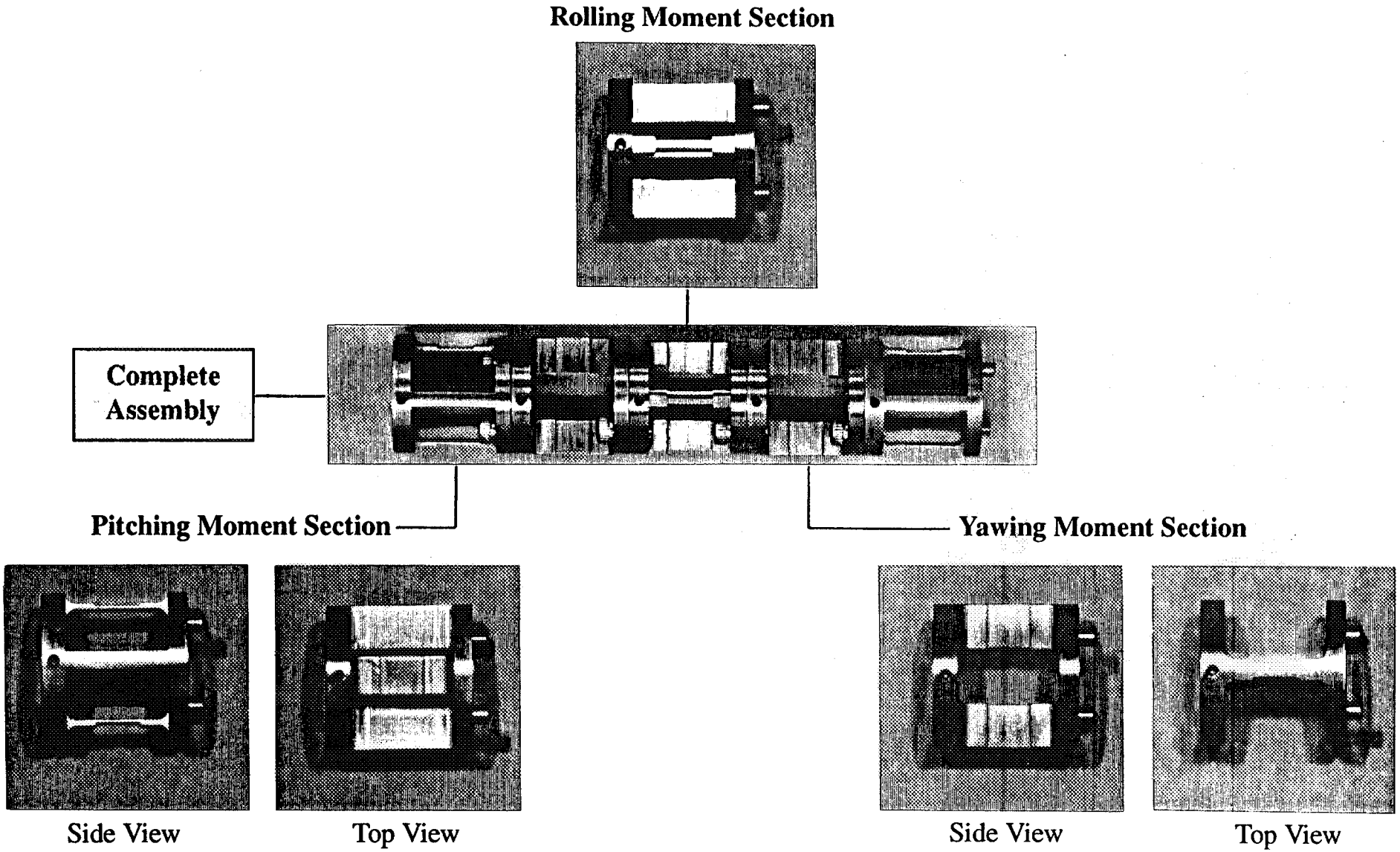

Figure 6 - Photographs of the 5-Component Water Tunnel Balance
(Detail of Mechanical Components)

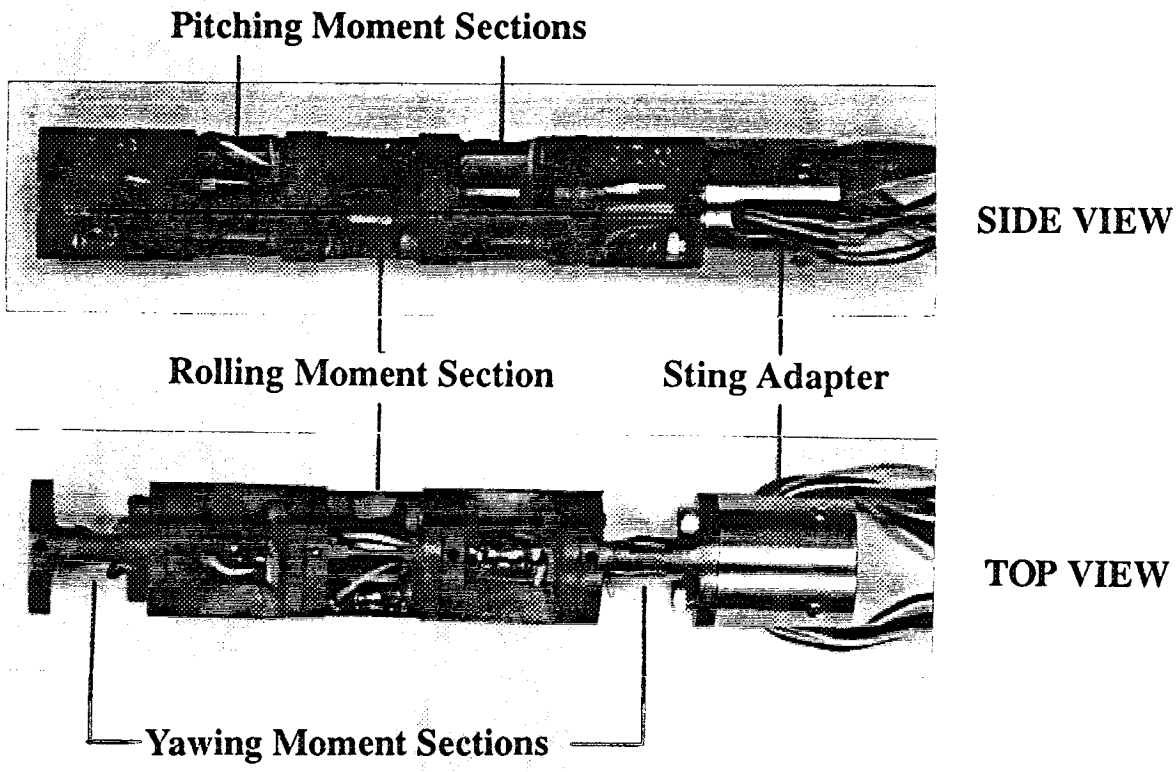

Figure 7 - Photographs of the 5-Component Water Tunnel Balance (Complete Assembly)

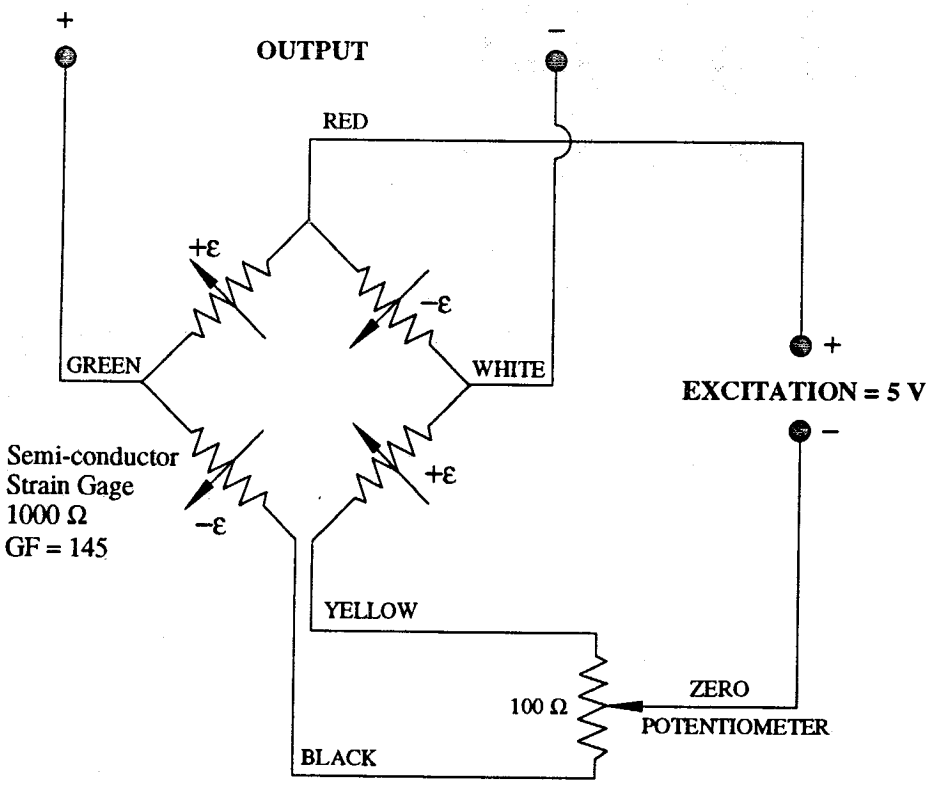

Figure 8 - Wheatstone Bridge Circuit

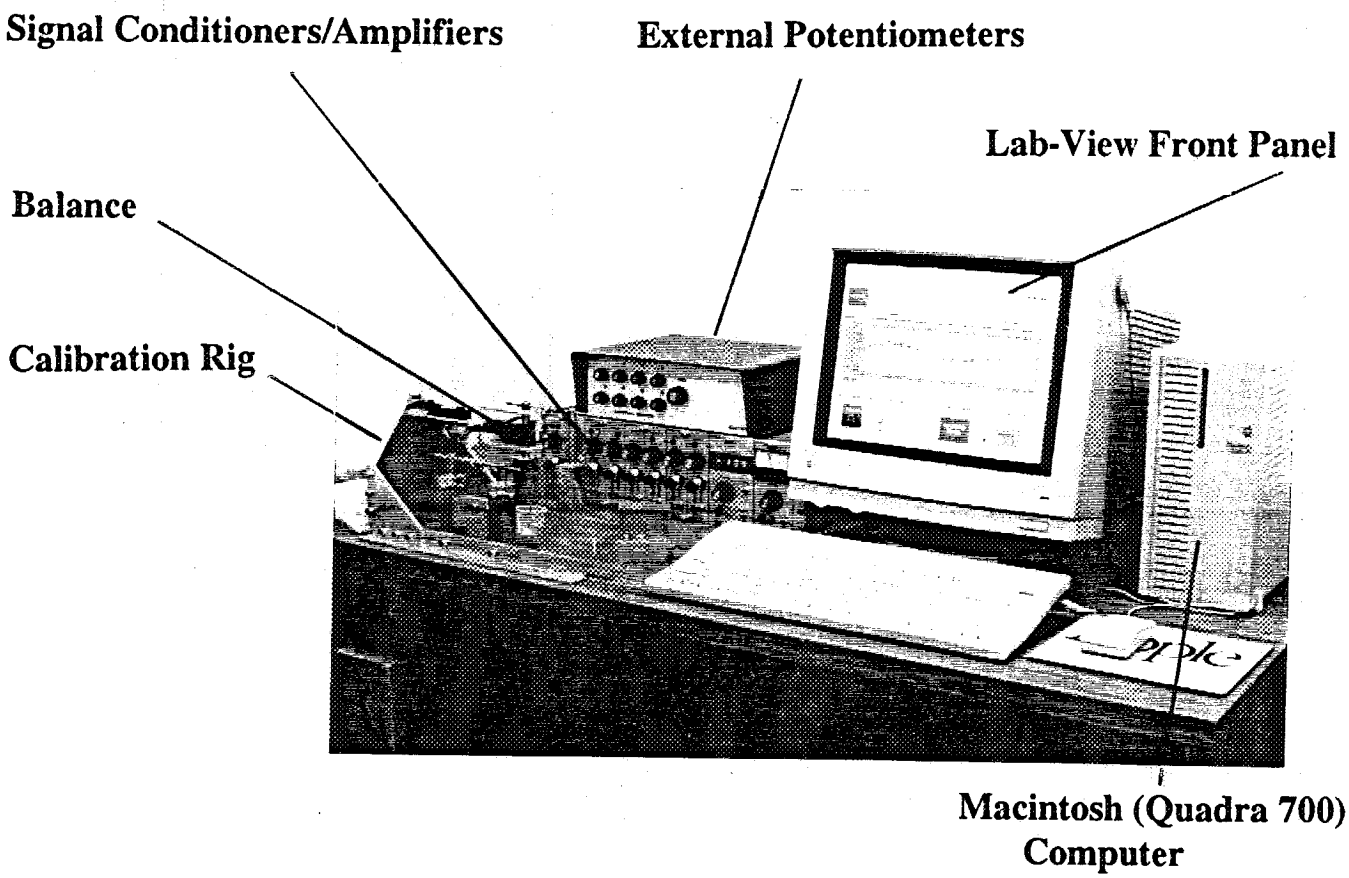

Figure 9 - Data Acquisition/Reduction System, Including Signal Conditioners and Calibration Rig

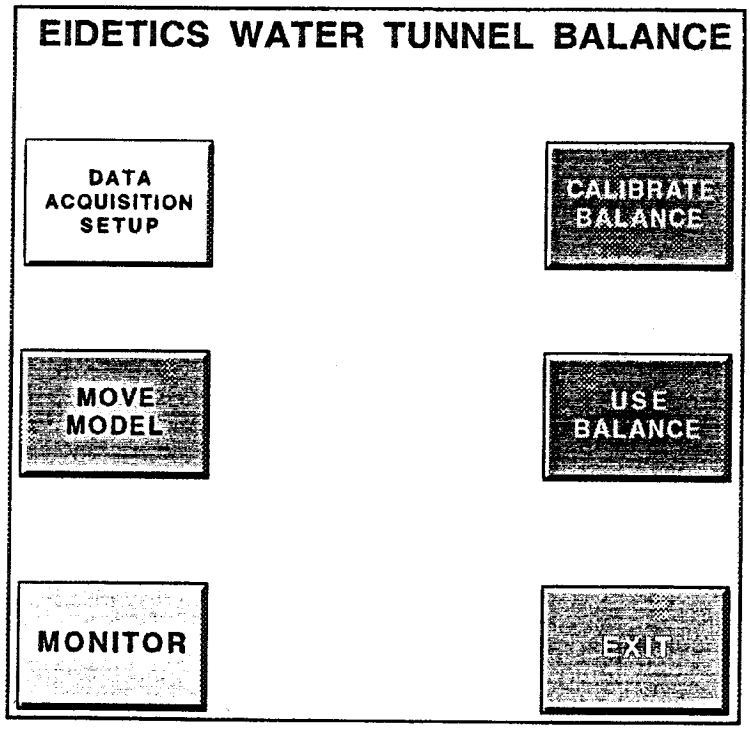

Figure 10 - Main Front Panel of the Data Acquisition/Reduction Software

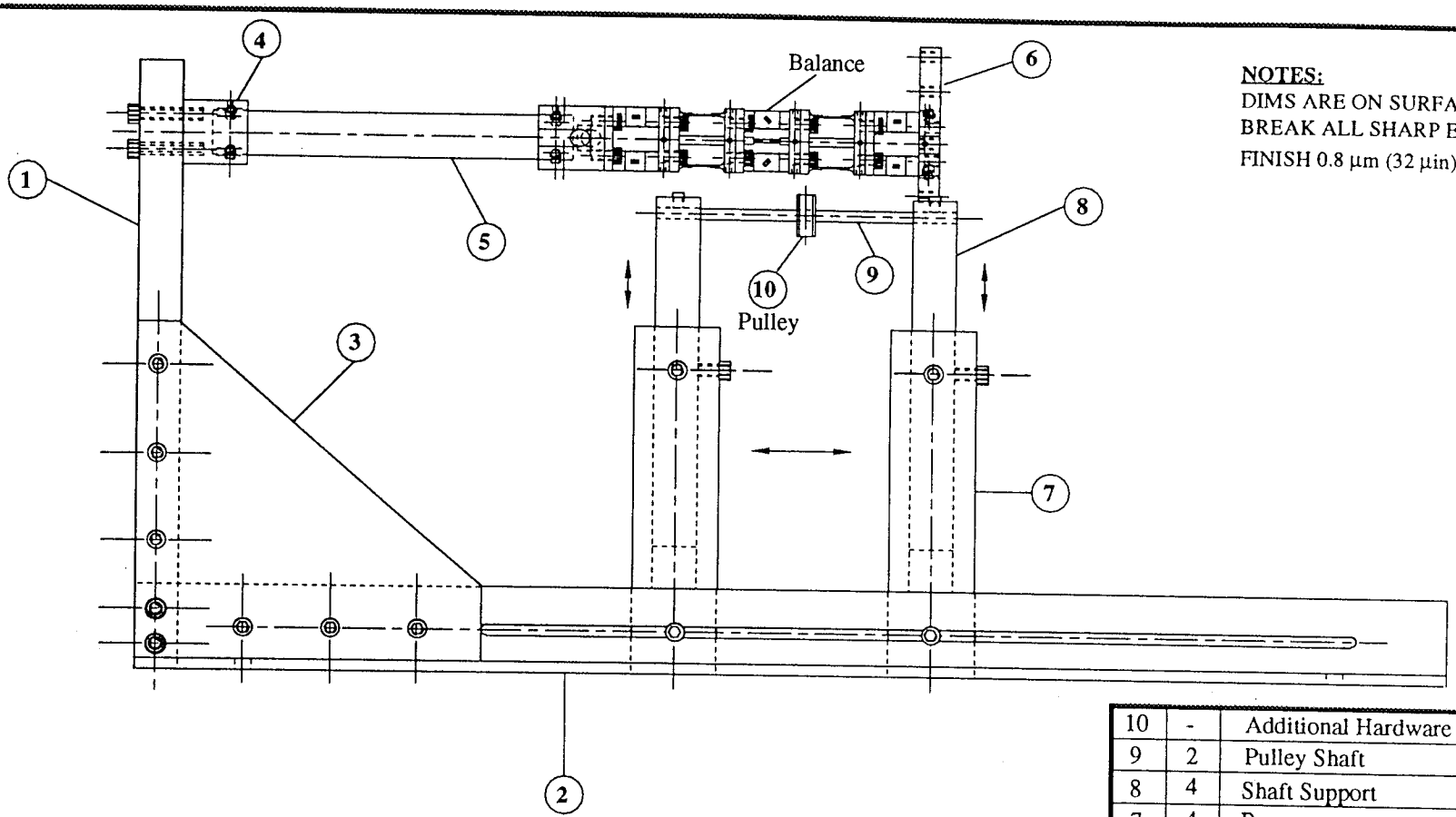

NOTES:
DIMS ARE ON SURFACE OF PART
BREAK ALL SHARP EDGES
FINISH 0.8 µm (32 µin) IN RMS

CALIBRATION RIG

SIDE VIEW

Item	Qty.	Description	Drawing #
10	-	Additional Hardware (Cal.)	020
9	2	Pulley Shaft	019
8	4	Shaft Support	018
7	4	Base	017
6	1	Loading Fixture	016
5	1	Calibration Sting	015
4	1	Sting Support	014
3	2	Side Plate	013
2	2	Rail	012
1	1	Main Support	011

EIDETICS INTERNATIONAL

CALIBRATION RIG
FOR WATER TUNNEL BALANCE

Material :

Tolerances (unless noted) :

Designed : CJS	Drawn : CJS	Date : 1/15/93
Scale : 1:2	All dimensions in inches (unless noted)	Drawing # 111 Rev. -

Figure 11 - Schematics of the Calibration Rig

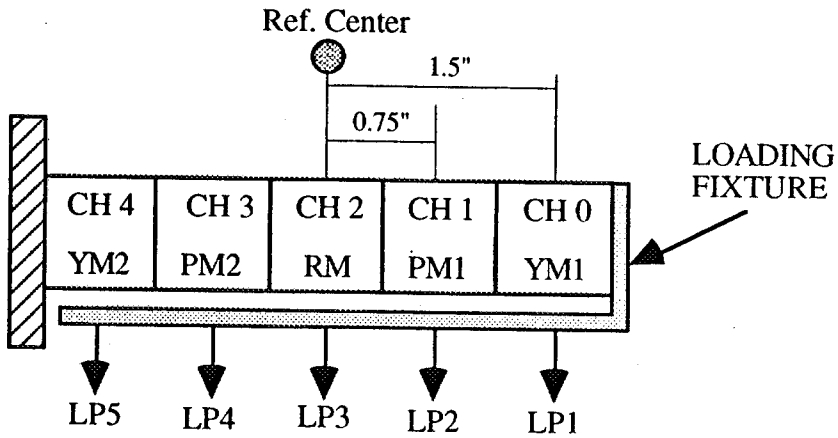

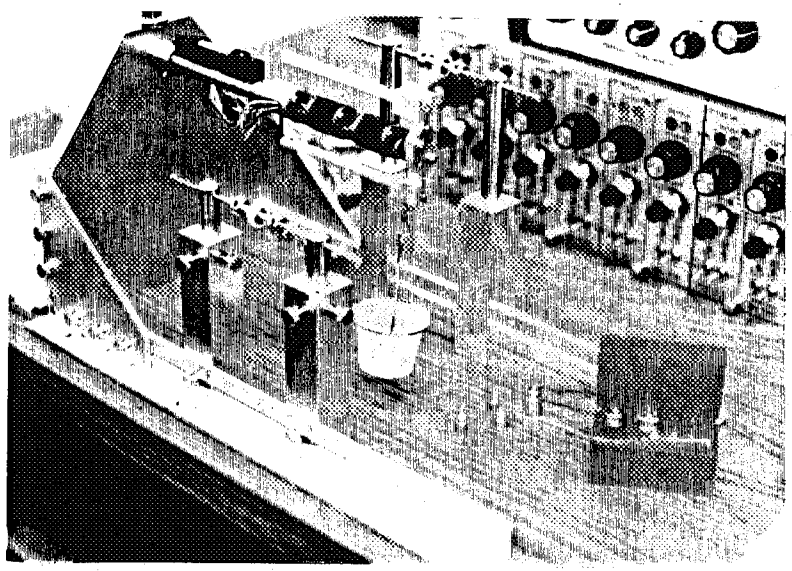

NORMAL FORCE CALIBRATION

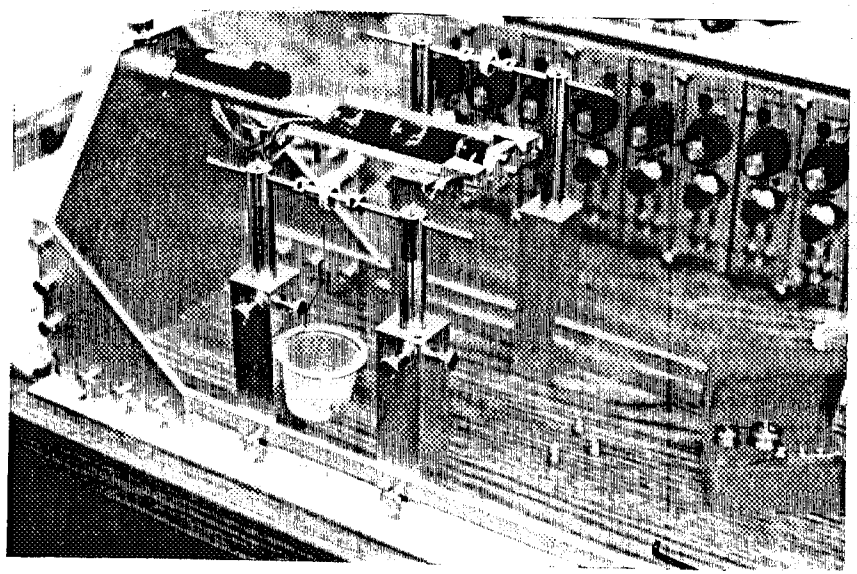

SIDE FORCE CALIBRATION

Figure 12 - Photographs of the Calibration Rig

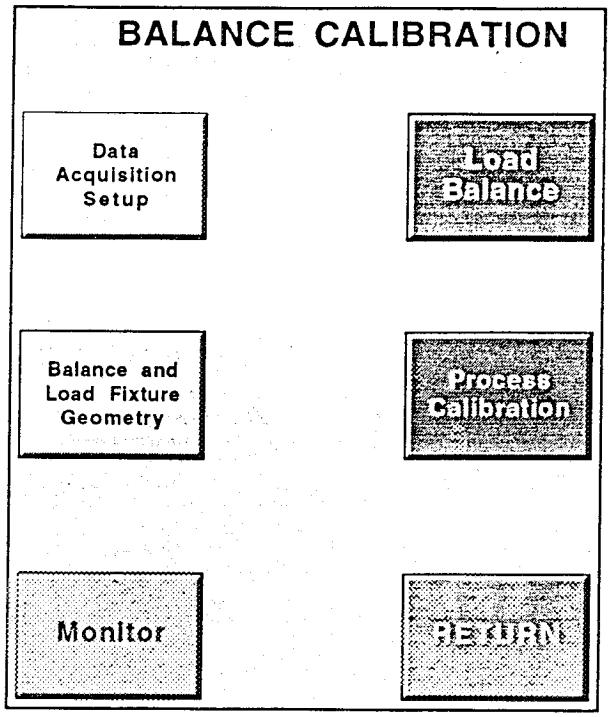

a) "Calibrate Balance" Panel

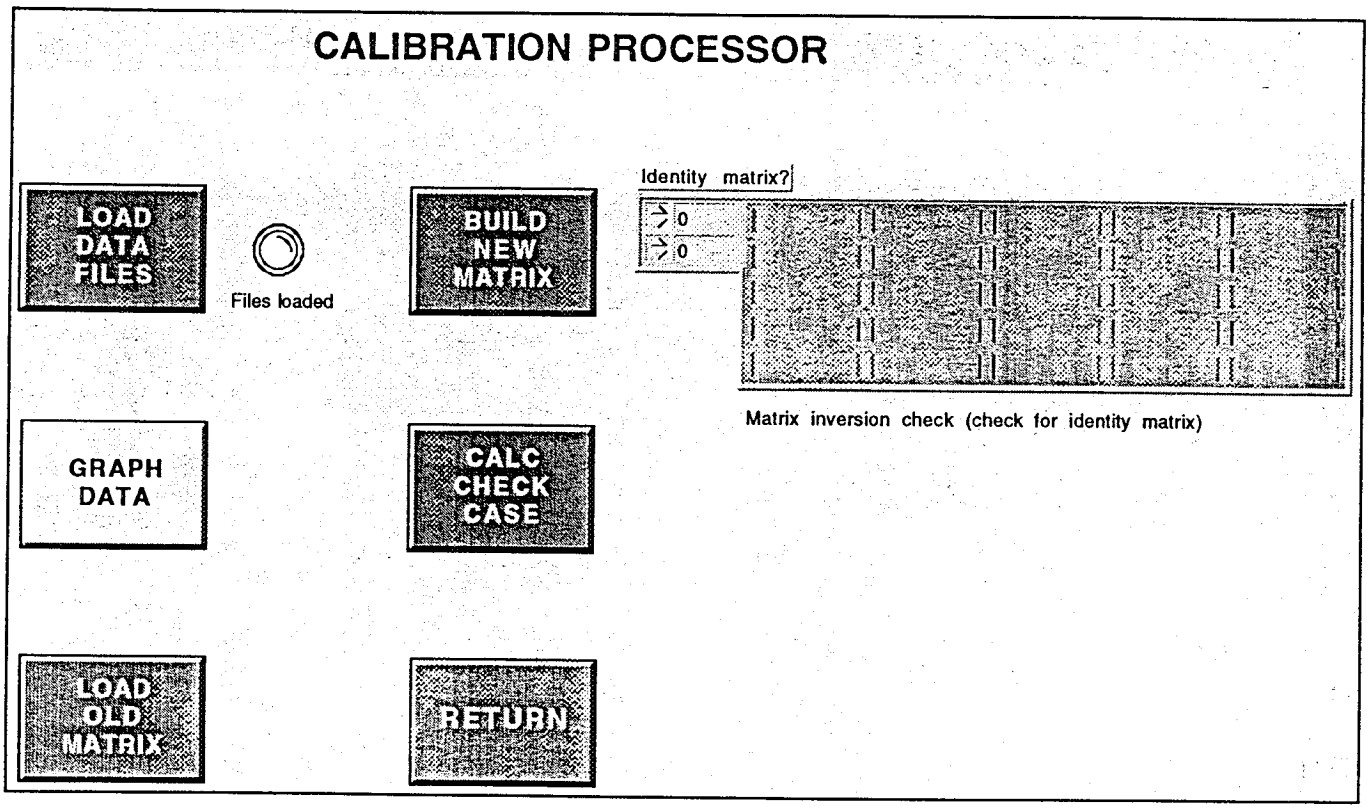

b) "Process Calibration" Panel

Figure 13 - Front Panels of the Calibration Software

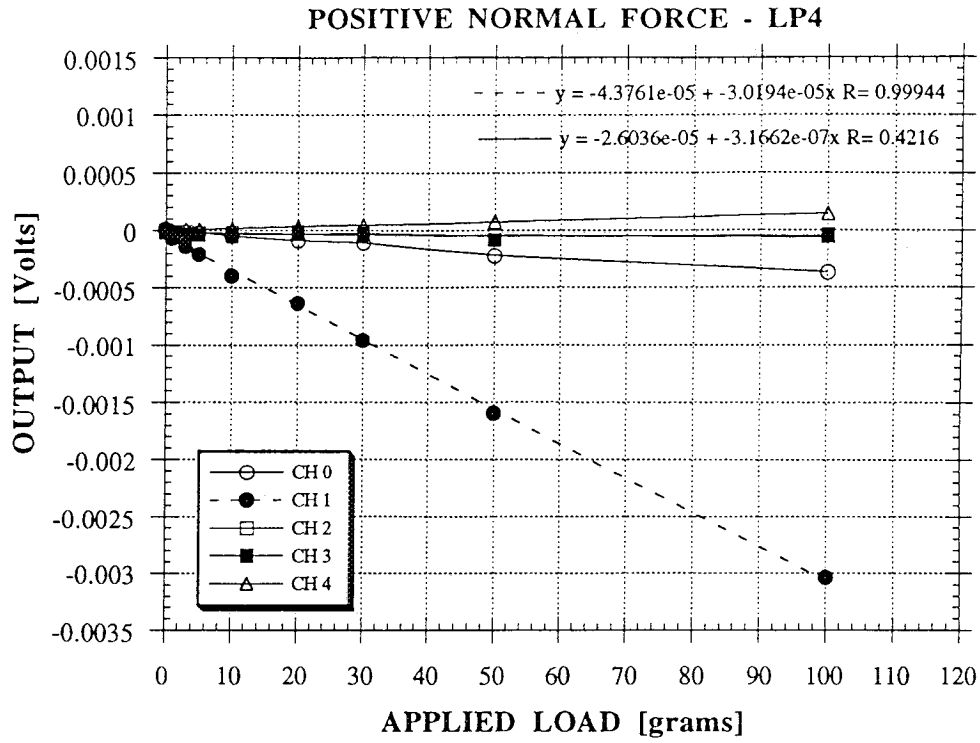

a) Balance Response to a Positive Normal Force

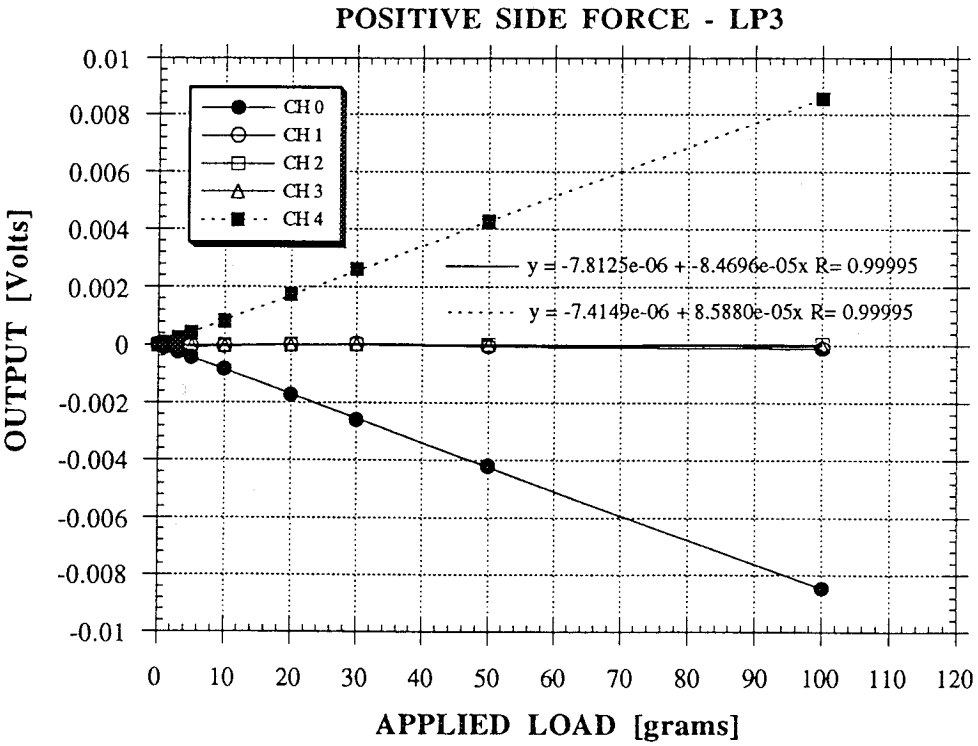

b) Balance Response to a Positive Side Force

Figure 14 - Examples of Loading Cases During Balance Calibration

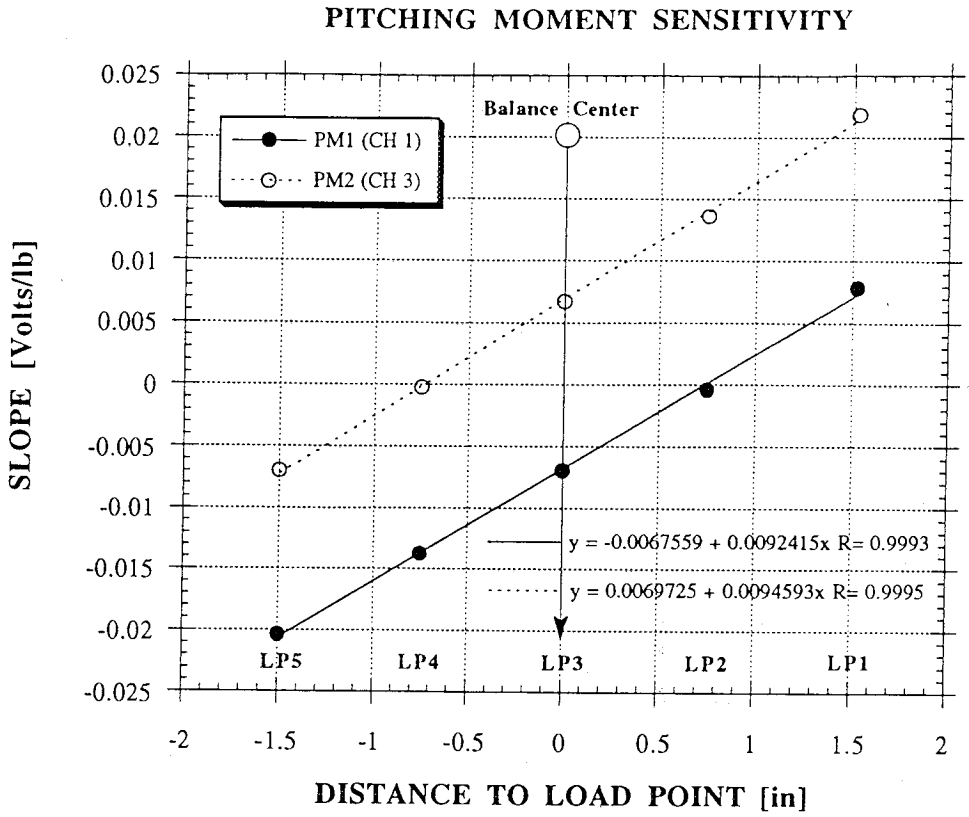

a) Pitching Moment Sensitivity

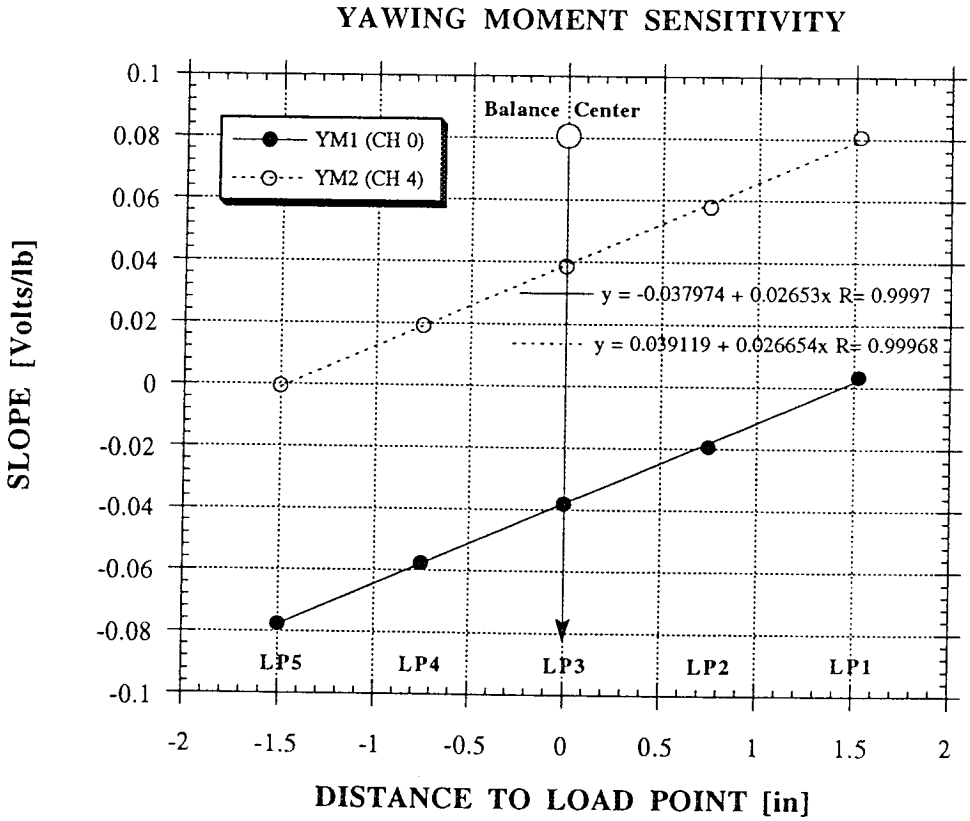

b) Yawing Moment Sensitivity

Figure 15 - Sensitivity to Primary Loads

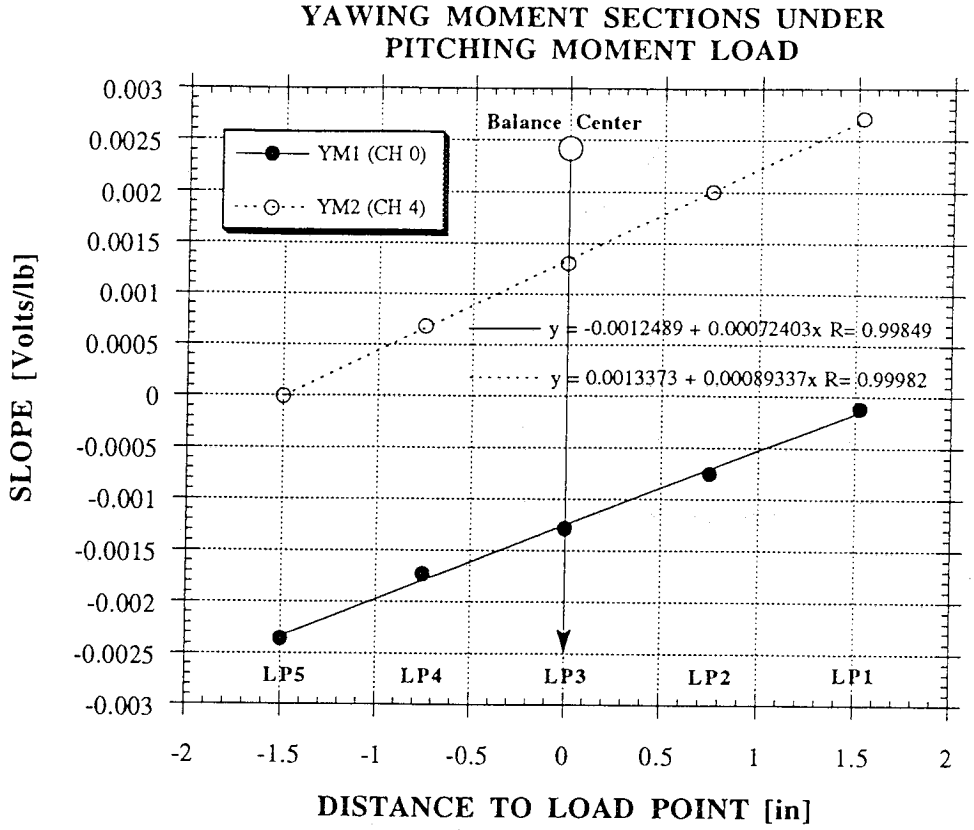

Figure 16 - Example of Balance Interactions (Yawing Moment Sections Under Pitching Moment Load)

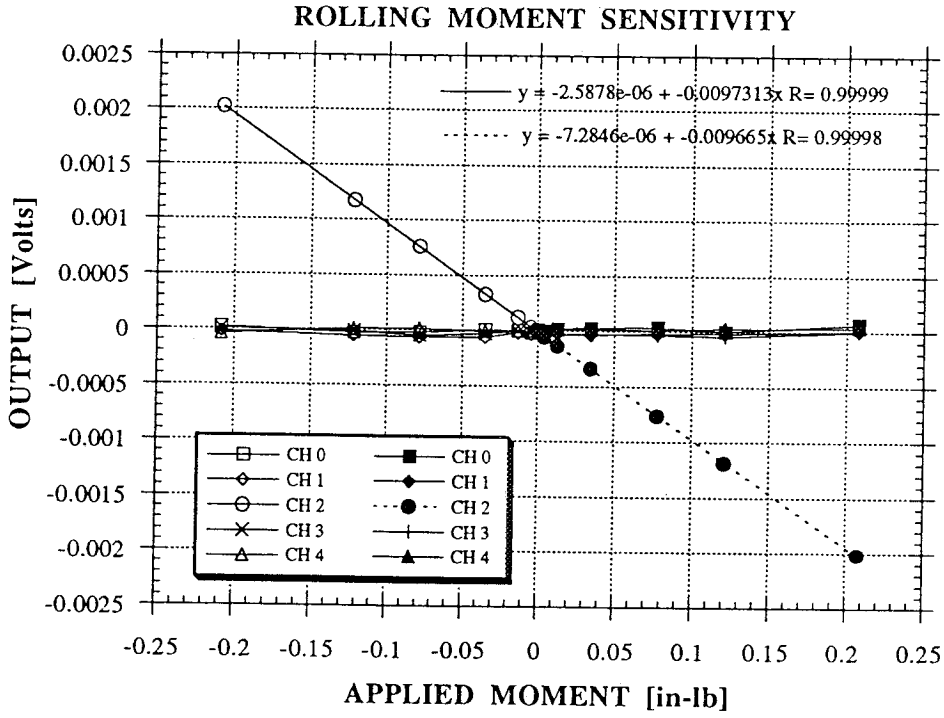

Figure 17 - Rolling Moment Sensitivity

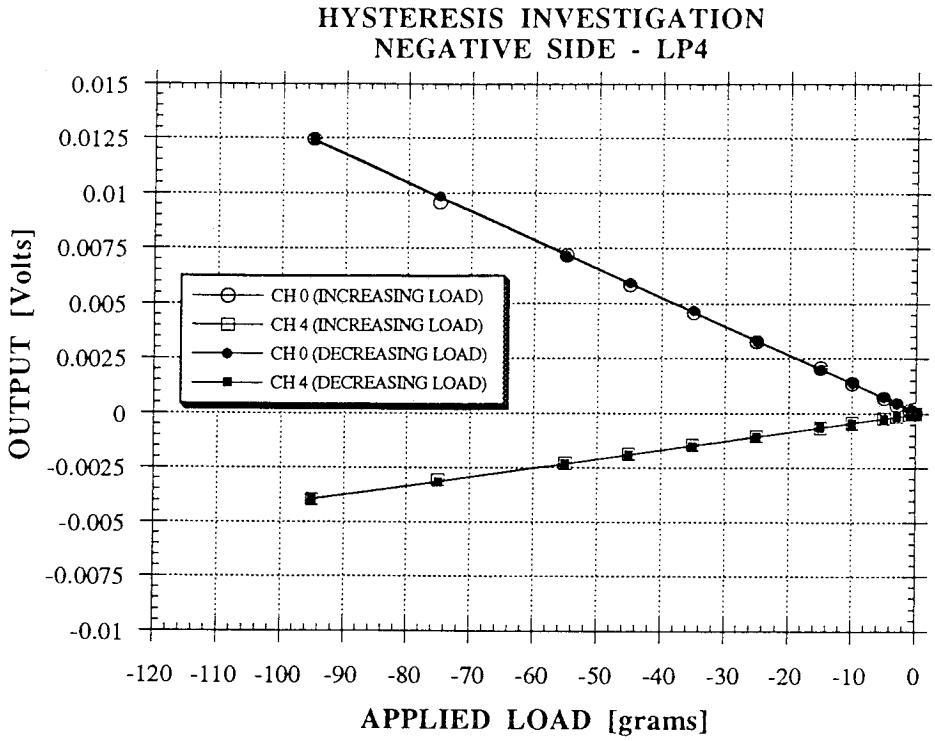

a) Side Force Load

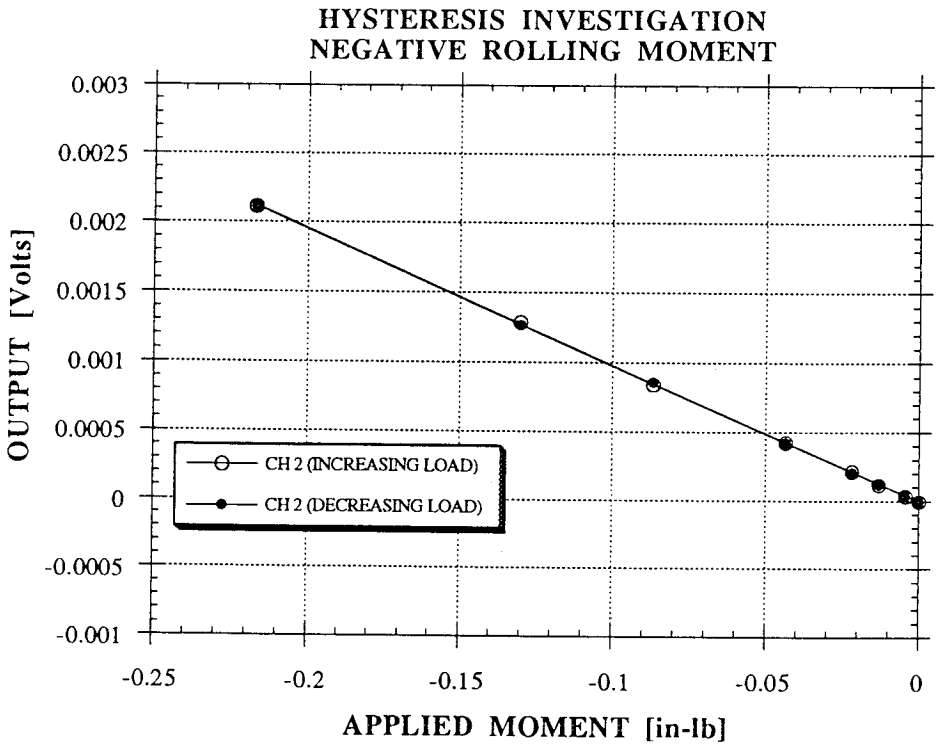

b) Rolling Moment Load

Figure 18 - Hysteresis Investigation

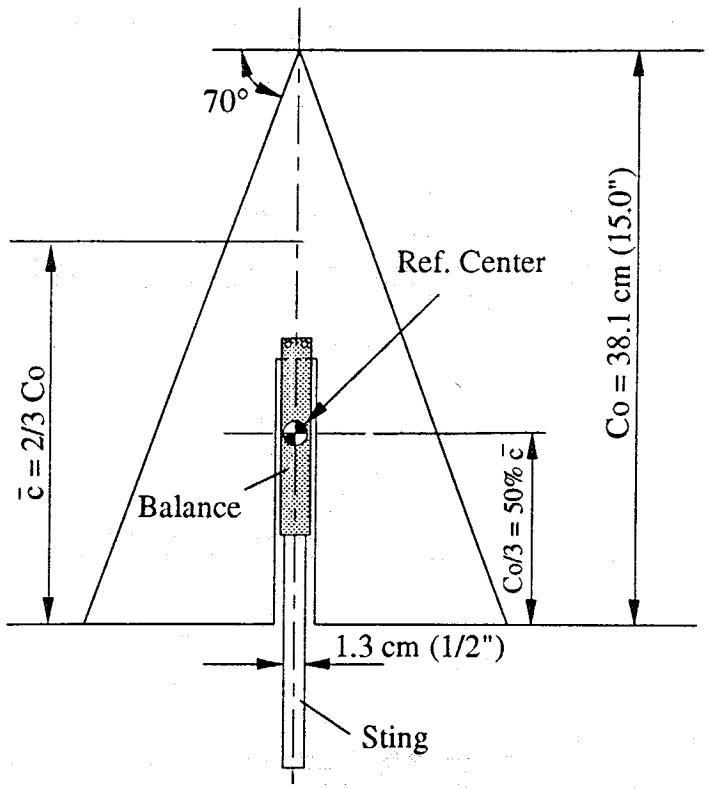

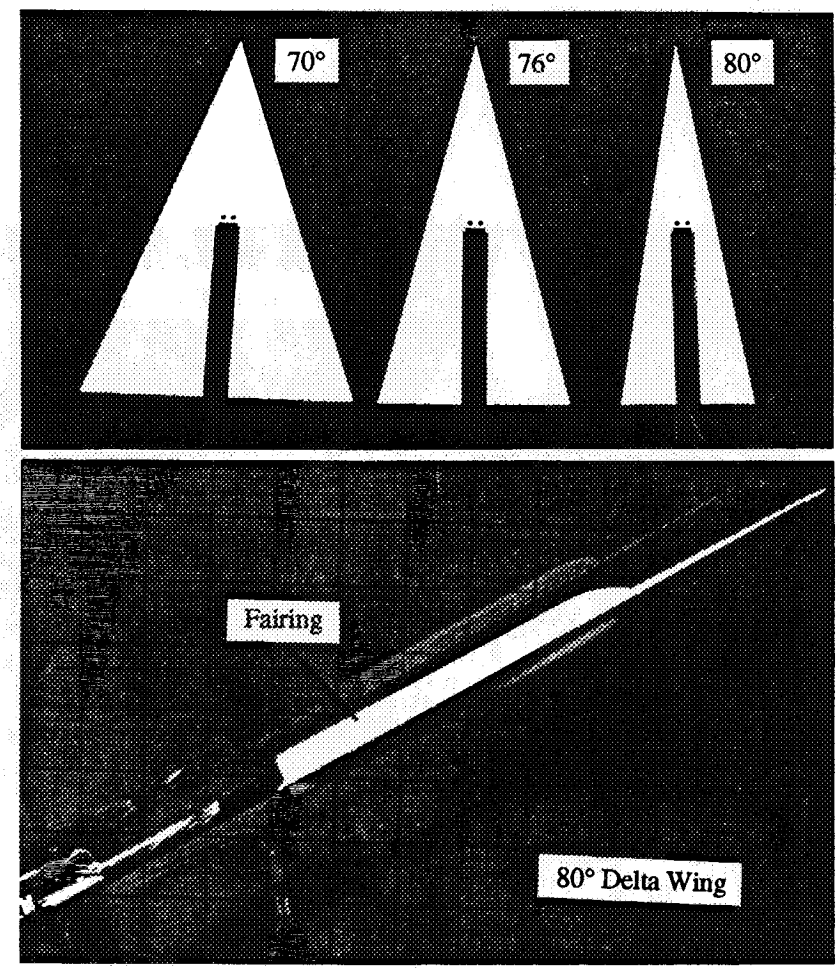

Figure 19 - Delta Wing Models

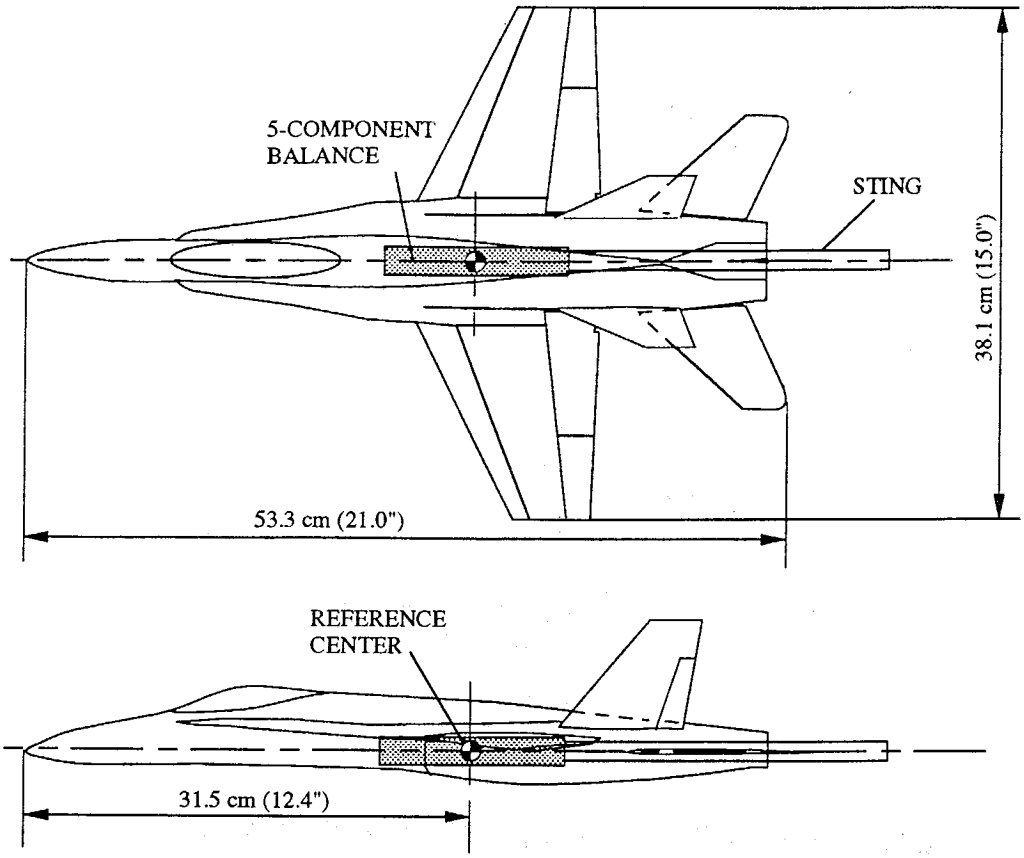

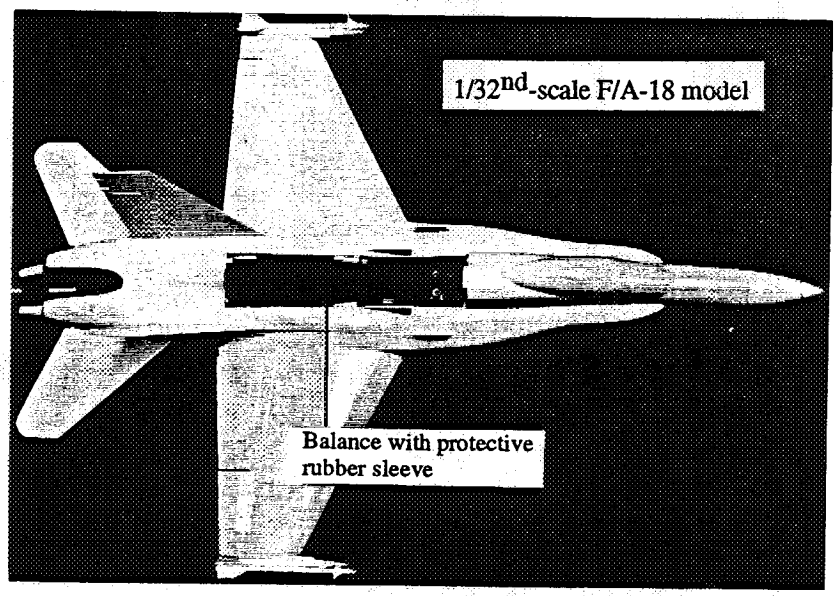

Figure 20 - 1/32nd-Scale F/A-18 Model

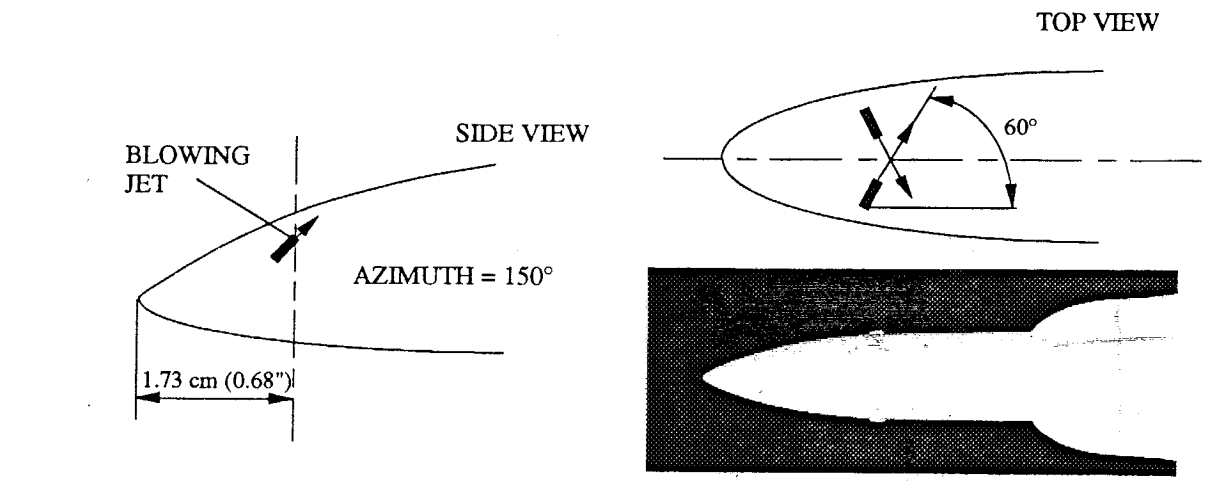

a) JET BLOWING

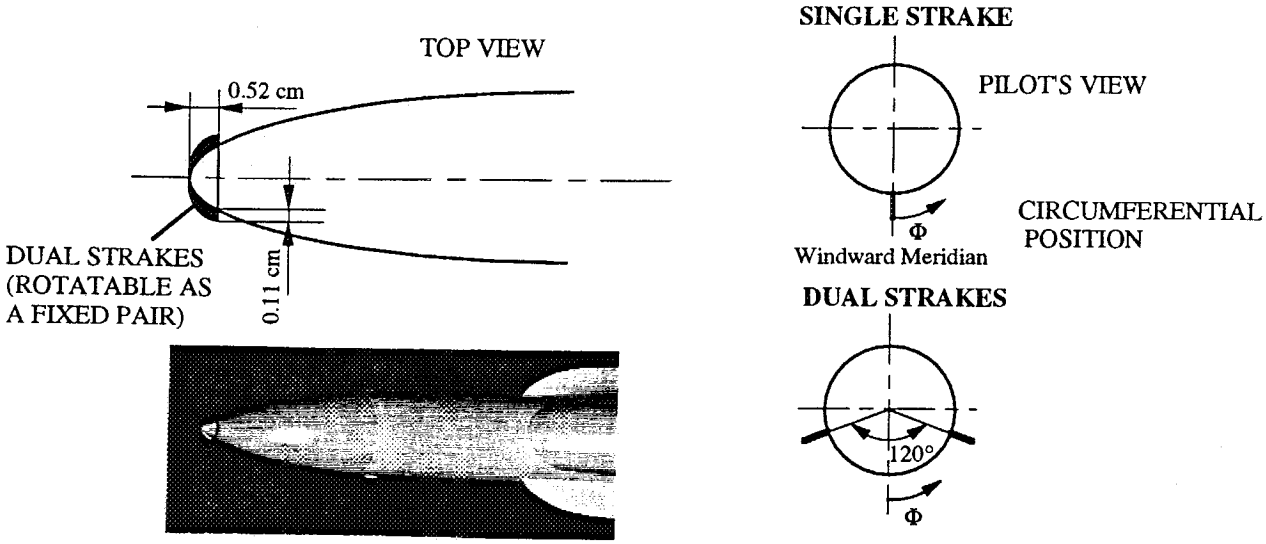

b) ROTATABLE TIP-STRAKES

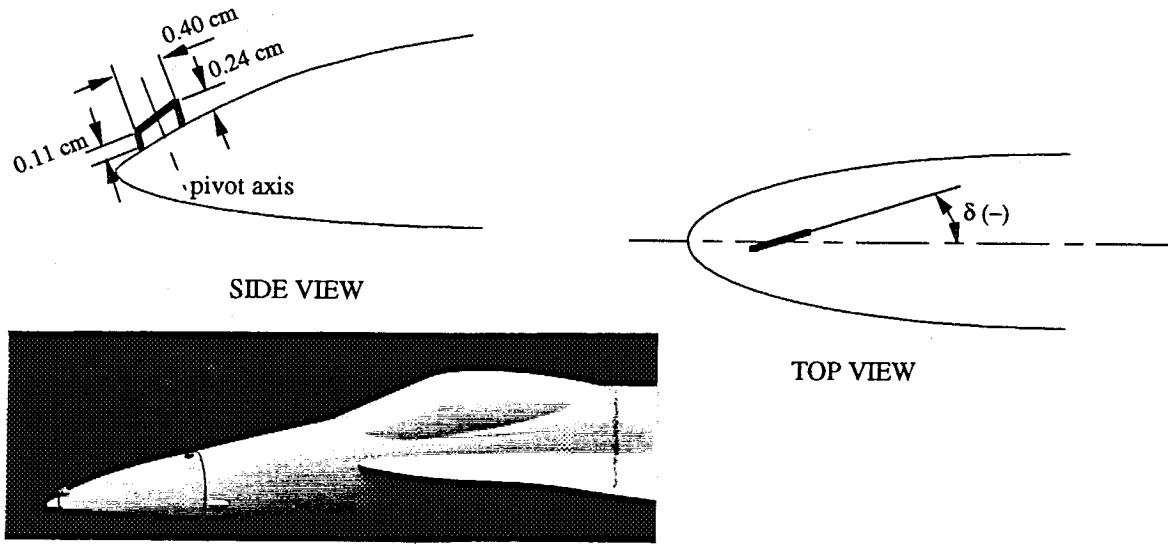

c) VERTICAL NOSE STRAKE

Figure 21 - Schematics of Forebody Vortex Control (FVC) Techniques Investigated

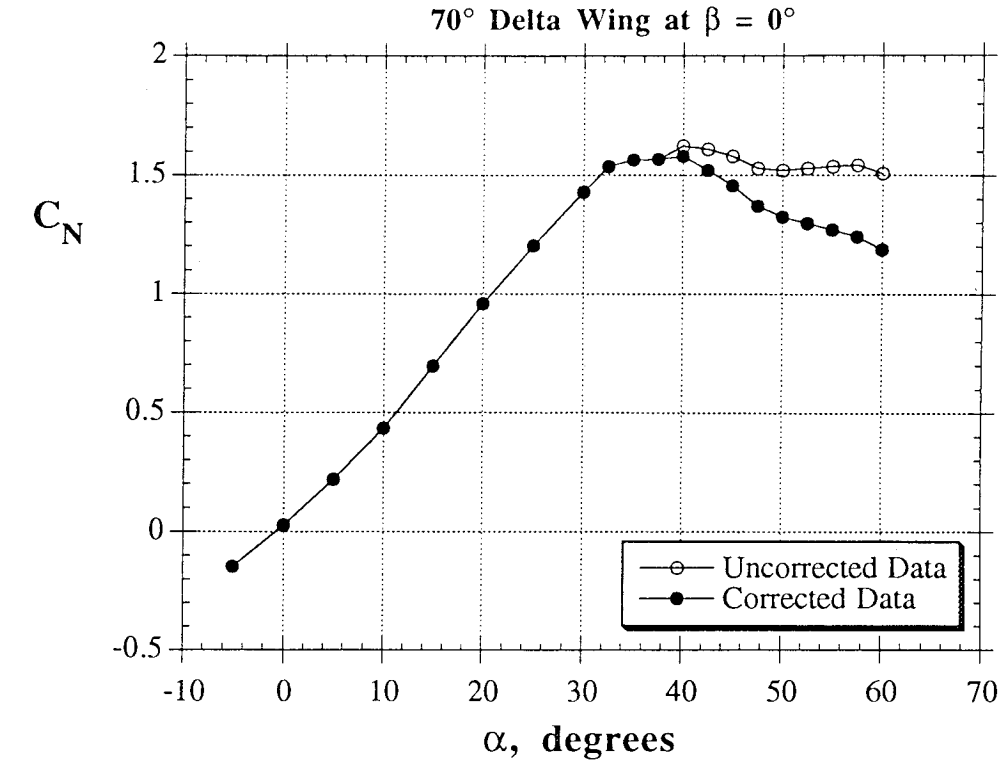

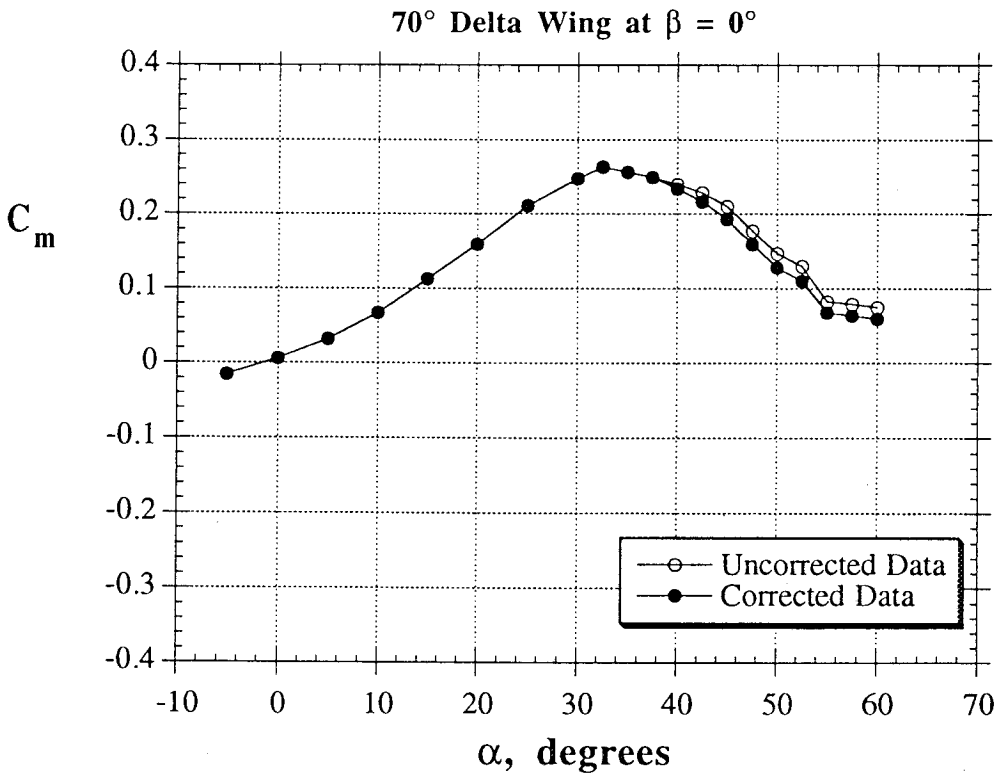

Figure 22 - Effect of Boundary Corrections on Forces and Moments (70° Delta Wing at β = 0°)

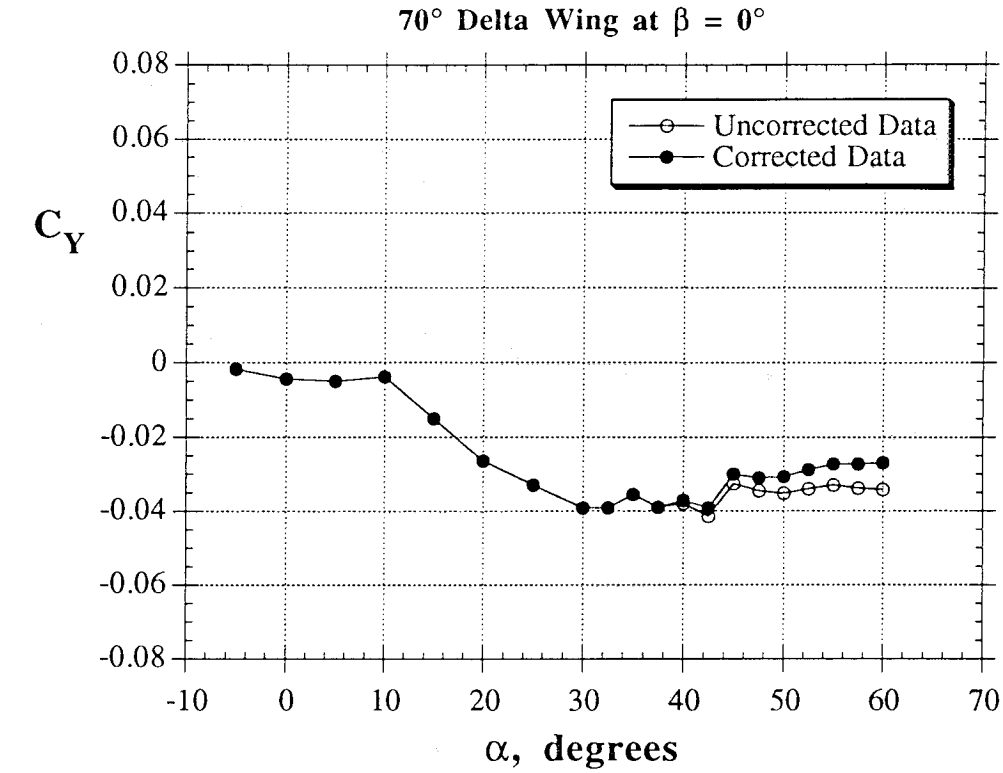

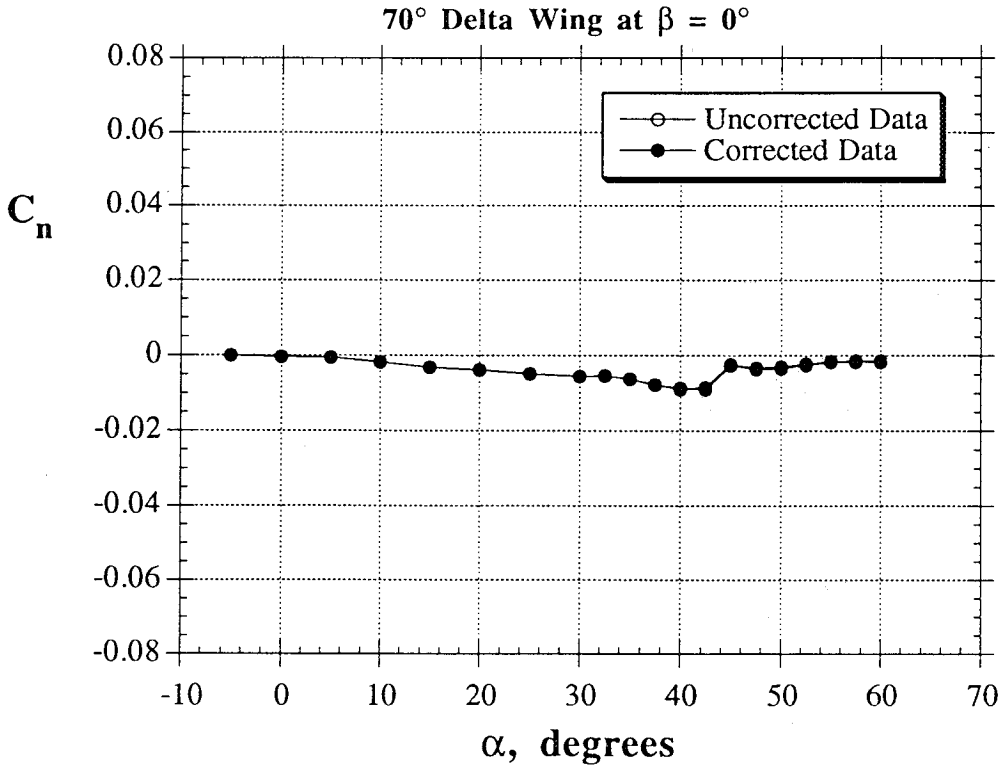

Figure 22 - Continued

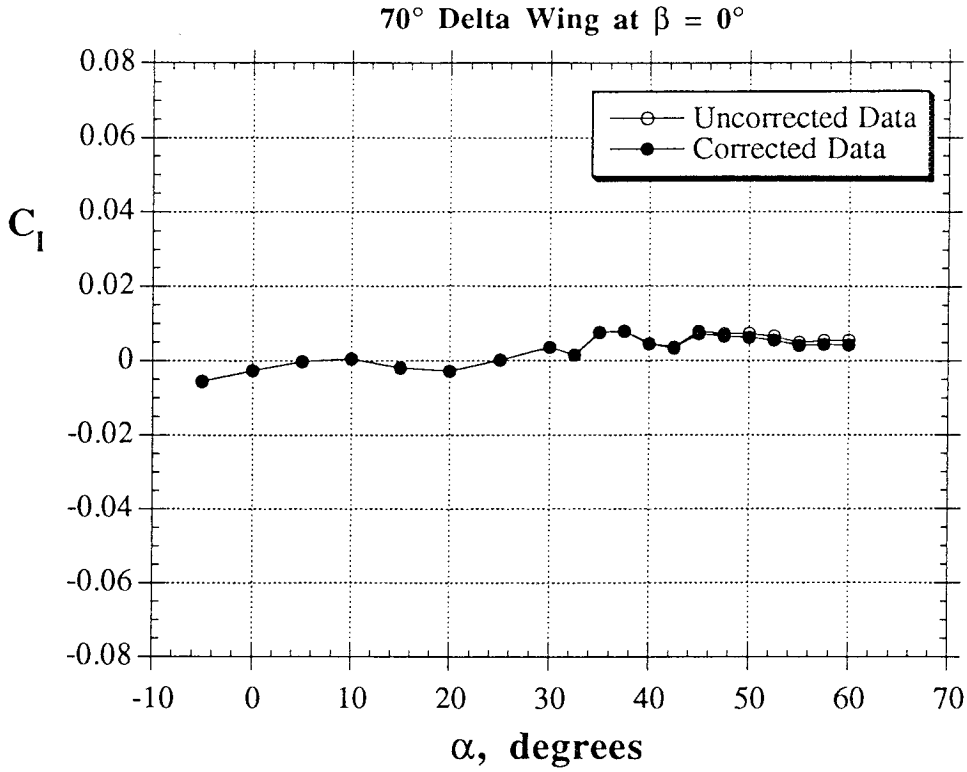

Figure 22 - Concluded

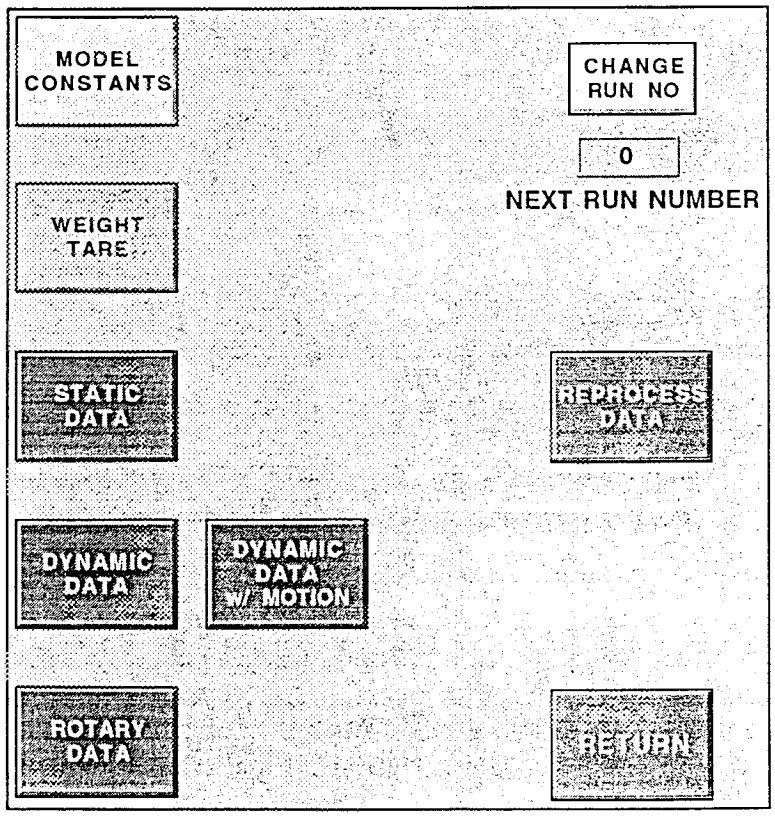

a) "Use Balance" Panel

Figure 23 - Software Panels Used During Static Tests

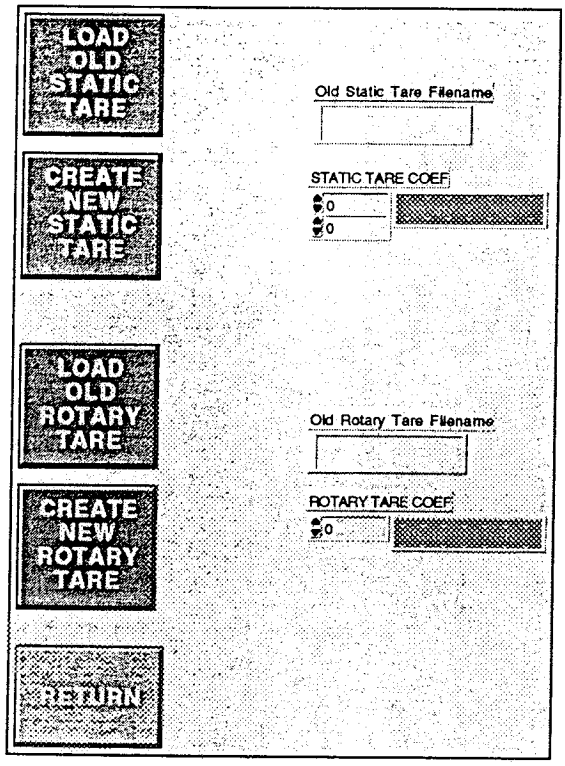

b) "Weight Tare" Panel

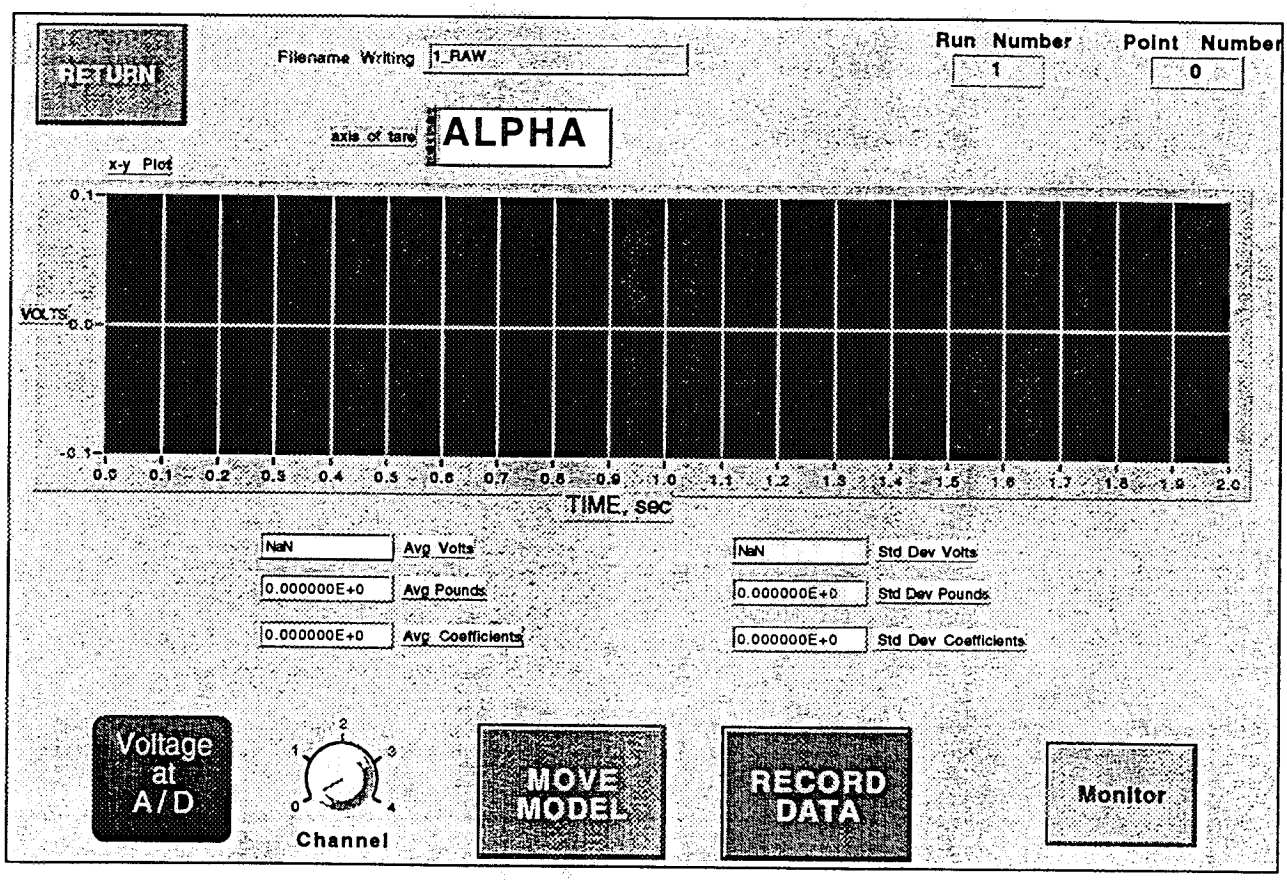

c) "Static Data" Panel

Figure 23 - Continued

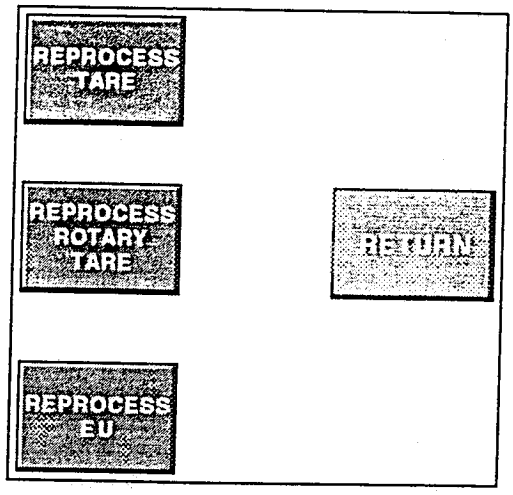

d) "Reproccess Data" Panel

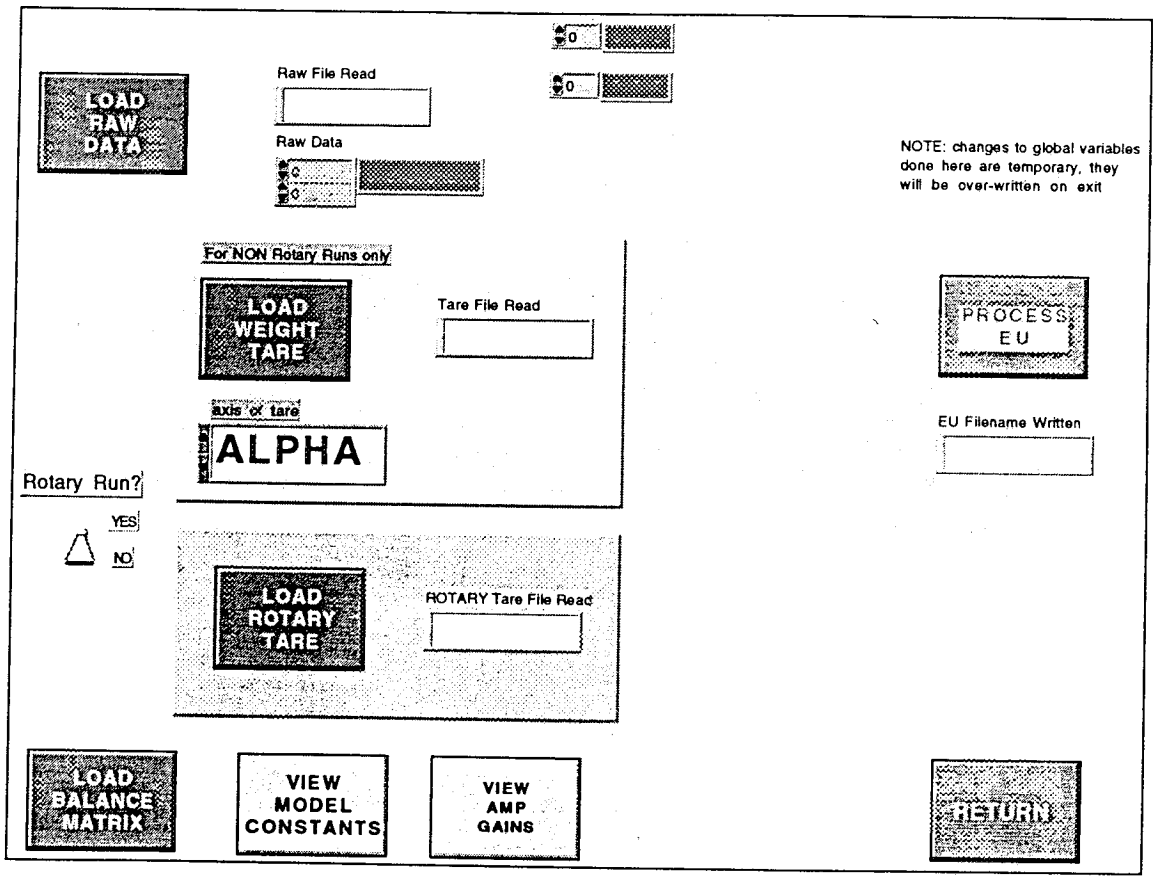

e) "Reproccess EU" Panel

Figure 23 - Concluded

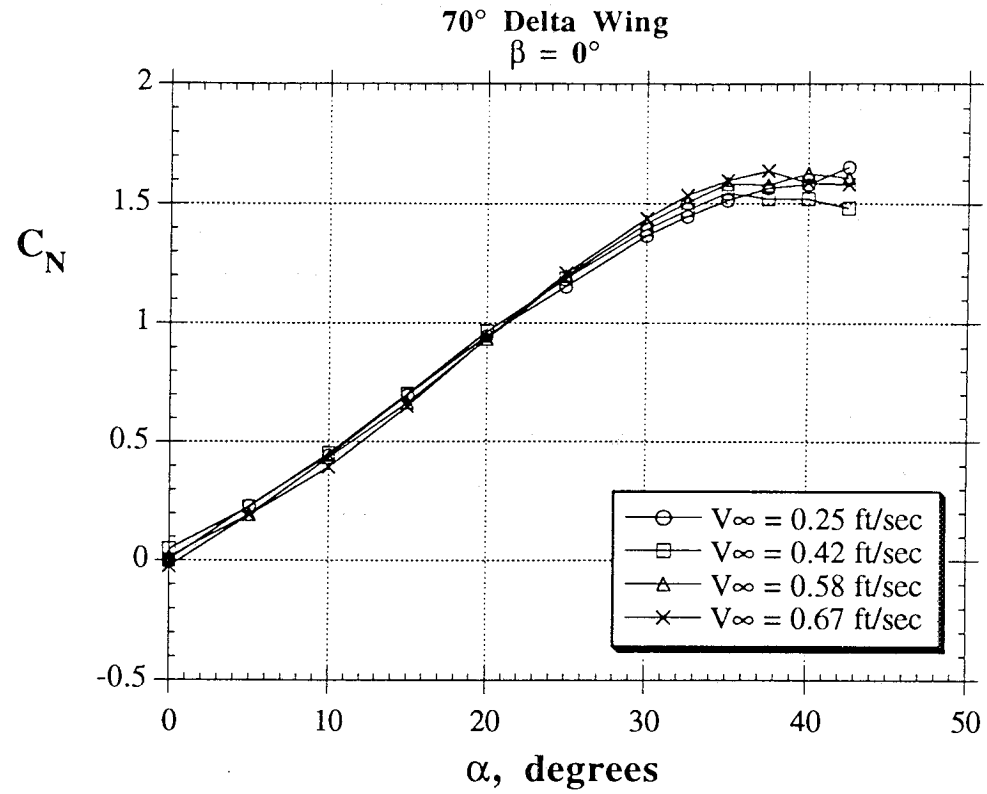

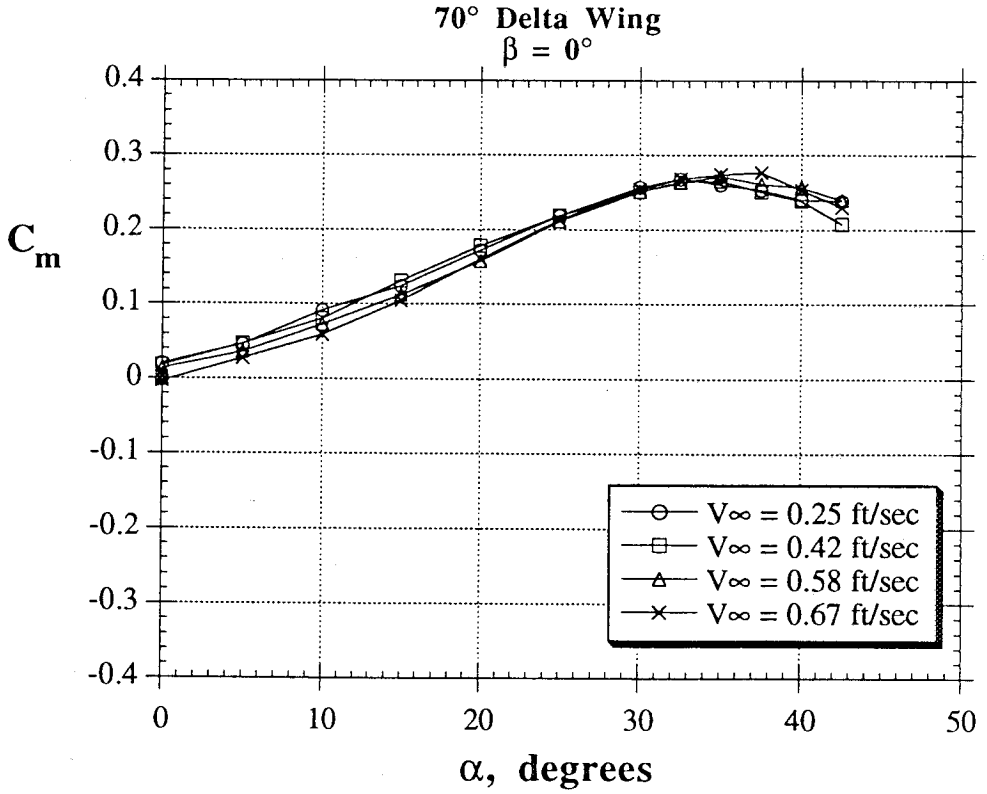

Figure 24 - Effect of Free Stream Velocity on Forces and Moments (70° Delta Wing at β = 0°)

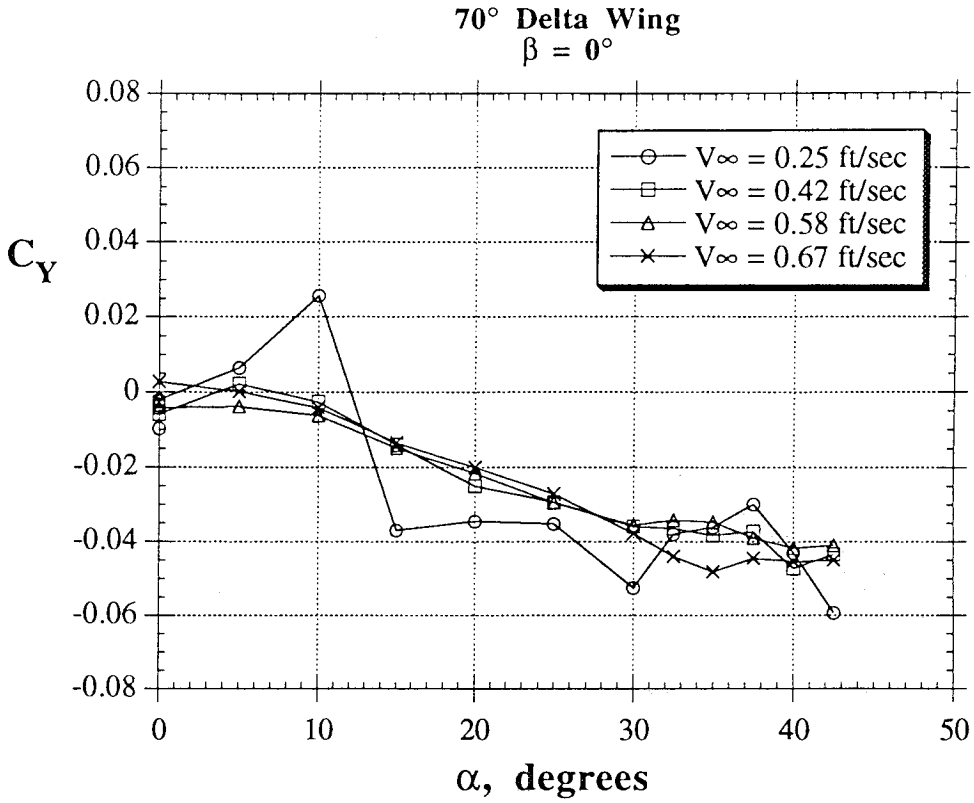

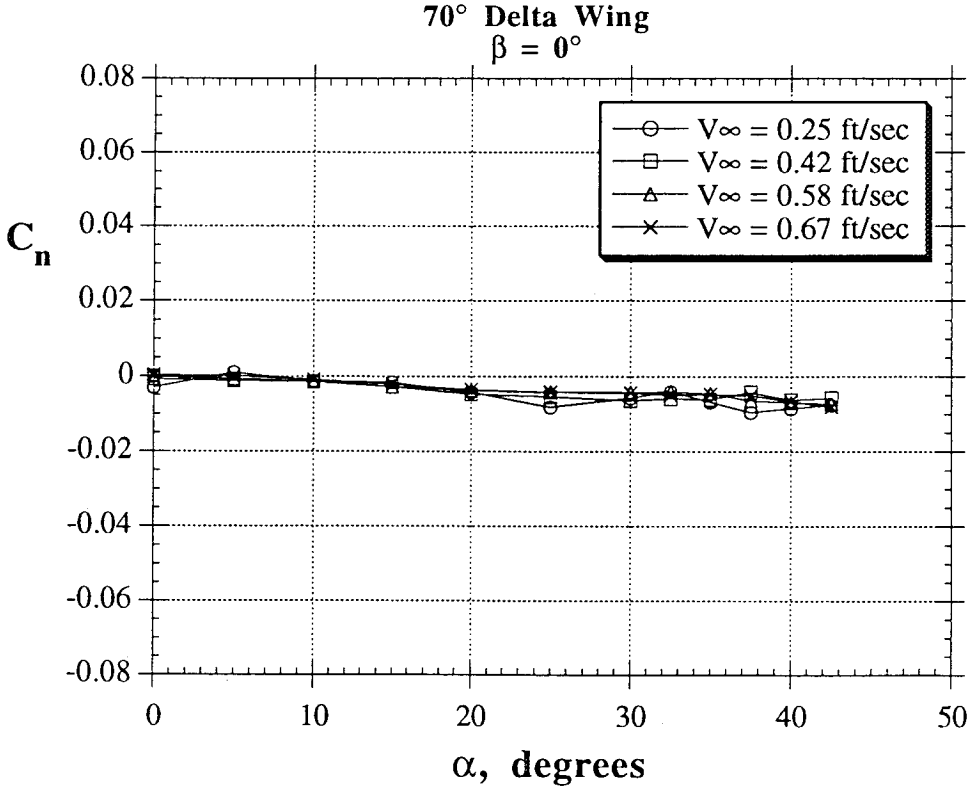

Figure 24 - Continued

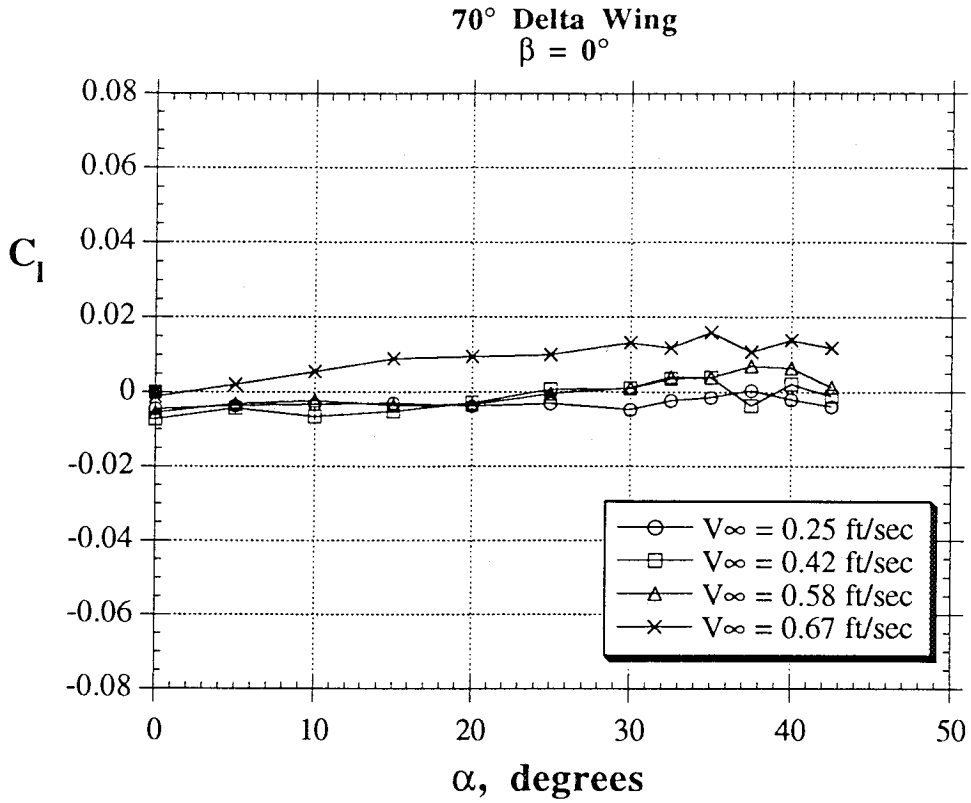

Figure 24 - Concluded

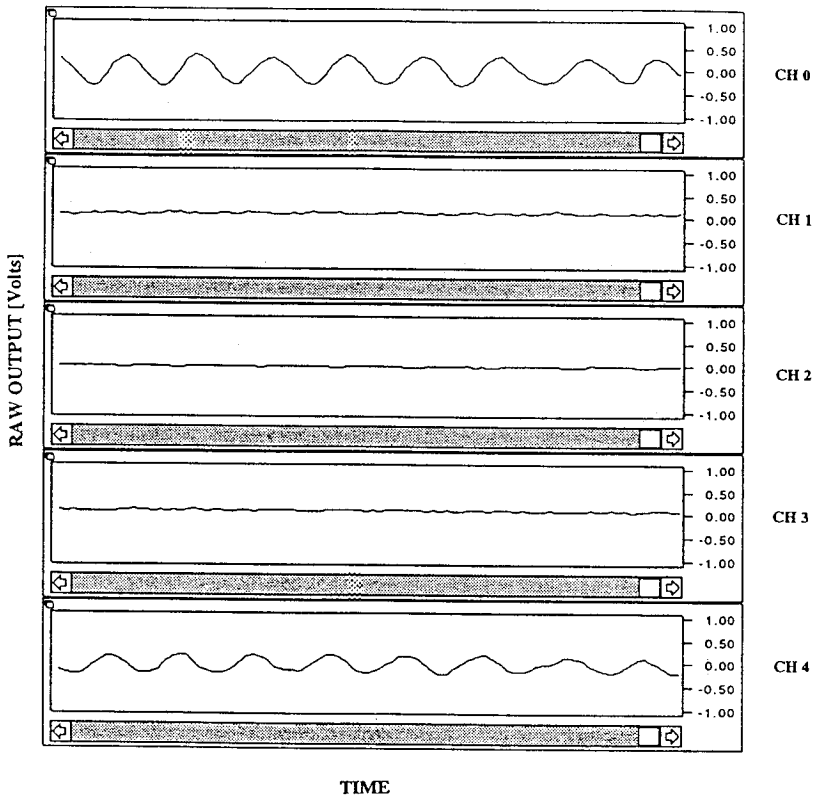

Figure 25 - Time Histories of Raw Voltages from the 5 Balance Channels at Different Free Stream Velocities

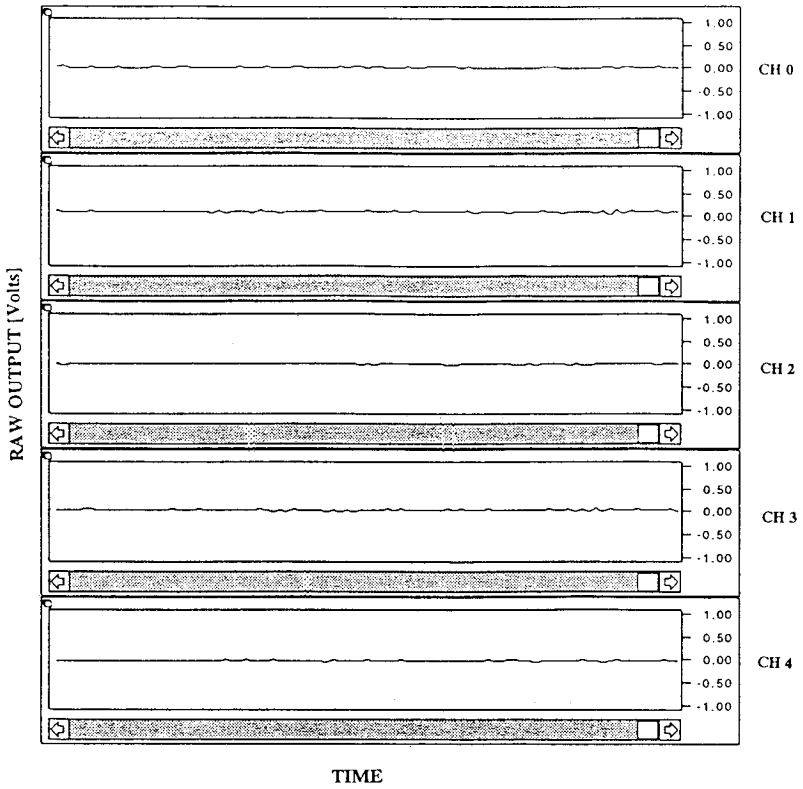

b) $\alpha = 20°$
$V_\infty = 0.21$ ft/sec

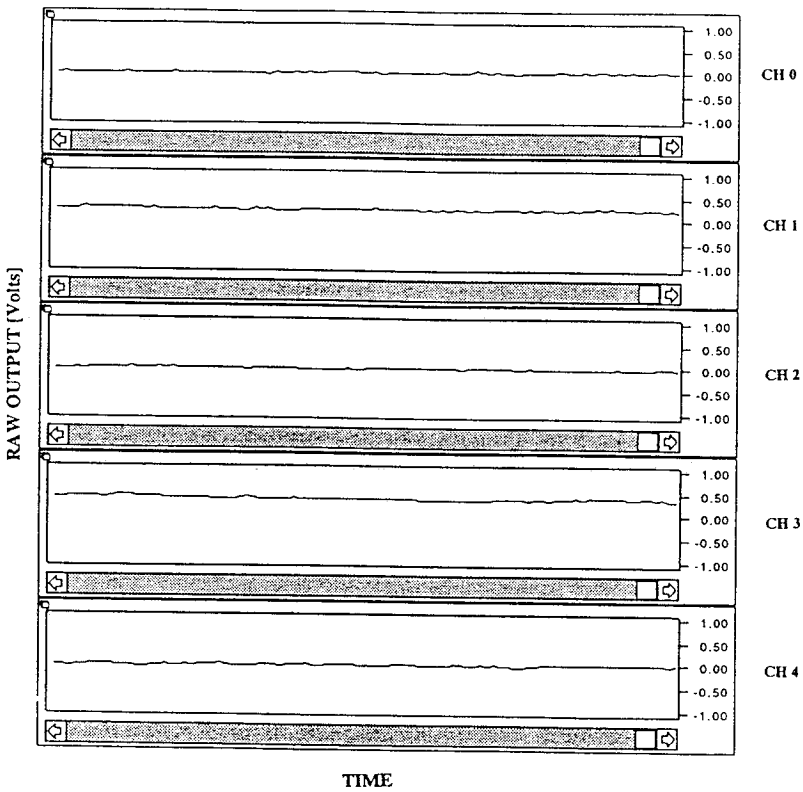

c) $\alpha = 20°$
$V_\infty = 0.42$ ft/sec

Figure 25 - Continued

d) $\alpha = 20°$
$V_\infty = 0.25$ ft/sec

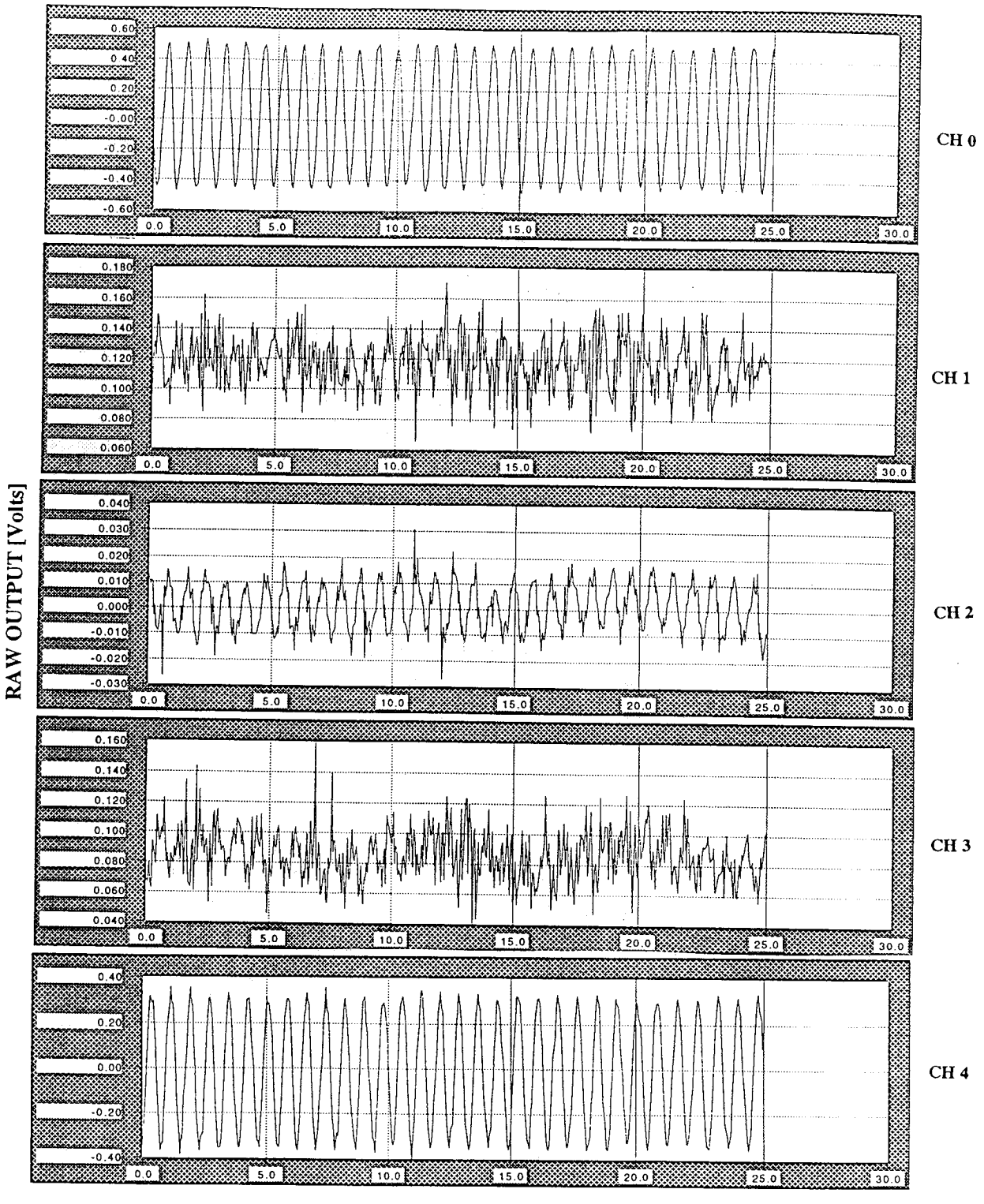

Figure 25 - Concluded

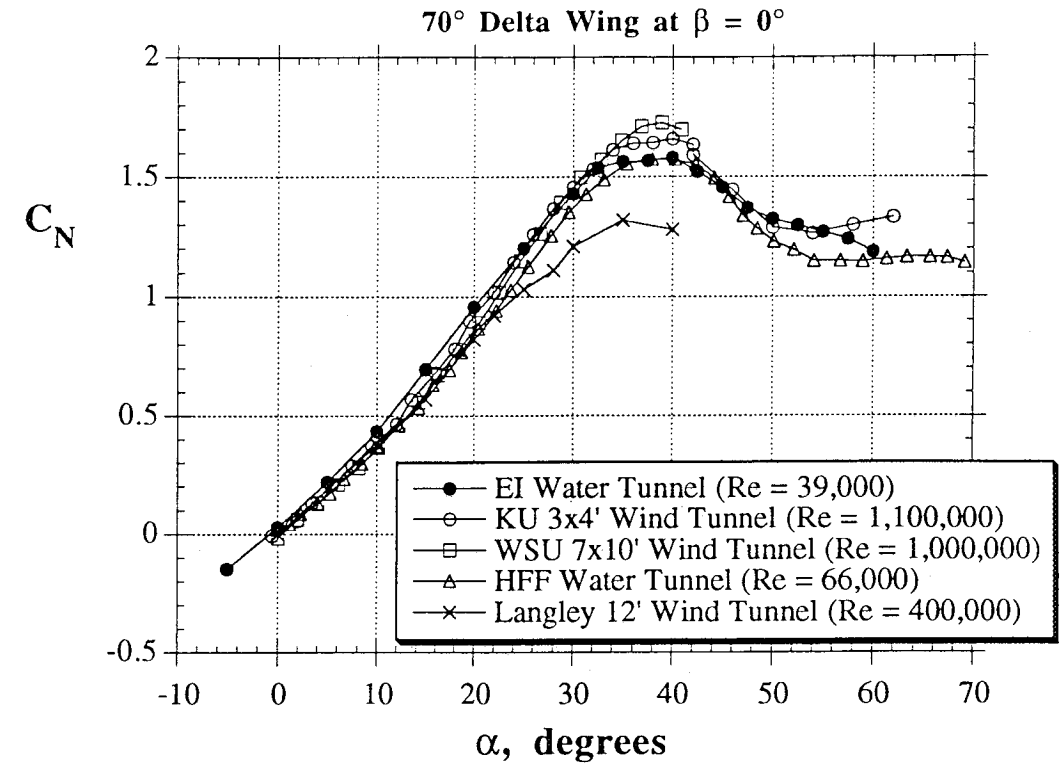

a) Normal Force

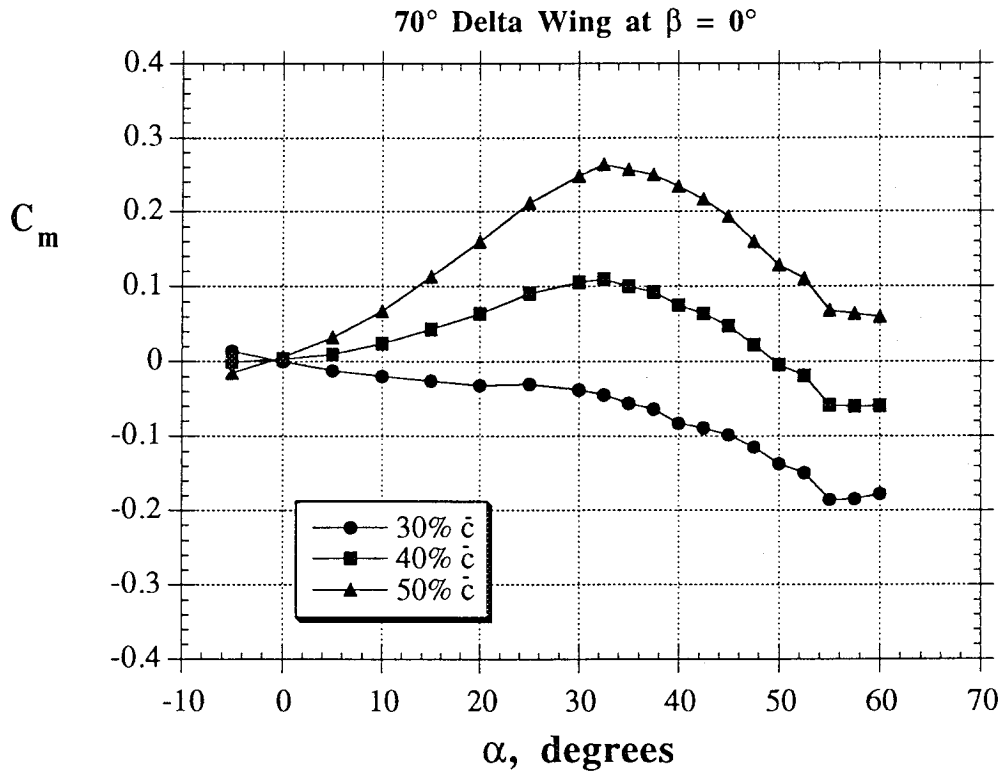

b) Pitching Moment at Different Reference Centers

Figure 26 - Longitudinal Characteristics of the 70° Delta Wing at β = 0° (Comparison with Refs. 5, 8, 9, 10)

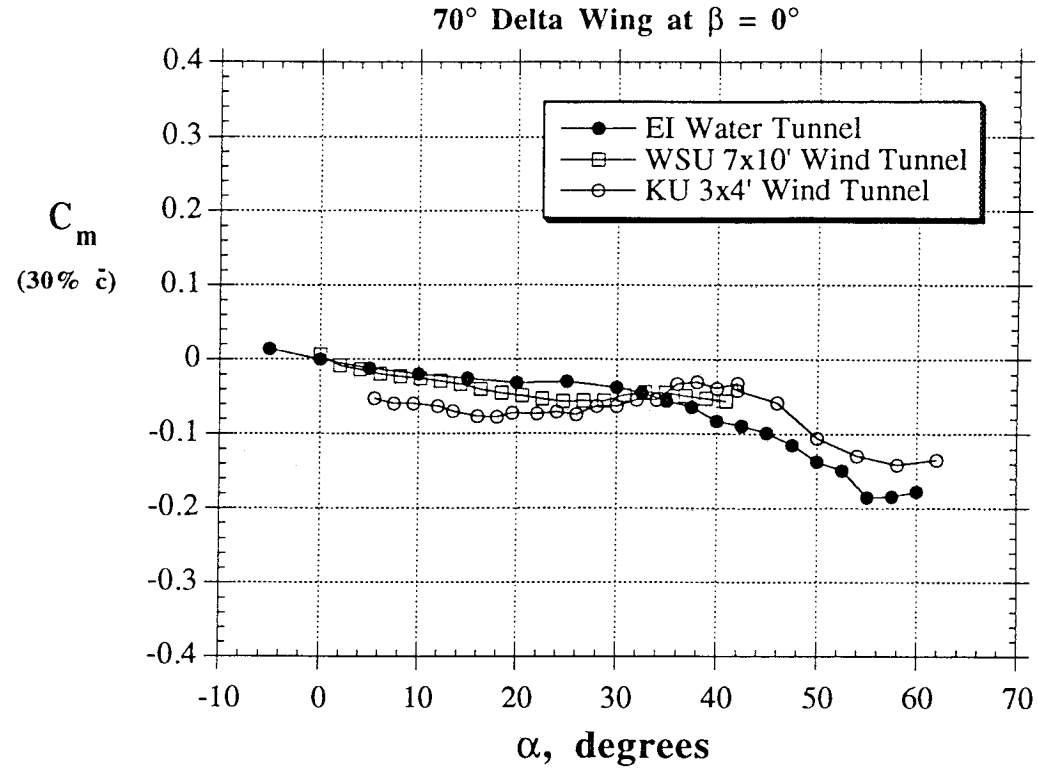

c) Pitching Moment at 30% $\bar{c}$

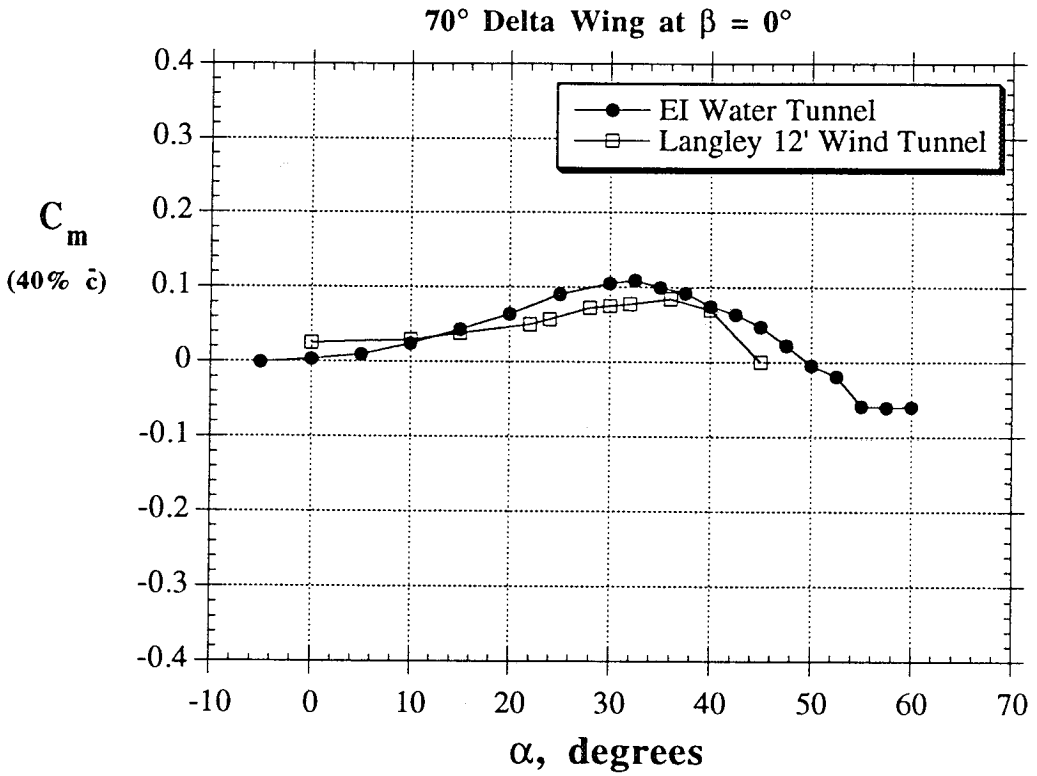

d) Pitching Moment at 40% $\bar{c}$

Figure 26 - Concluded

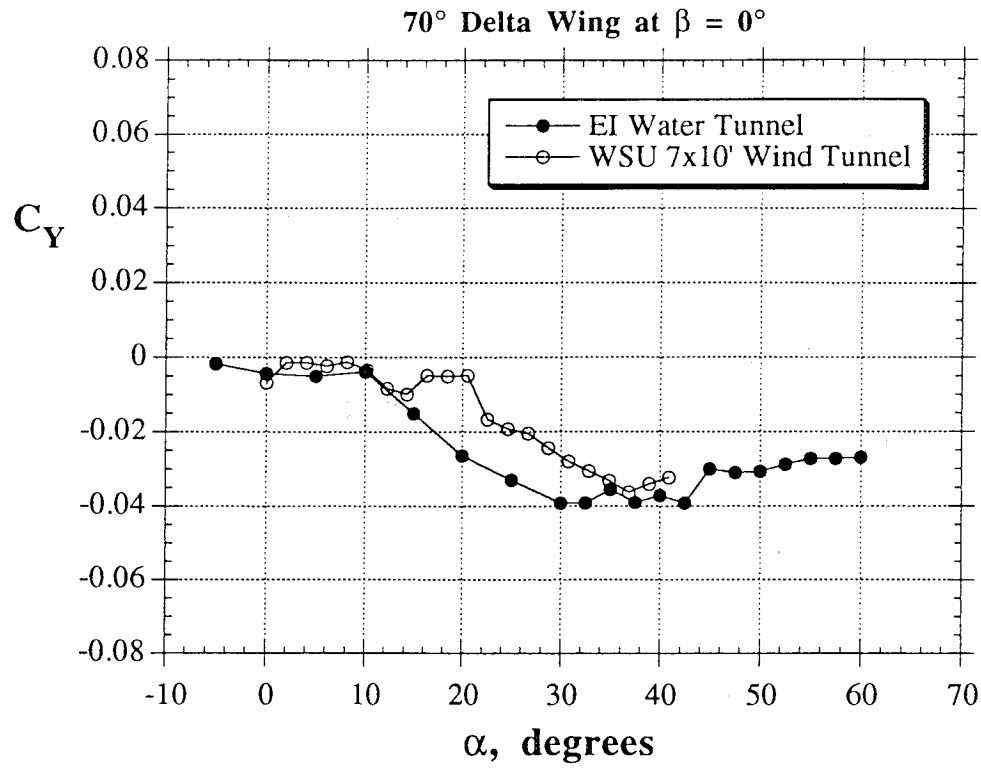

Figure 27 - Side Force Changes on the 70° Delta Wing at $\beta = 0°$ (Comparison with Ref. 9)

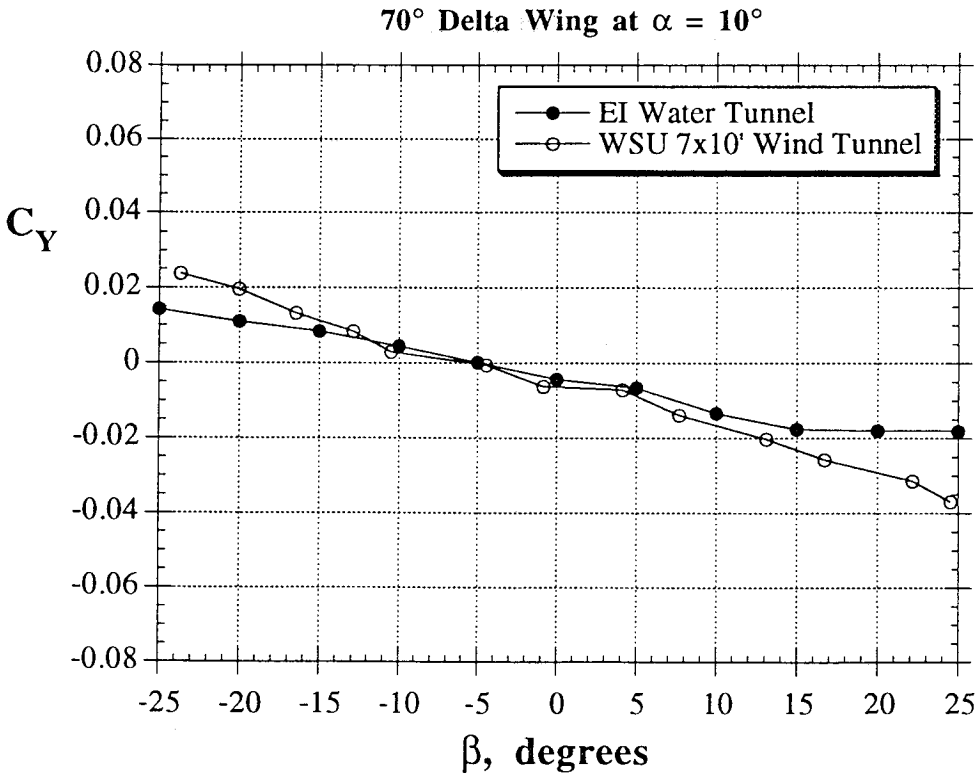

Figure 28 - Effect of Sideslip Variations on the Directional Characteristics of the 70° Delta Wing at $\alpha = 10°$ (Comparison with Ref. 9)

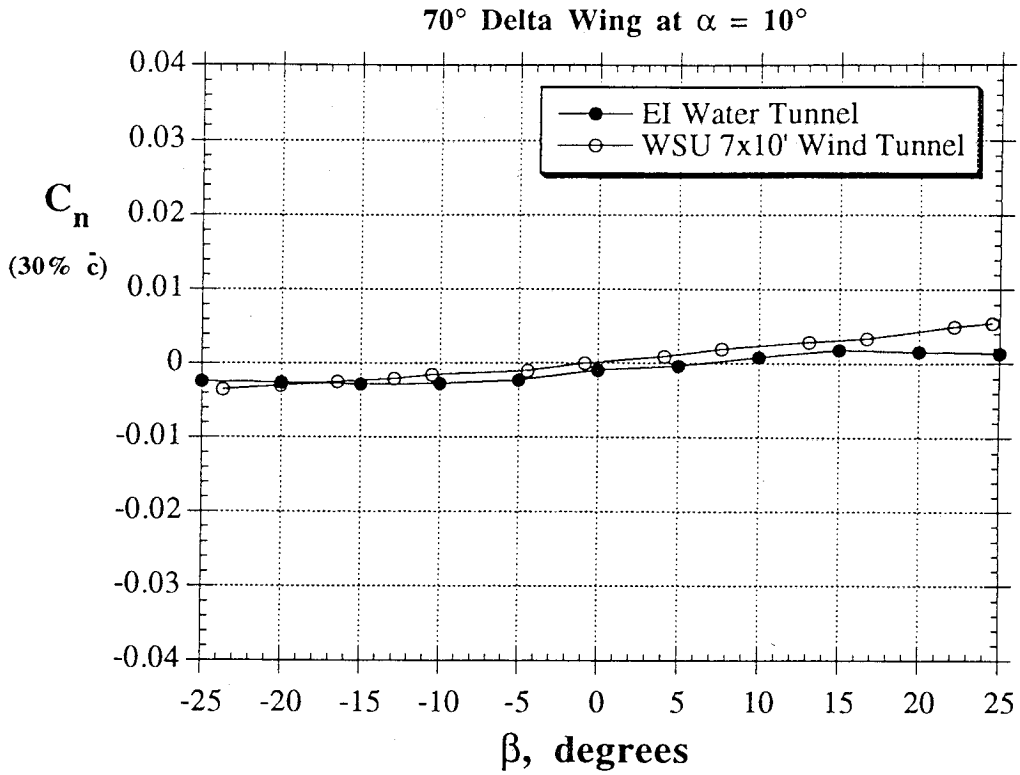

Figure 28 - Concluded

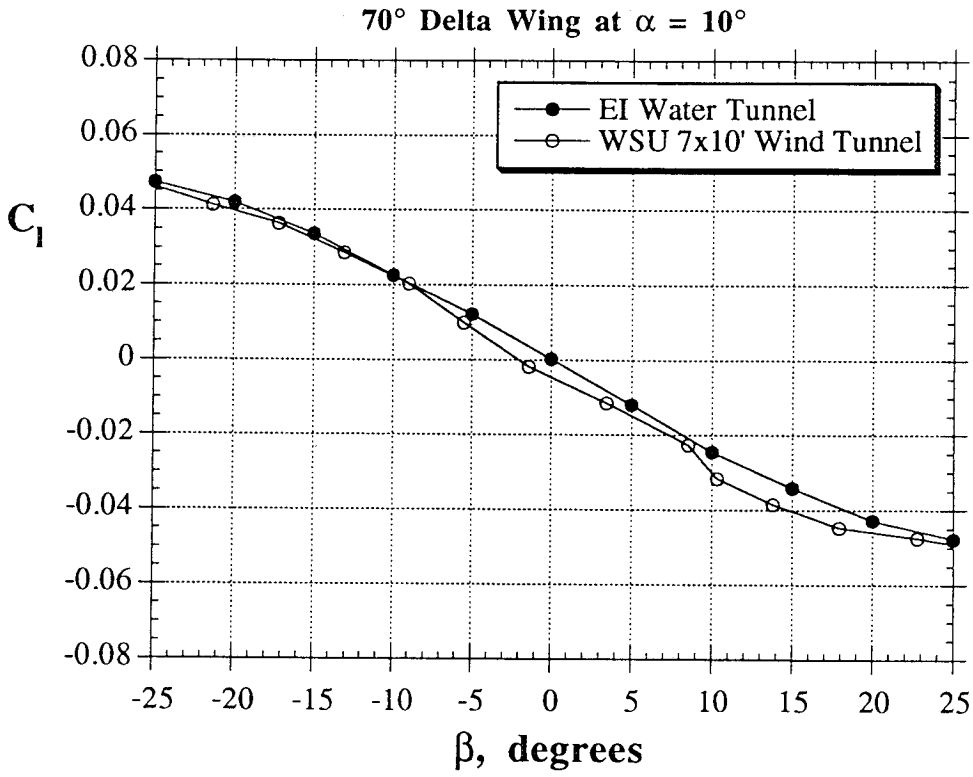

a) α = 10°

Figure 29 - Effect of Sideslip Variations on the Rolling Moment of the 70° Delta Wing (Comparison with Ref. 11)

b) $\alpha = 20°$

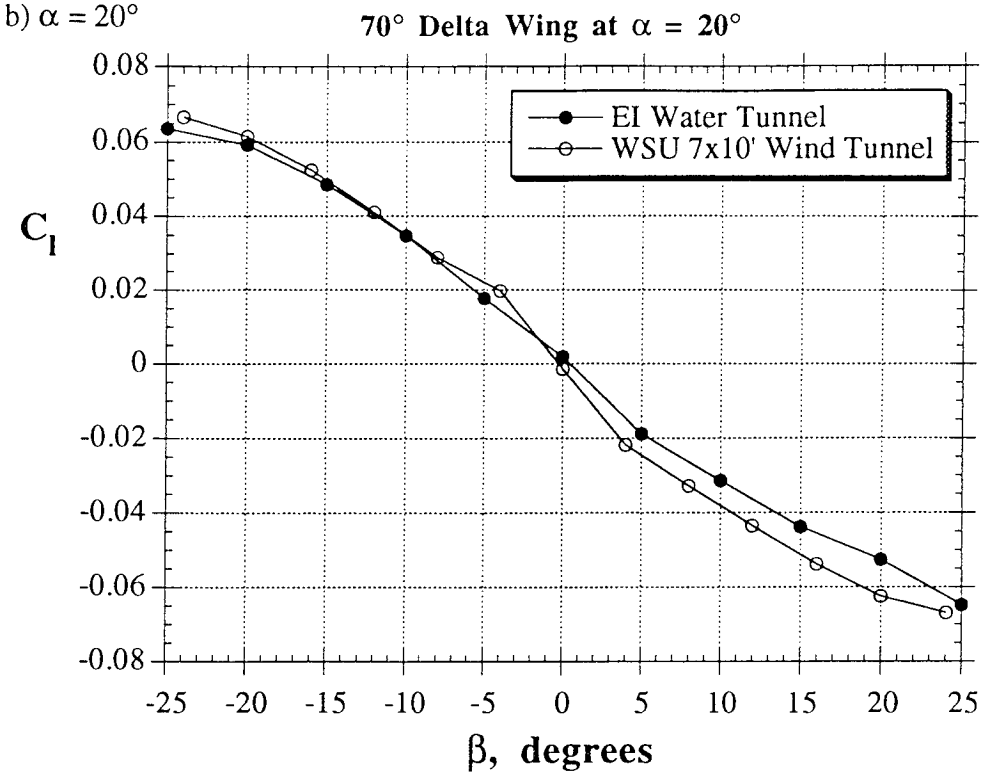

Figure 29 - Concluded

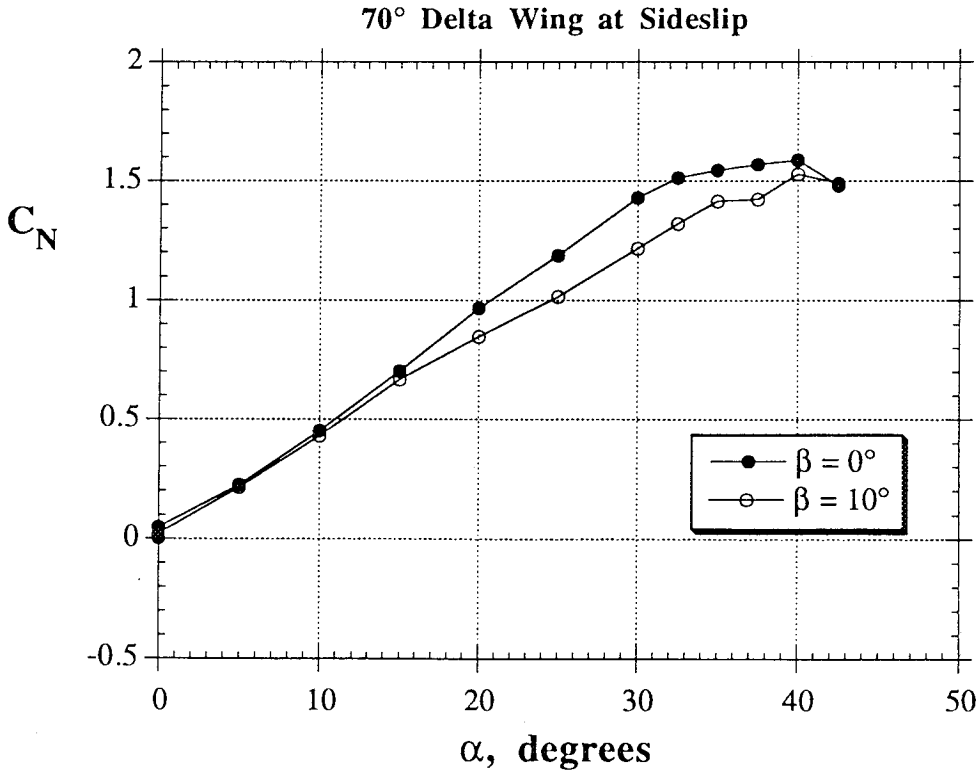

Figure 30 - Effect of Sideslip Angle ($\beta = 10°$) on Forces and Moments (70° Delta Wing)

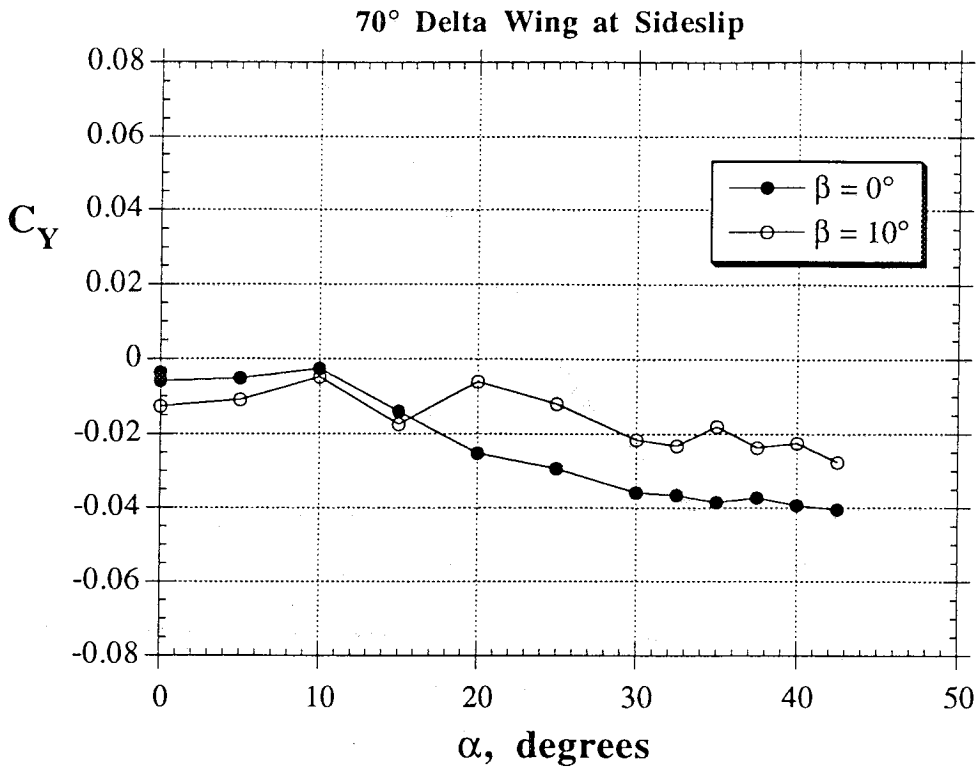

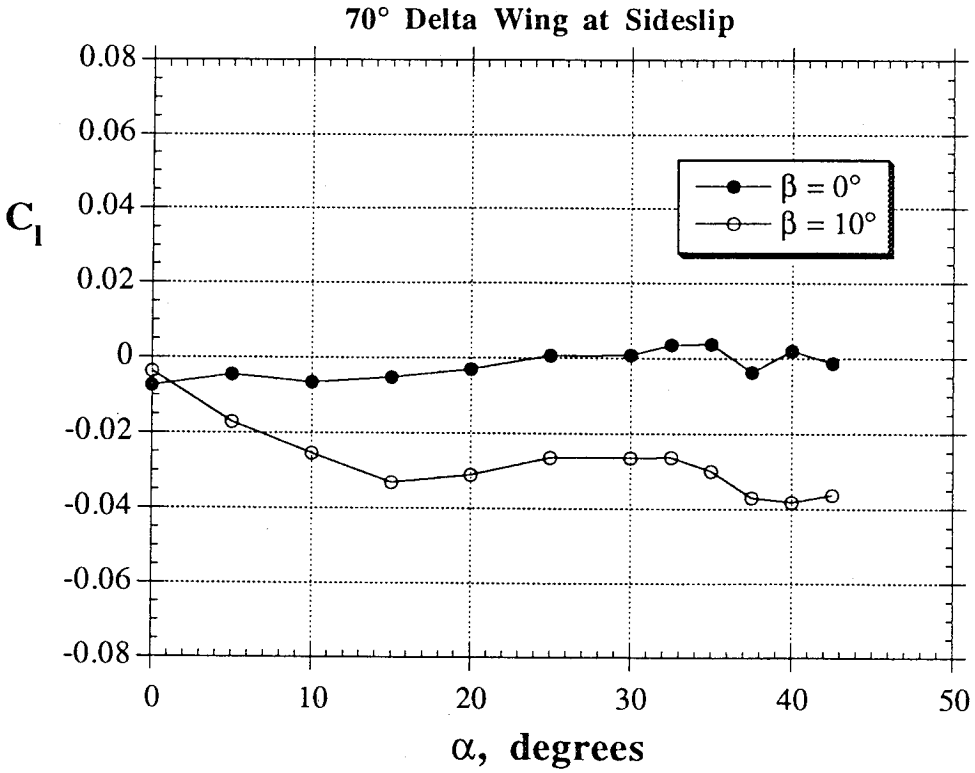

Figure 30 - Concluded

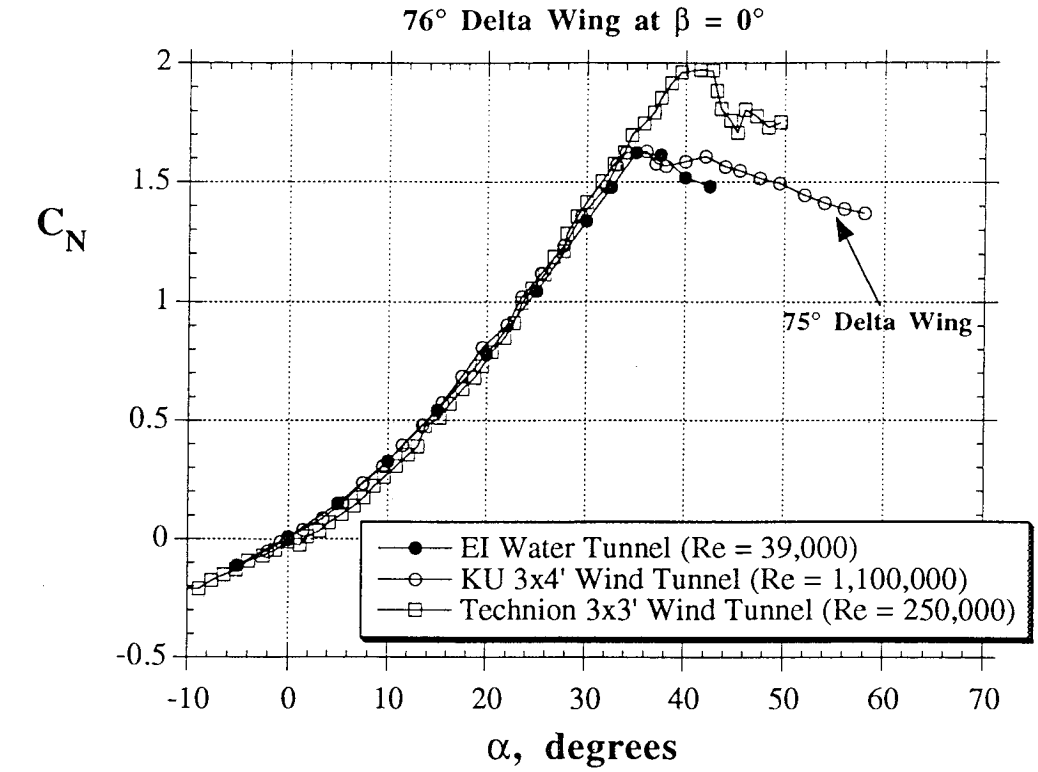

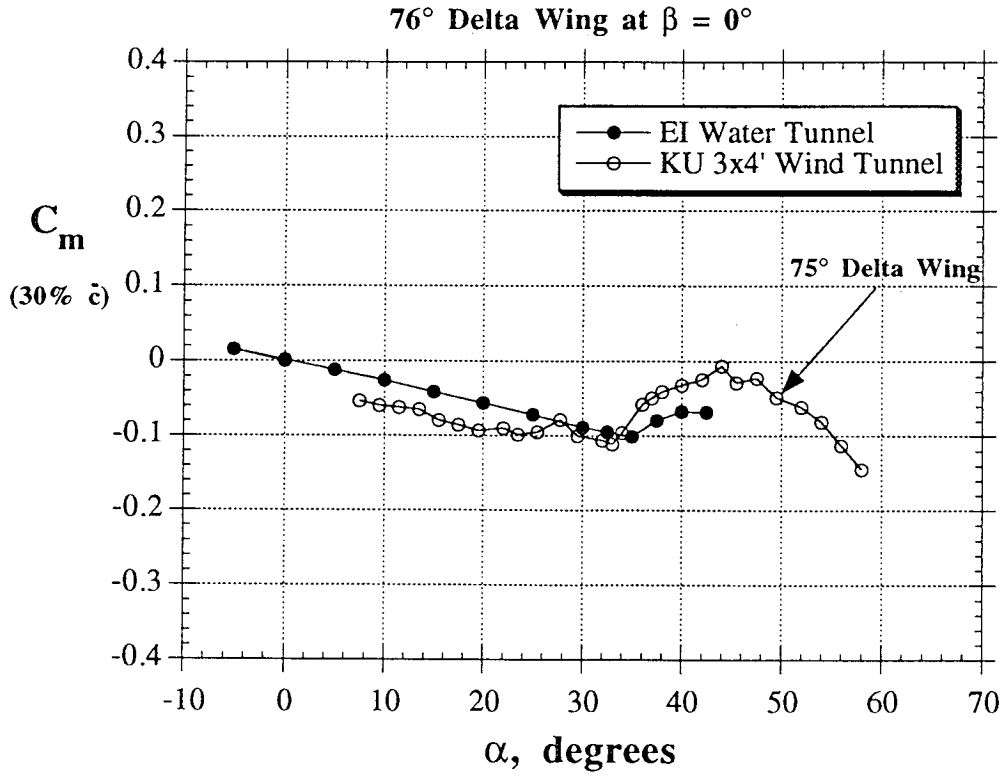

Figure 31 - Longitudinal Characteristics of the 76° Delta Wing at β = 0° (Comparison with Refs. 8 and 12)

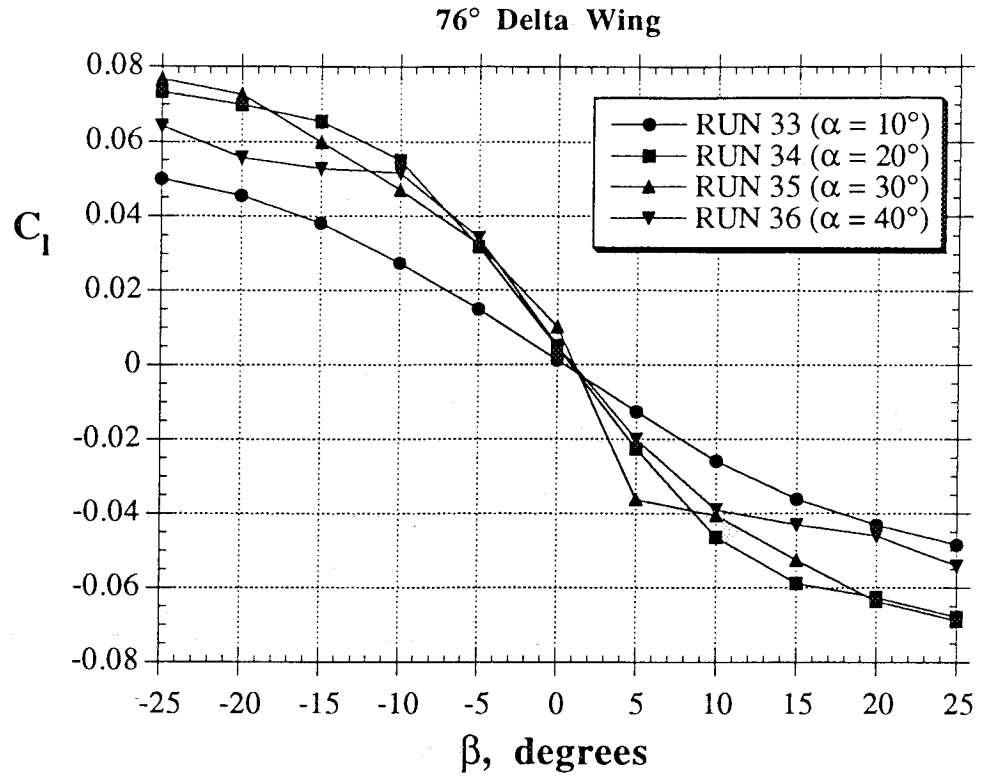

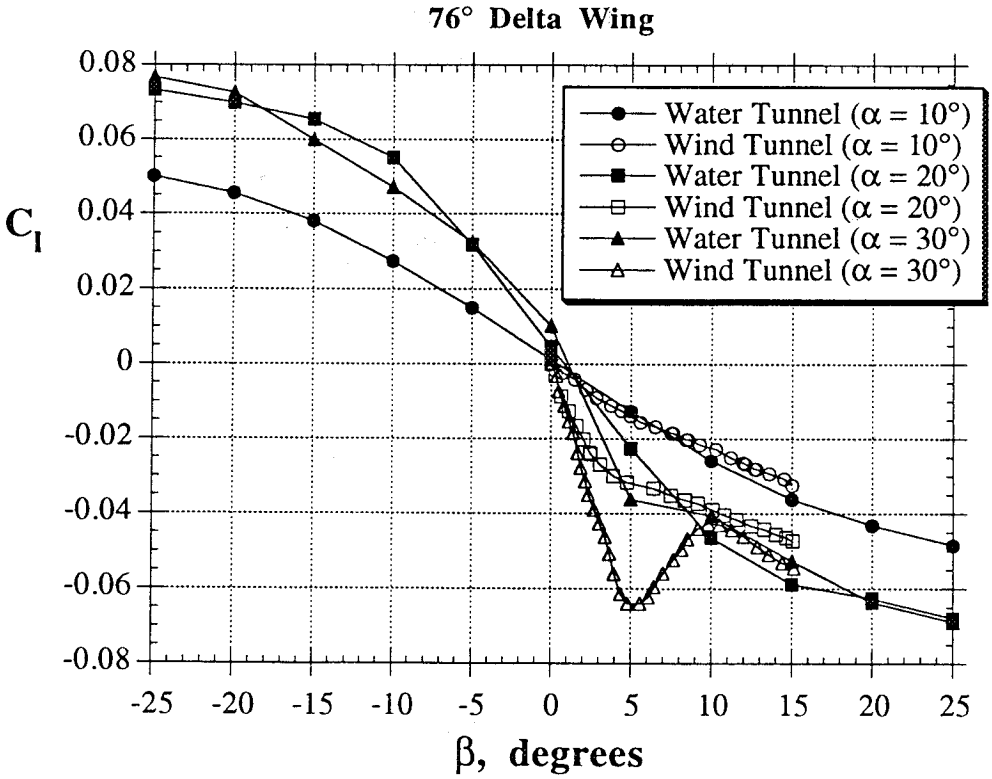

Figure 32 - Effect of Sideslip Variations on the Rolling Moment of the 76° Delta Wing at Different Angles of Attack (Comparison with Ref. 12)

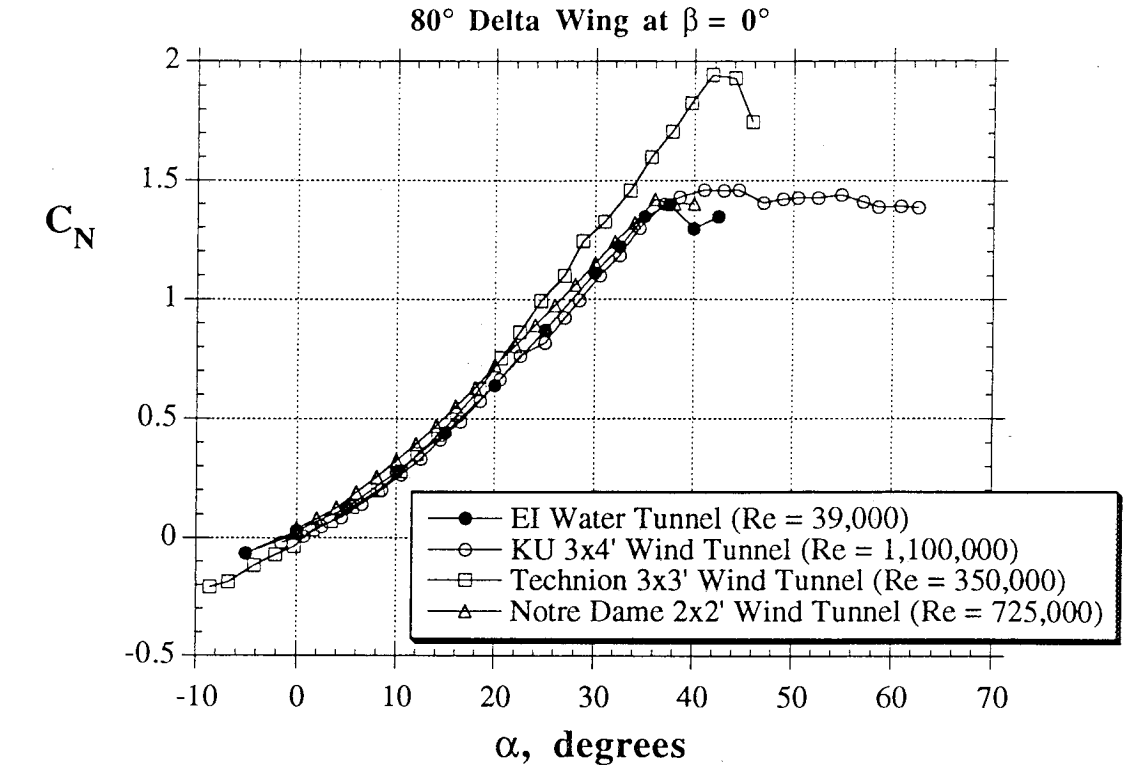

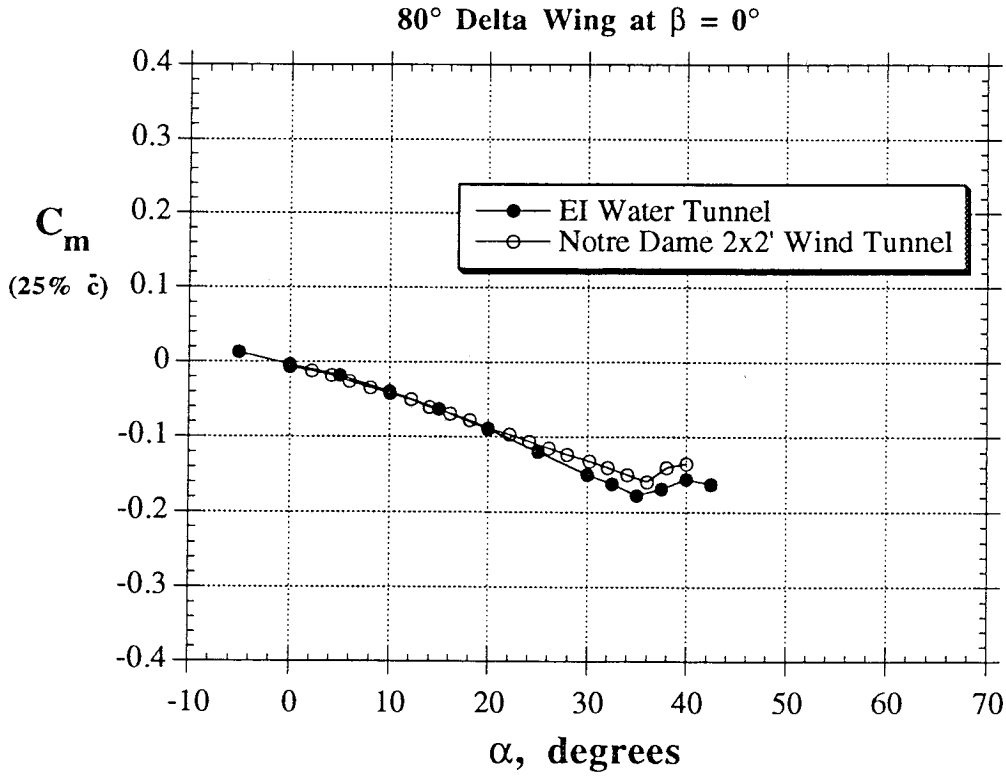

Figure 33 - Longitudinal Characteristics of the 80° Delta Wing at β = 0° (Comparison with Refs. 8, 12, 13)

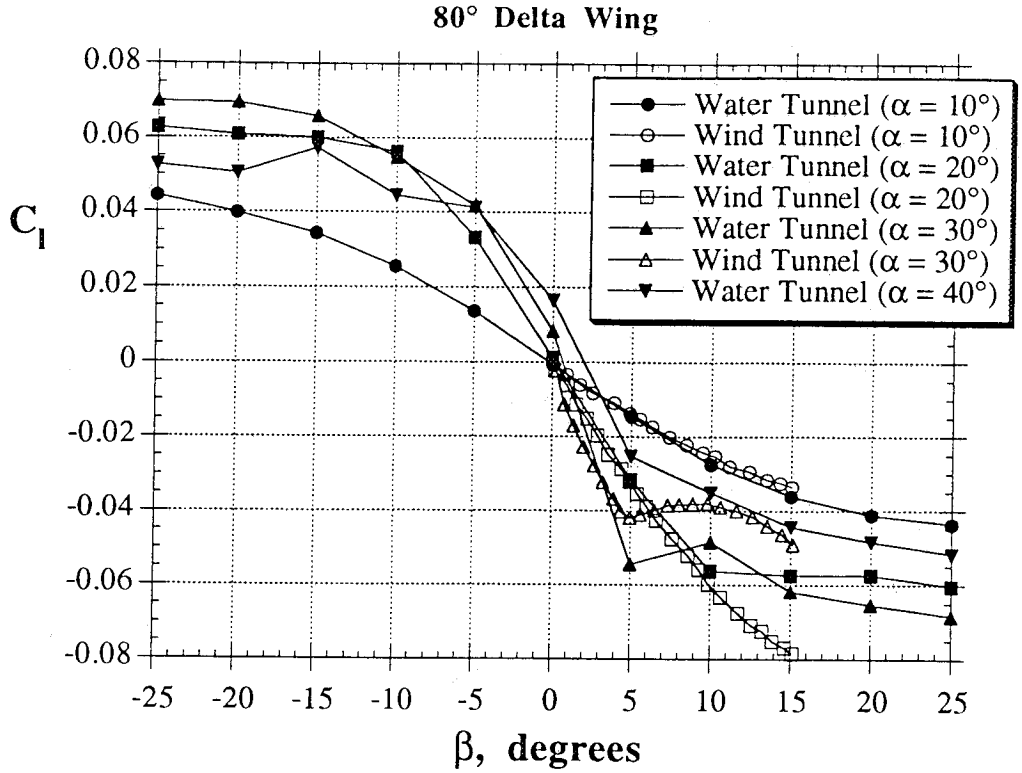

Figure 34 - Effect of Sideslip Variations on the Rolling Moment of the 80° Delta Wing at Different Angles of Attack (Comparison with Ref. 12)

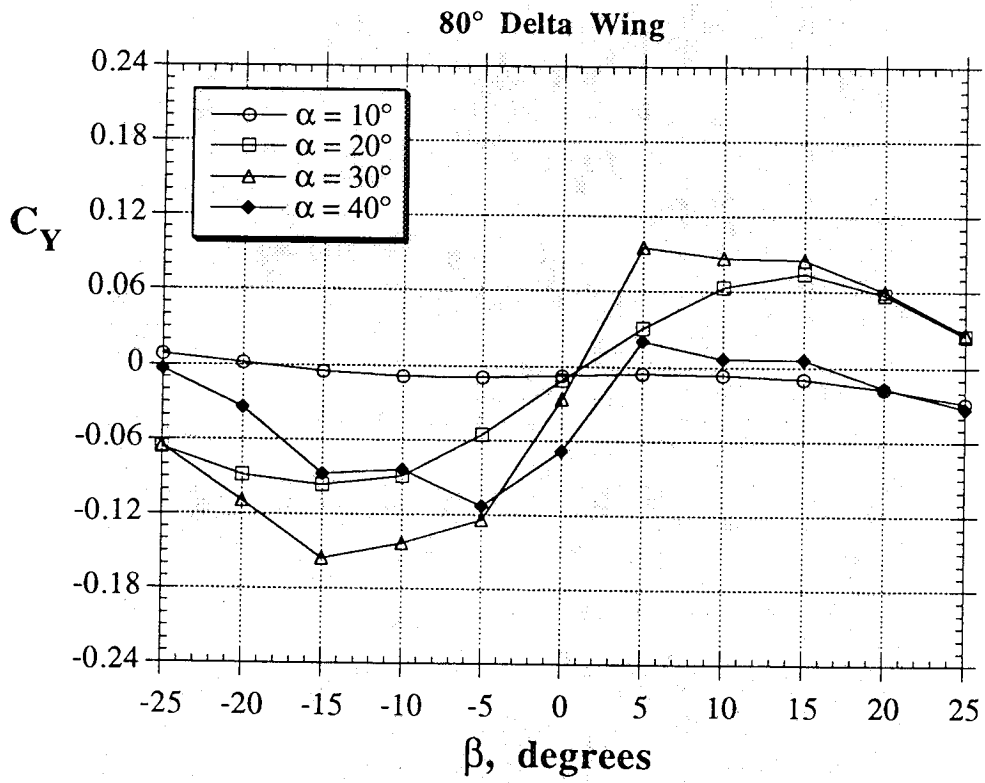

Figure 35 - Effect of Sideslip Variations on the Directional Characteristics of the 80° Delta Wing at Different Angles of Attack

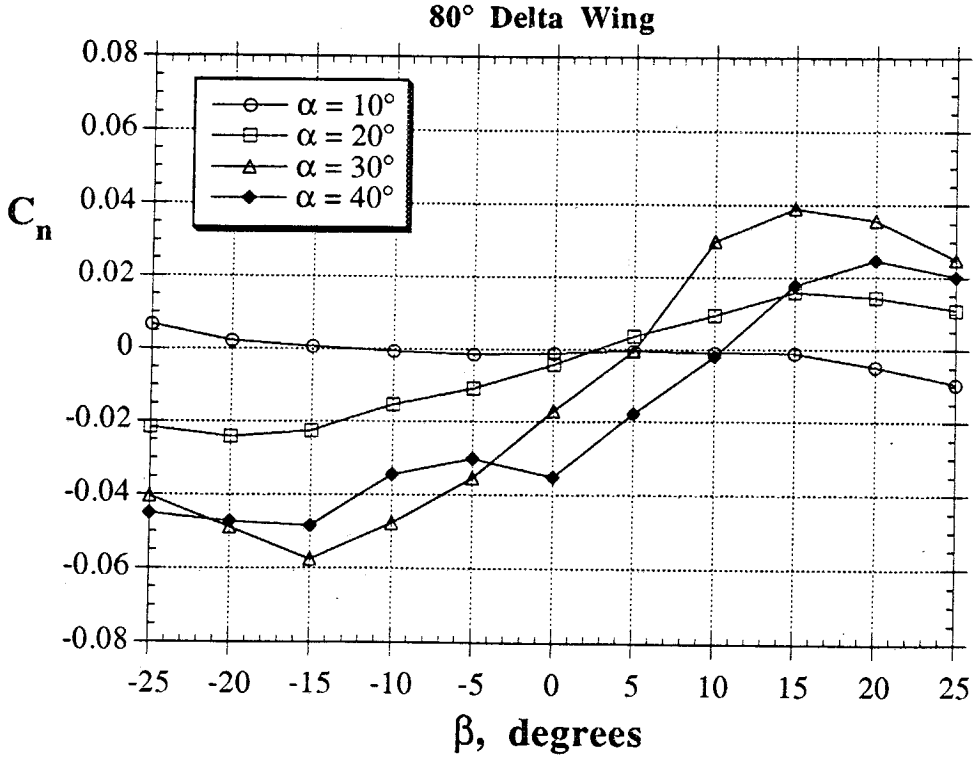

Figure 35 - Concluded

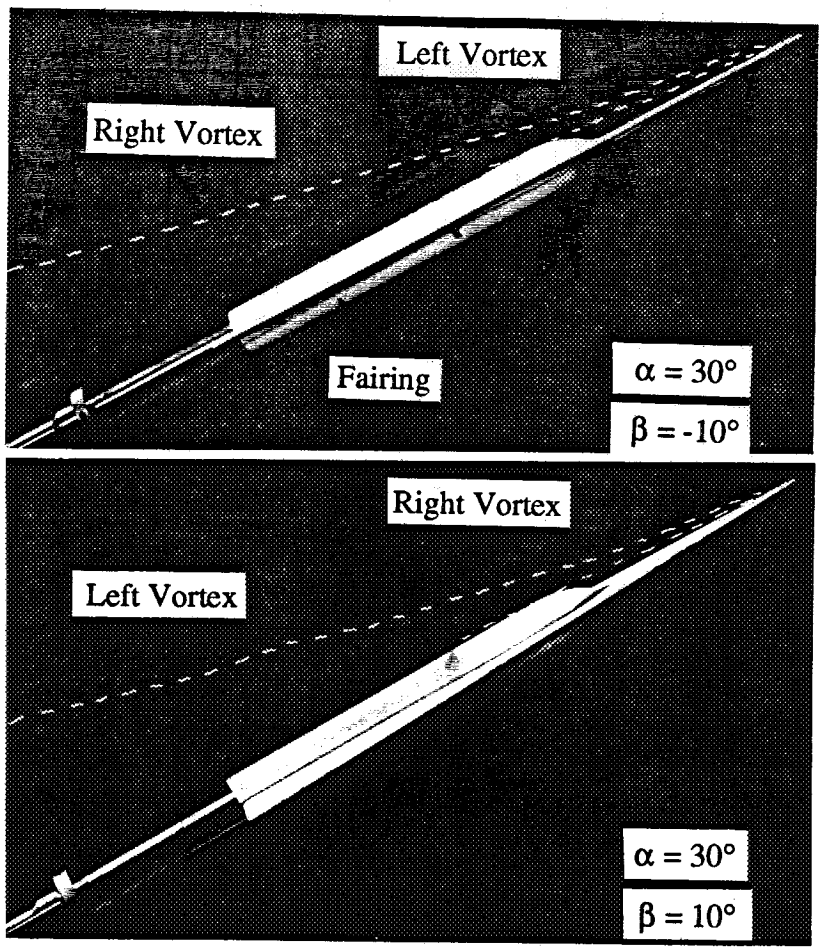

Figure 36 - Flow Visualization on the 80° Delta Wing at $\alpha = 30°$ and $\beta = +/-10°$

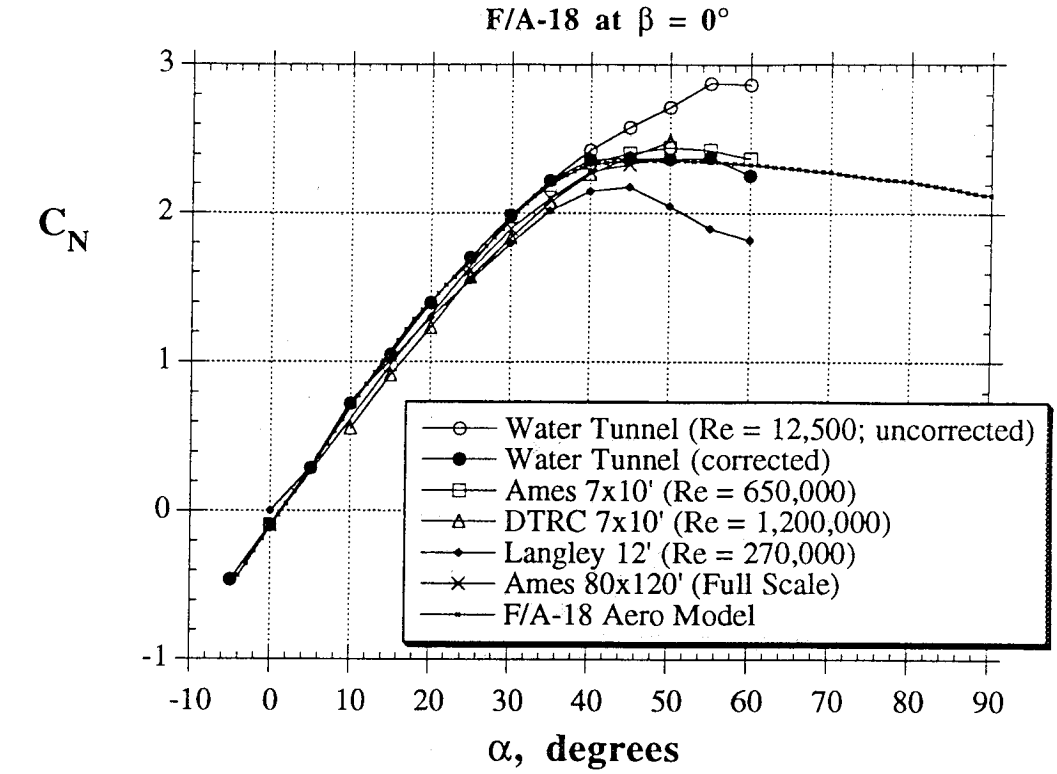

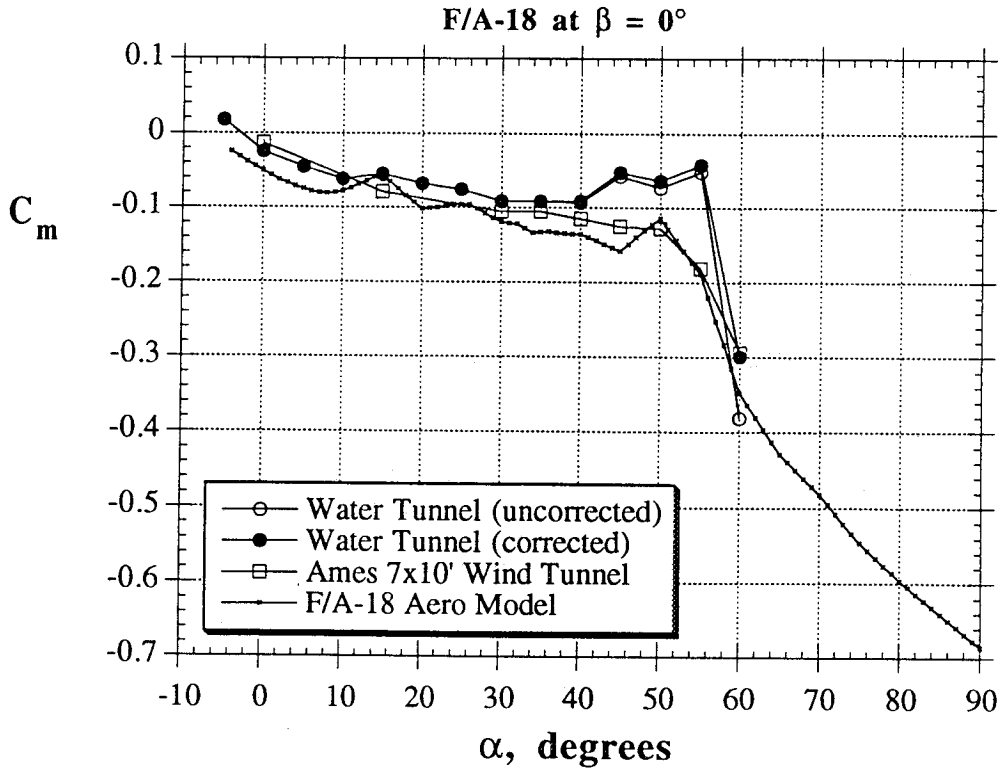

Figure 37 - Force/Moment Measurements on the F/A-18 Model at β = 0° (Comparison with Refs. 16, 17, 18, 19)

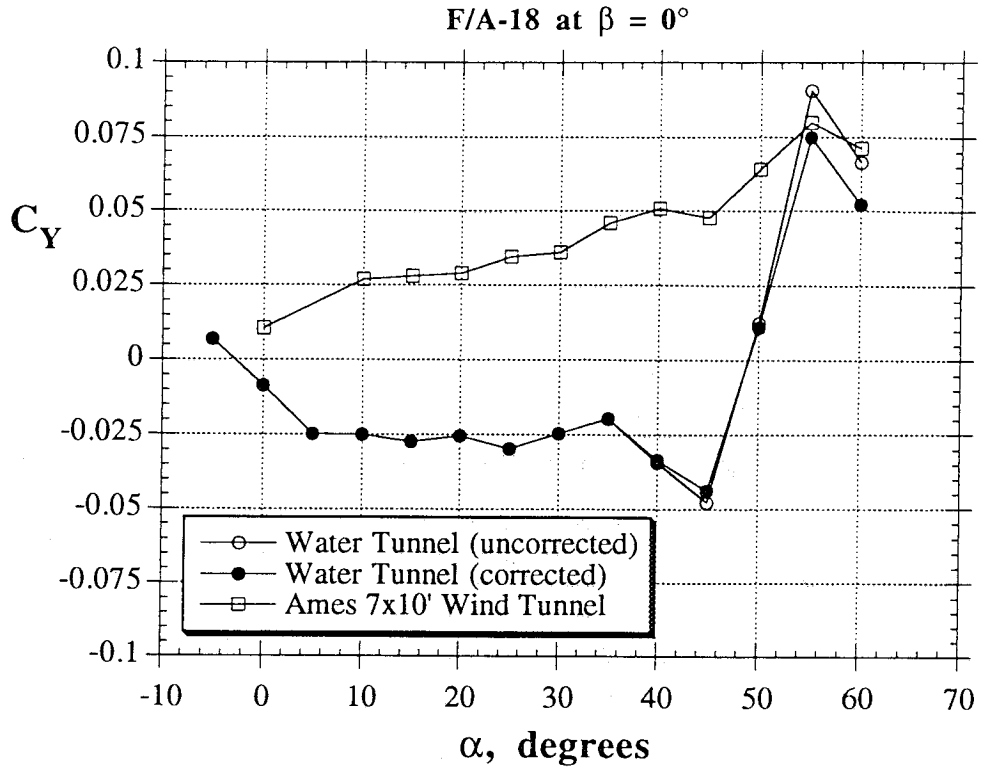

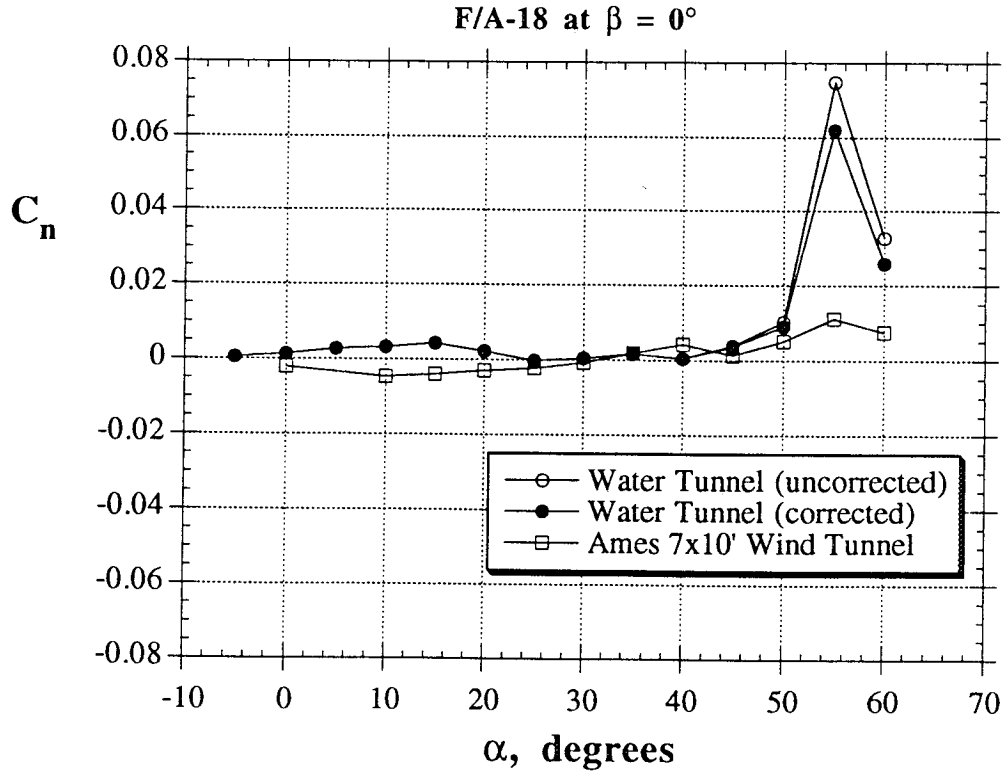

Figure 37 - Continued

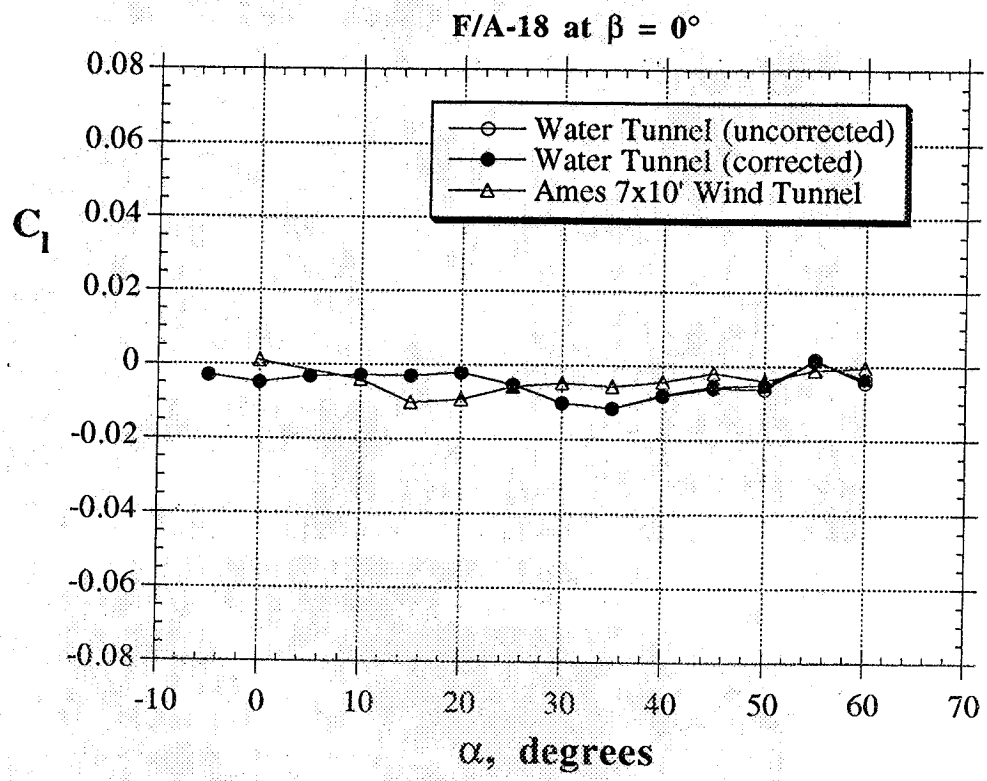

Figure 37 - Concluded

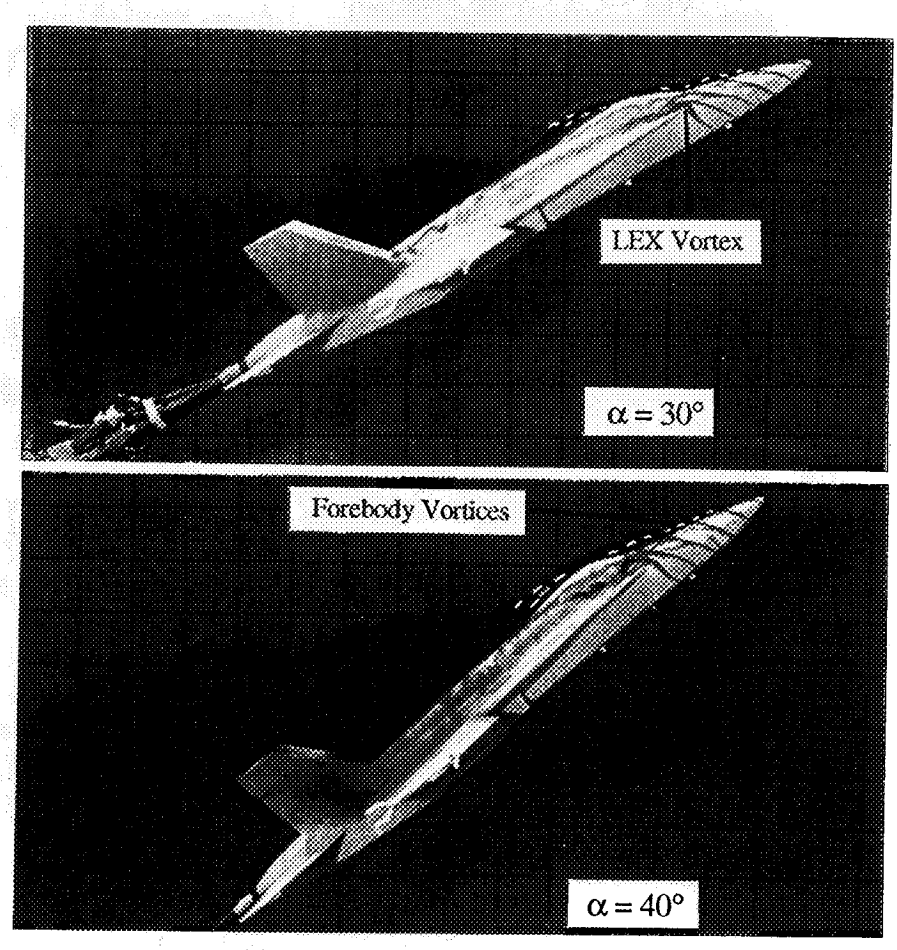

Figure 38 - Flow Visualization on the F/A-18 Model at β = 0°

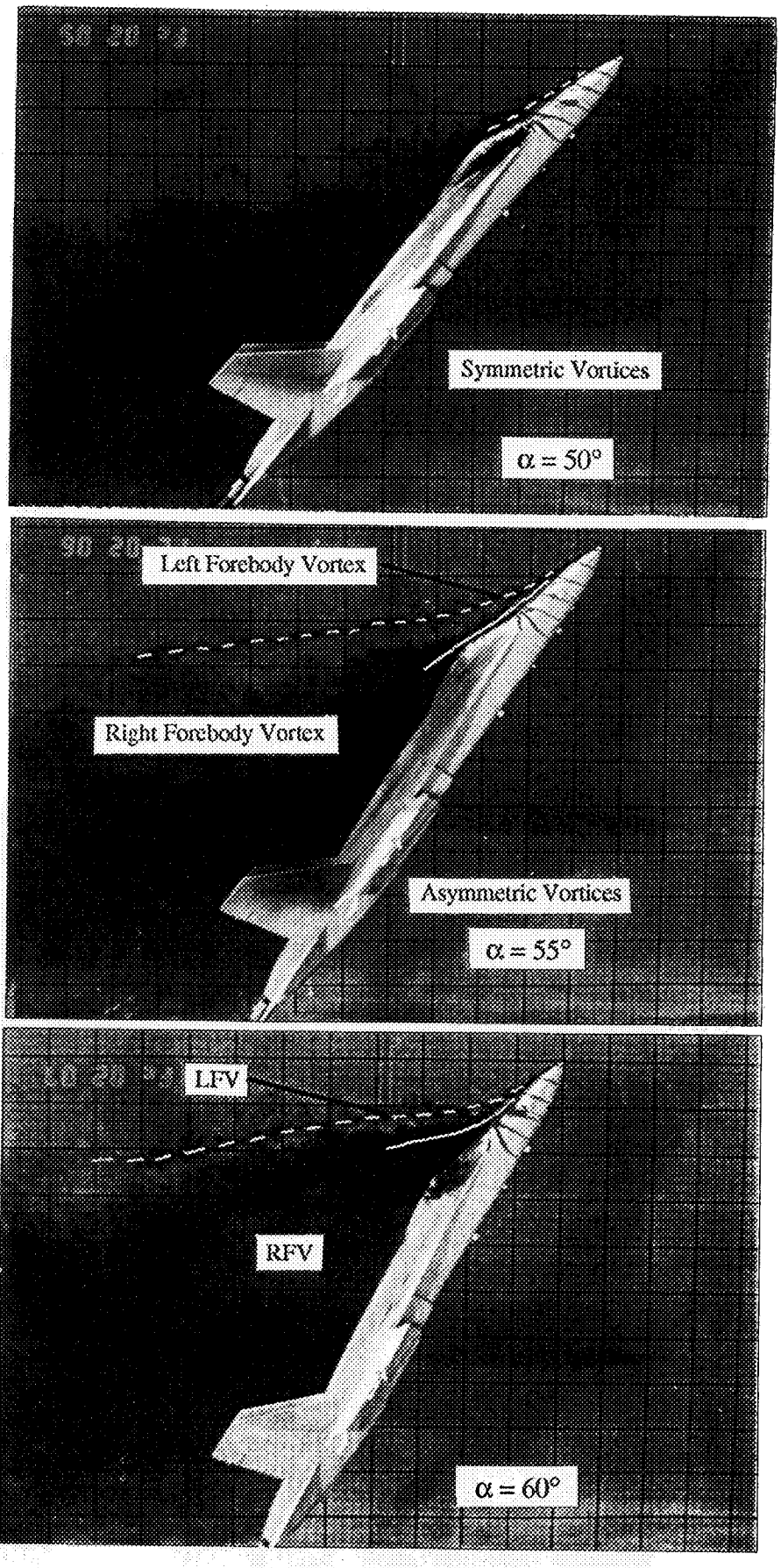

Figure 38 - Concluded

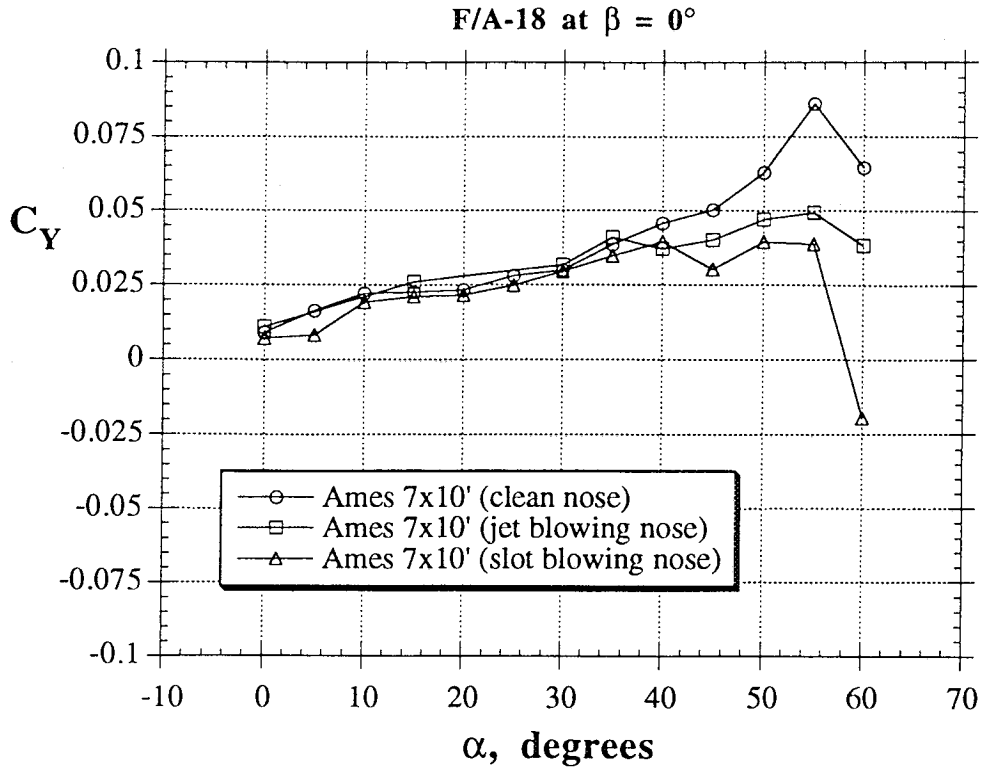

Figure 39 - Side Force Variations on an F/A-18 Model With Different Forebodies (From Wind Tunnel Test Performed in Ref. 16)

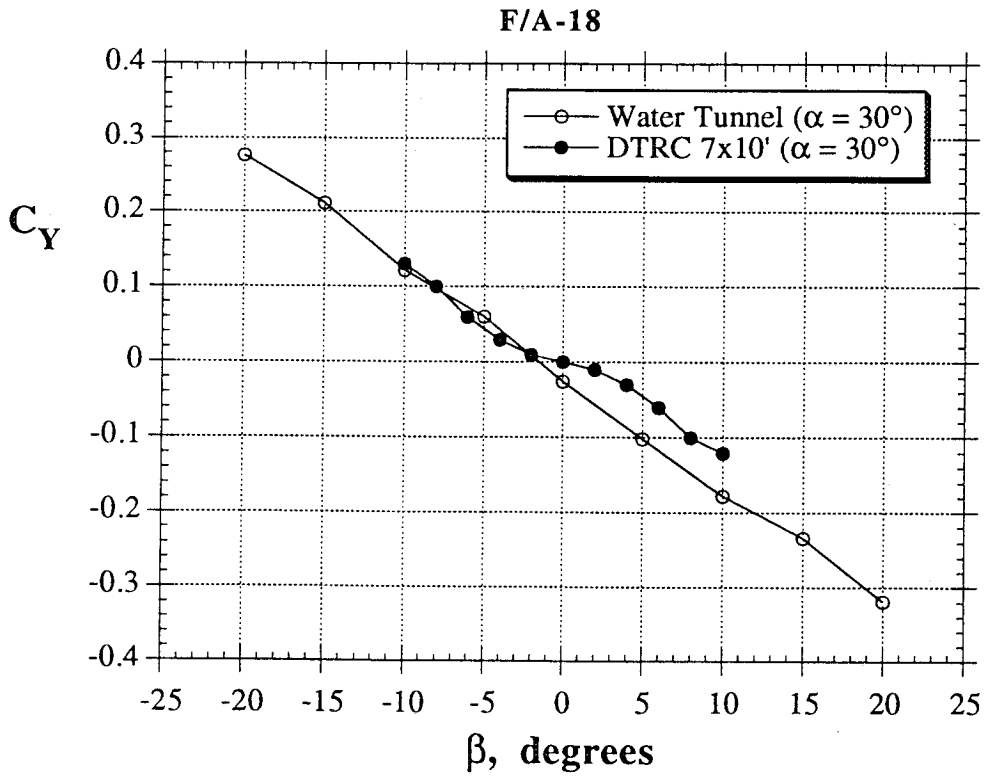

Figure 40 - Effect of Sideslip Variations on the Lateral-Directional Characteristics of the F/A-18 Model at $\alpha = 30°$ (Comparison with Ref. 18)

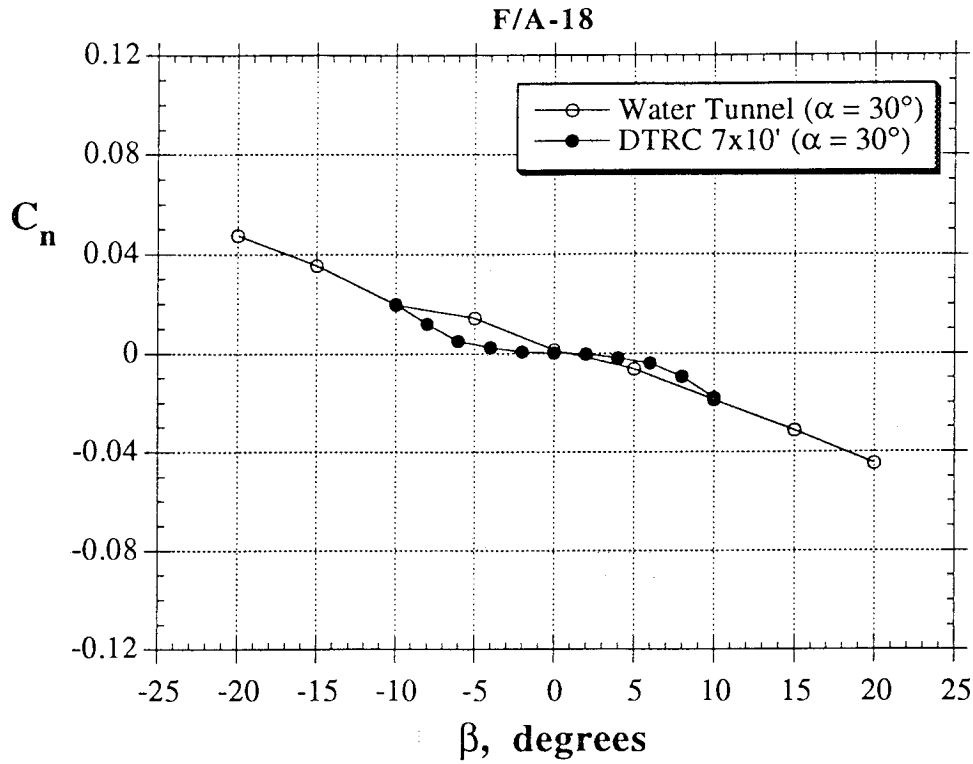

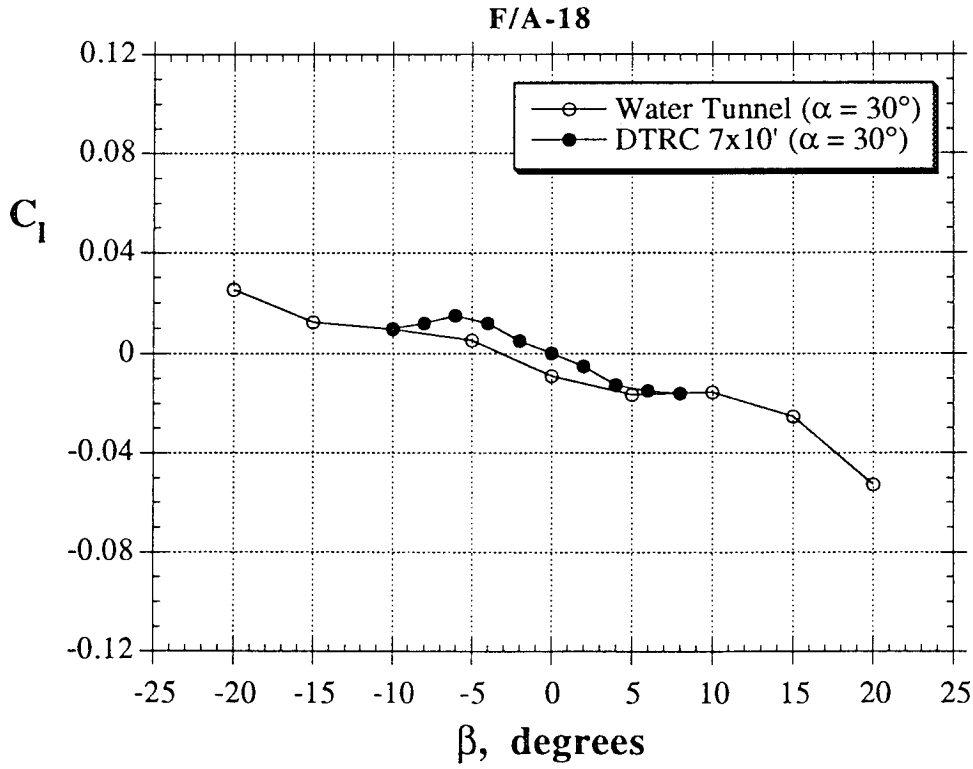

Figure 40 - Concluded

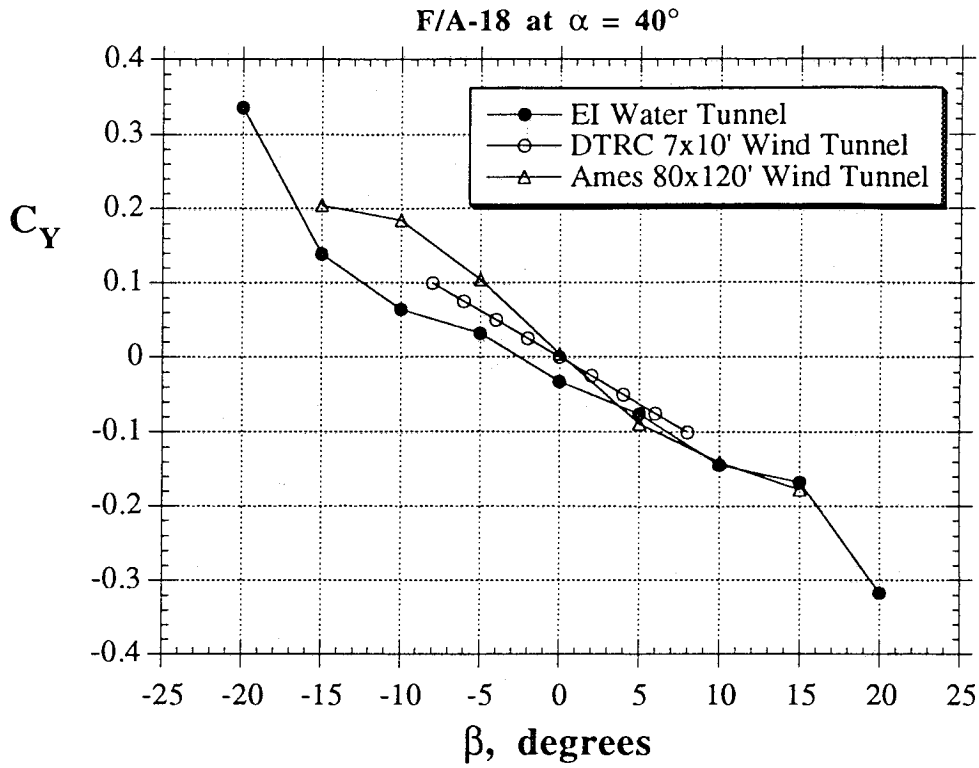

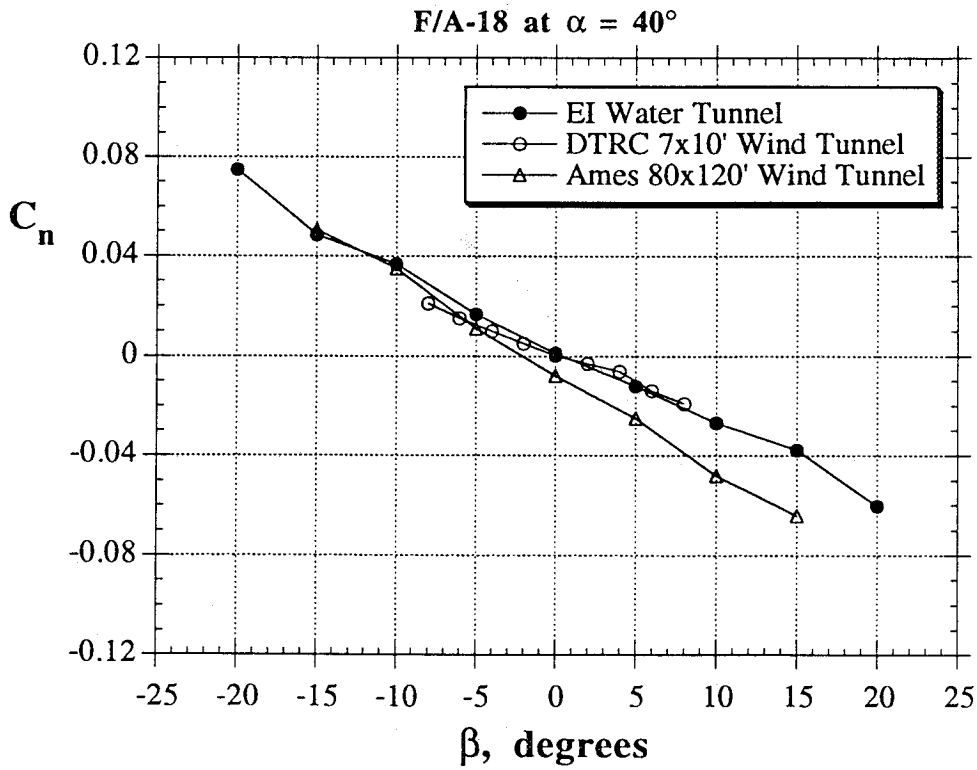

Figure 41 - Effect of Sideslip Variations on the Lateral-Directional Characteristics of the F/A-18 Model at $\alpha = 40°$ (Comparison with Refs. 17, 18)

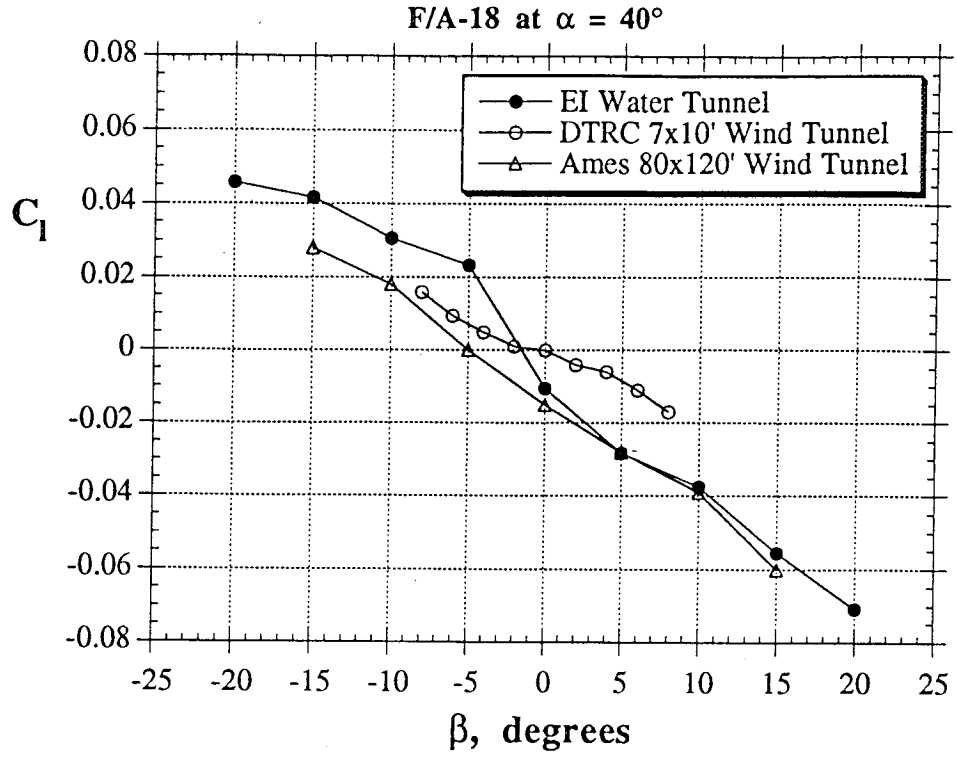

Figure 41 - Concluded

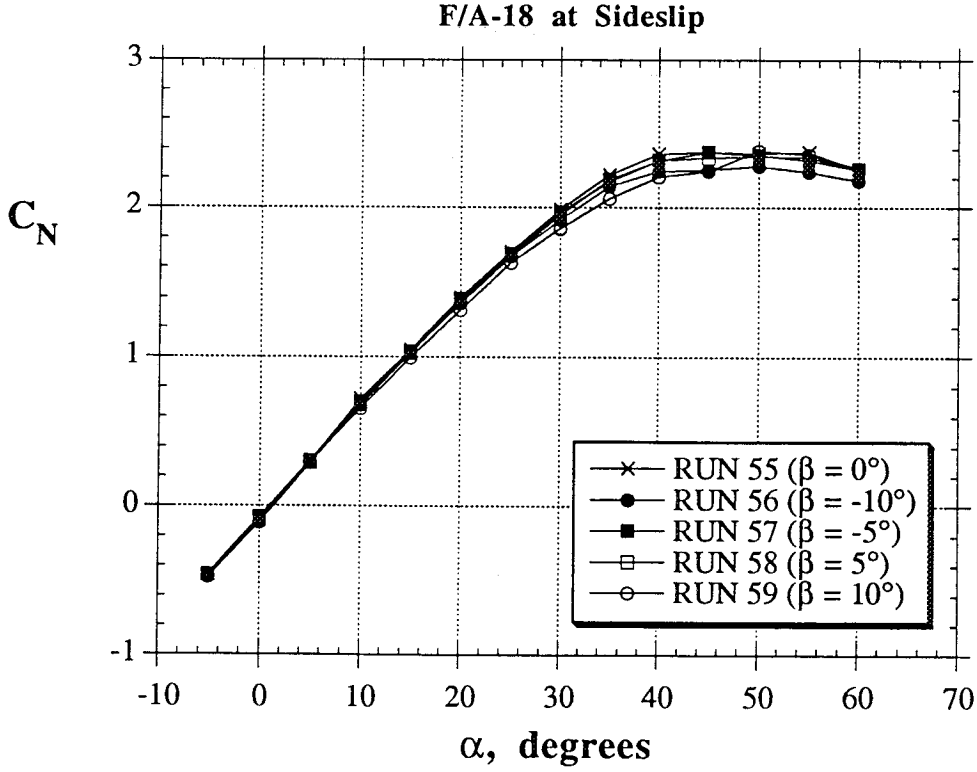

Figure 42 - Effect of Sideslip Angle on the Normal Force of the F/A-18

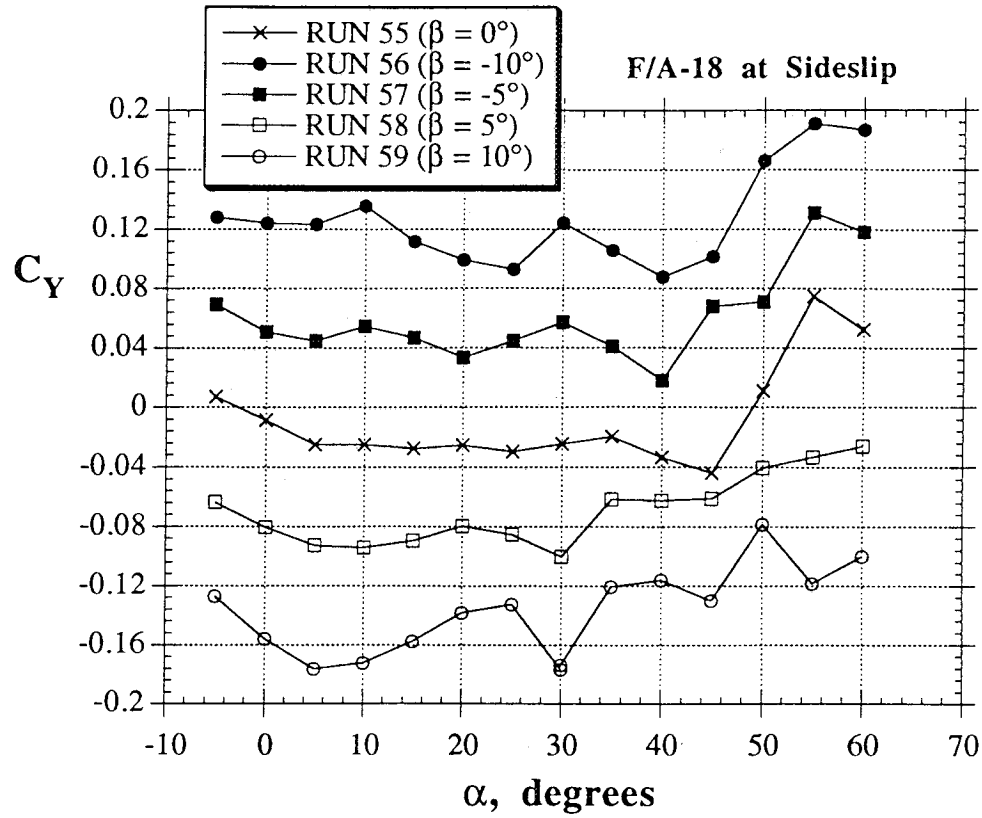

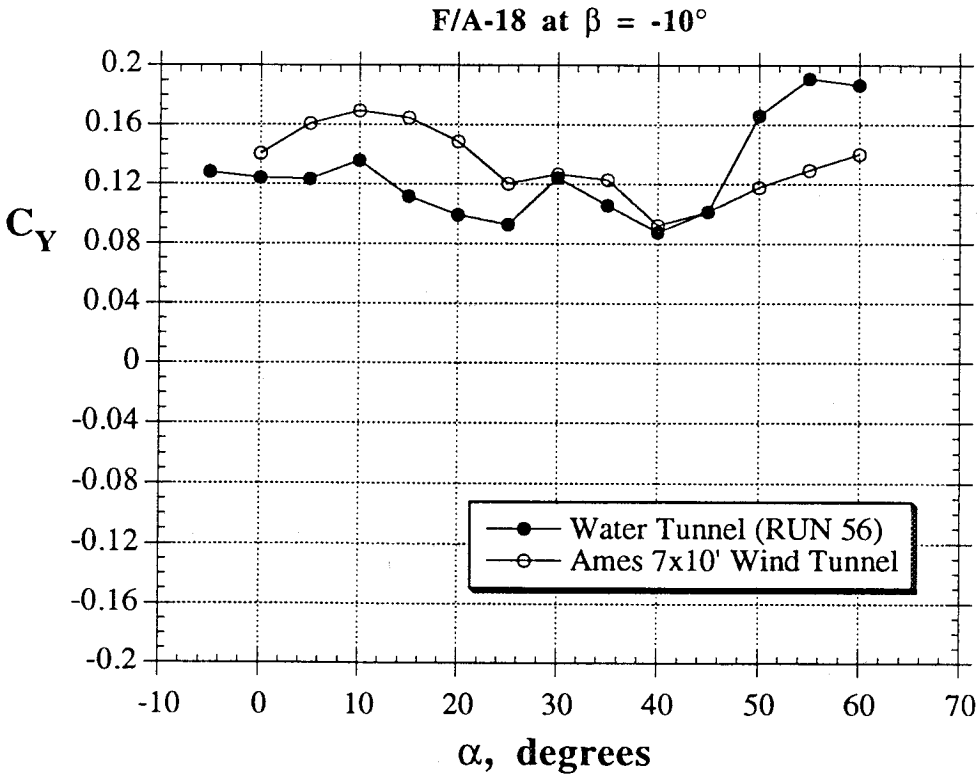

Figure 43 - Effect of Sideslip Angle on the Lateral-Directional Characteristics of the F/A-18 (Comparisons to Wind Tunnel Test, Ref. 16)

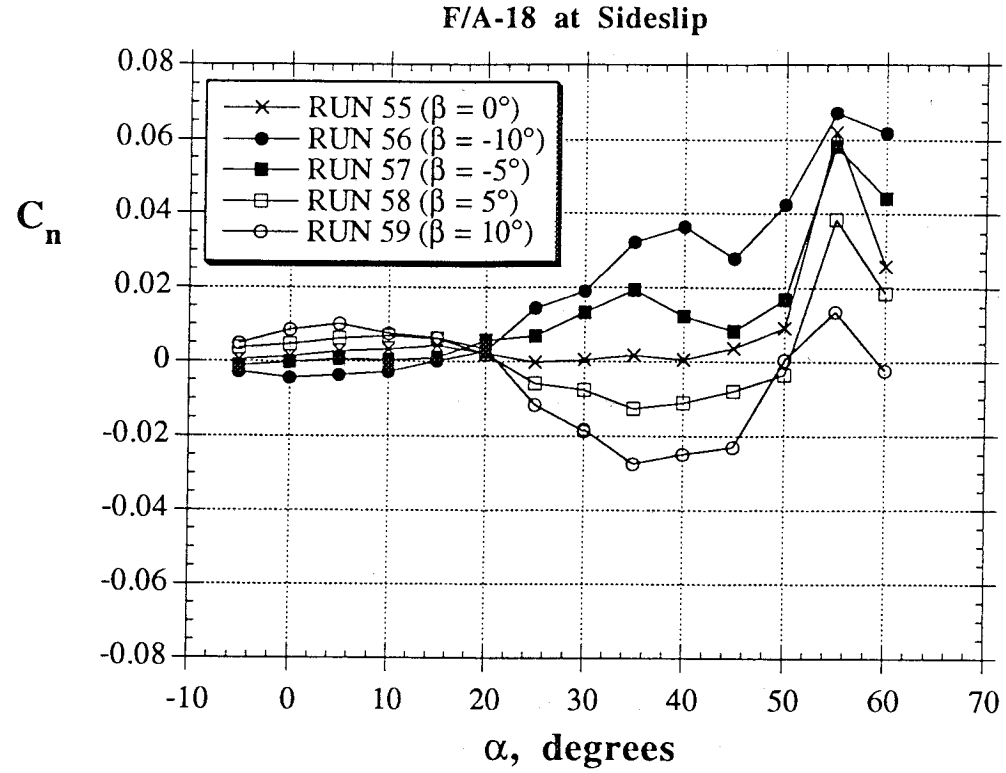

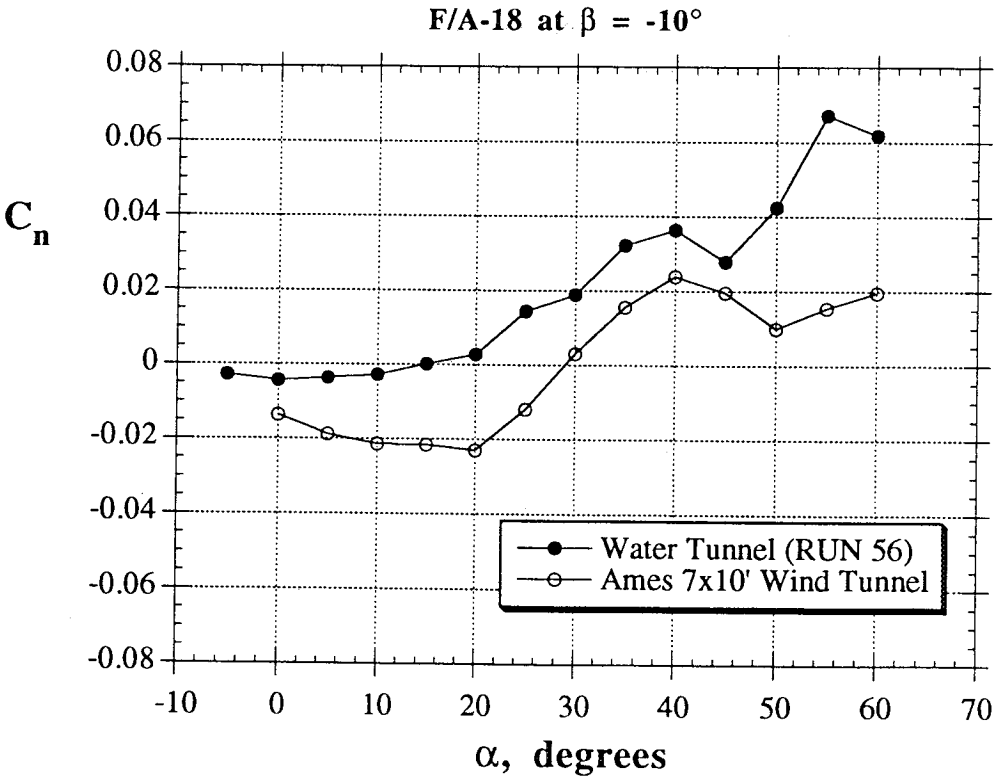

Figure 43 - Continued

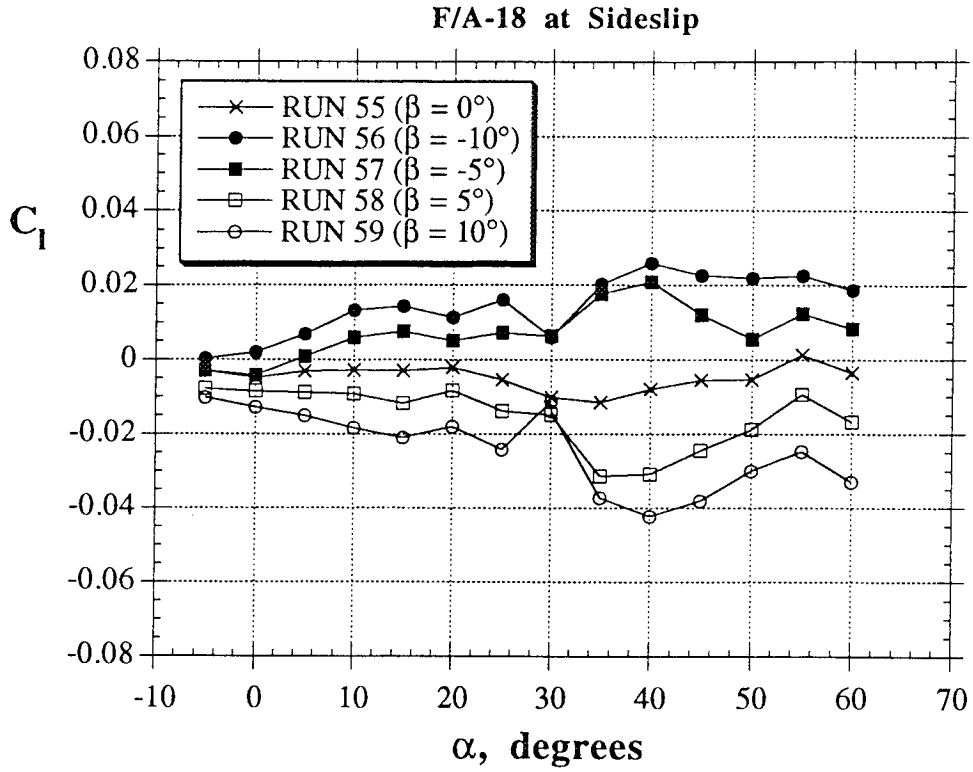

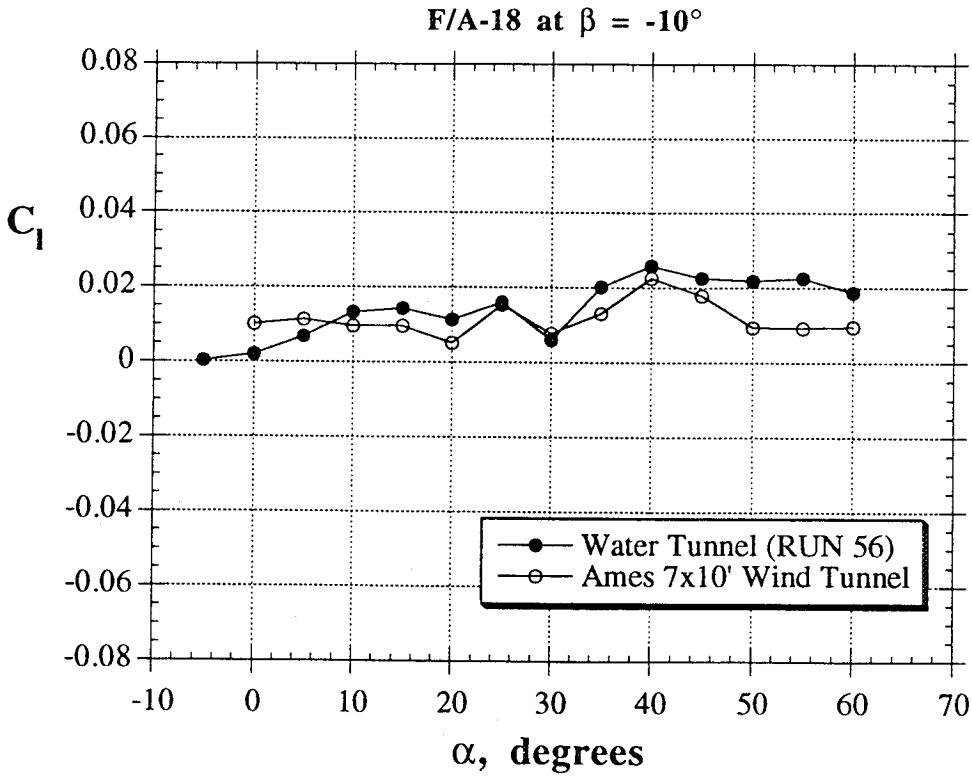

Figure 43 - Concluded

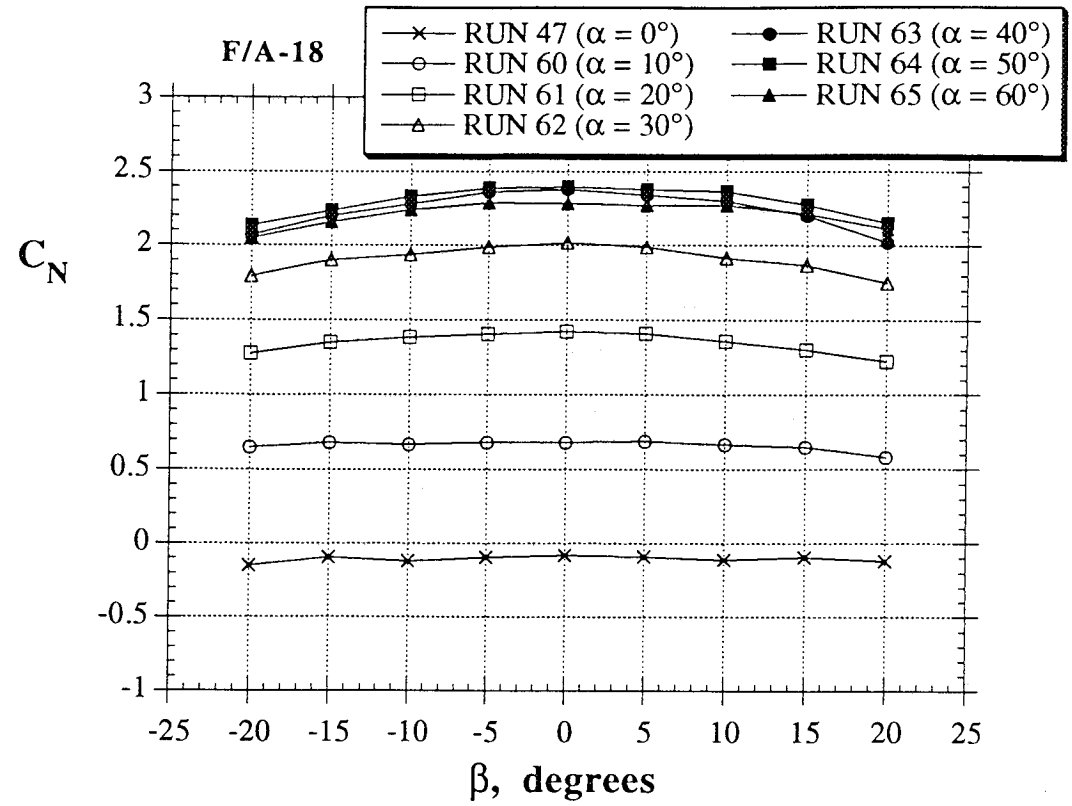

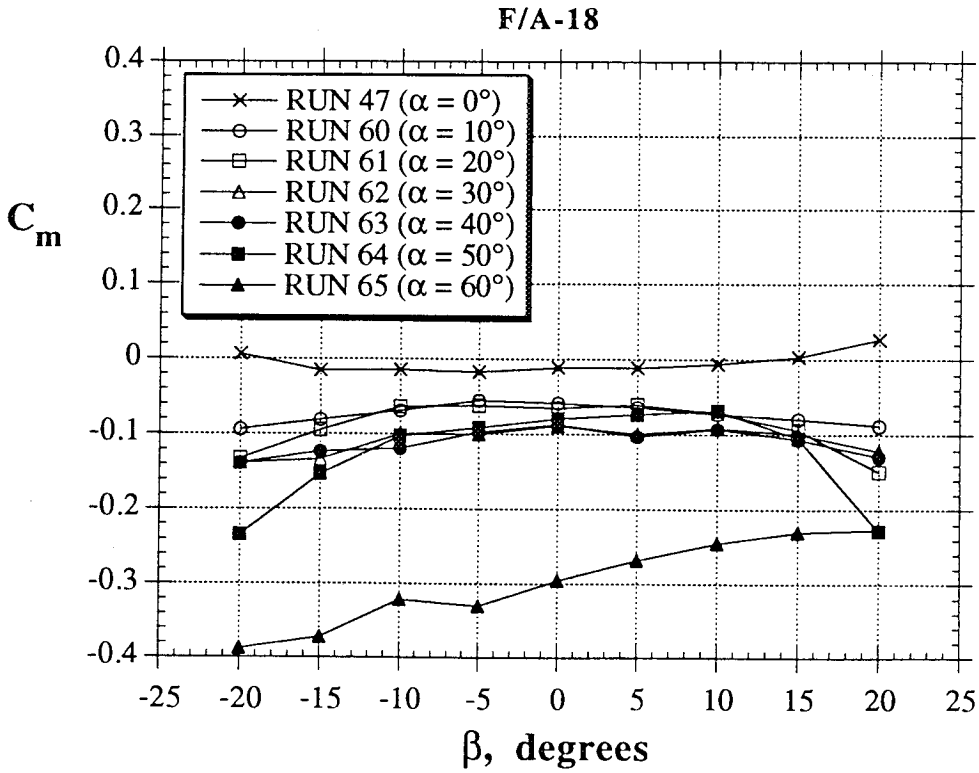

Figure 44 - Effect of Sideslip Variations at Constant Angles of Attack (F/A-18 Model)

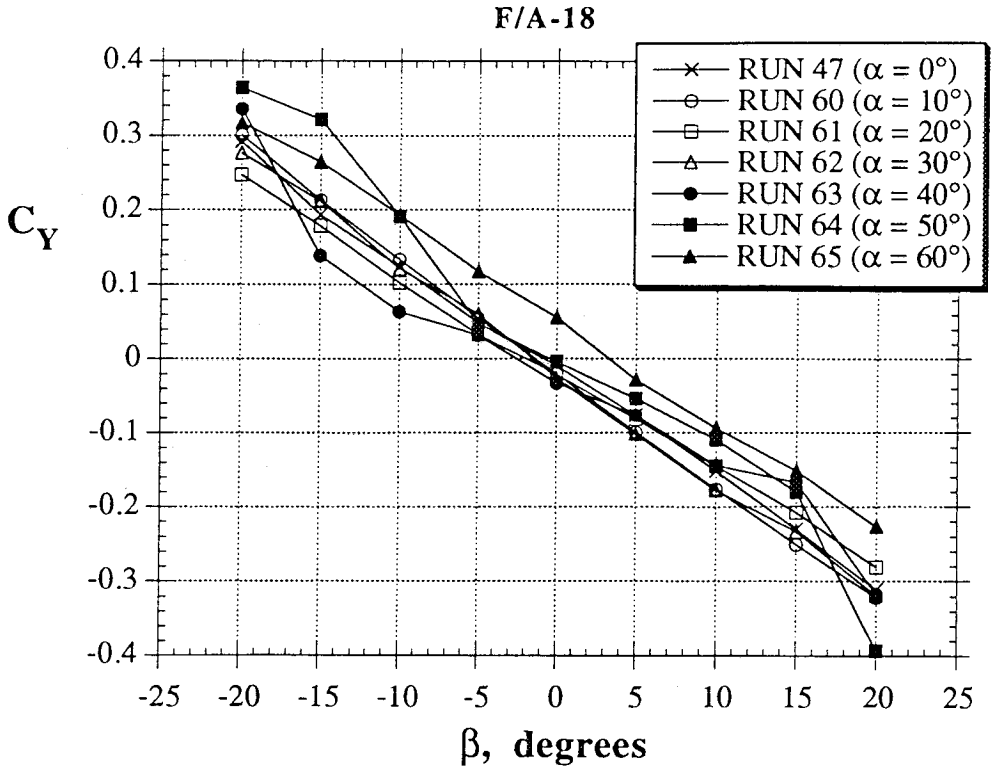

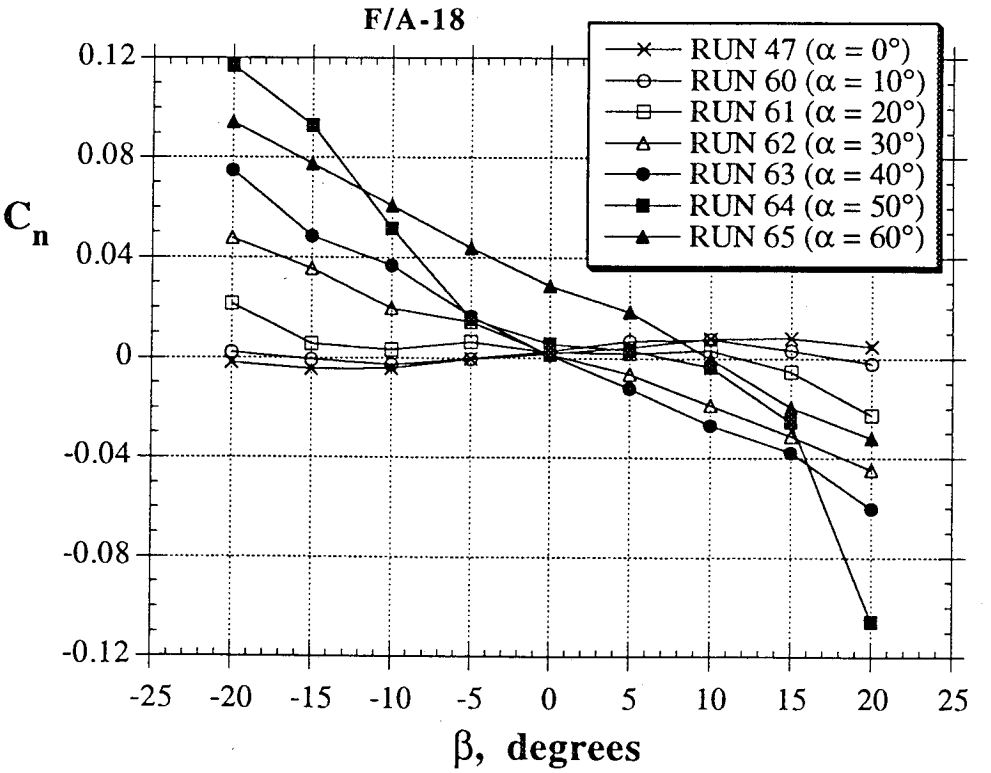

Figure 44 - Continued

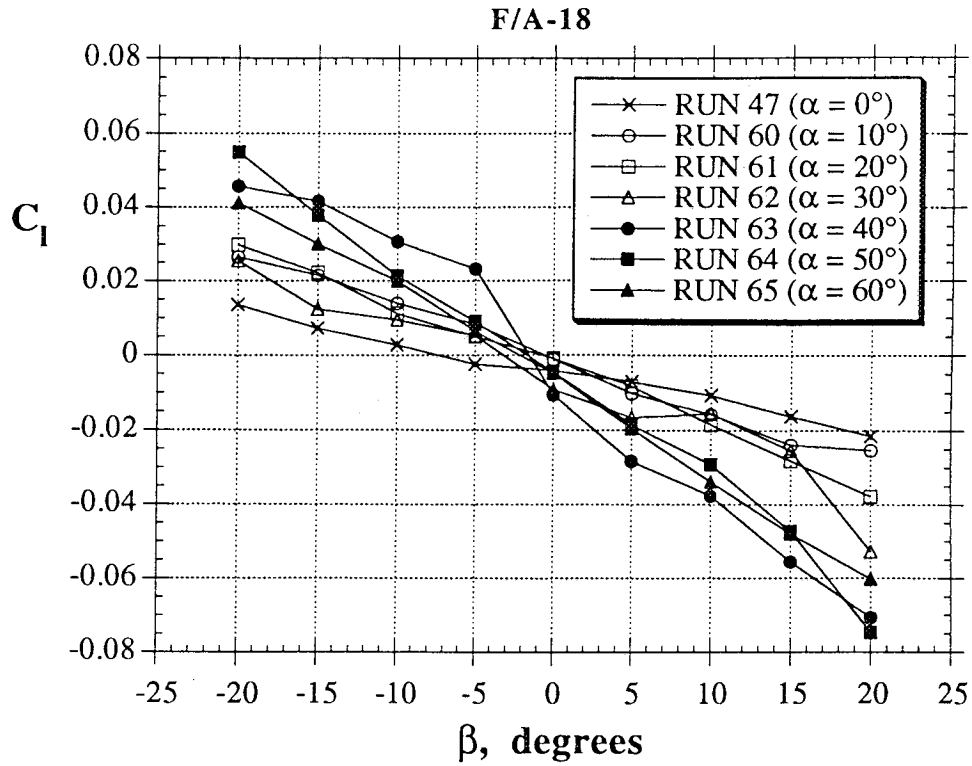

Figure 44 - Concluded

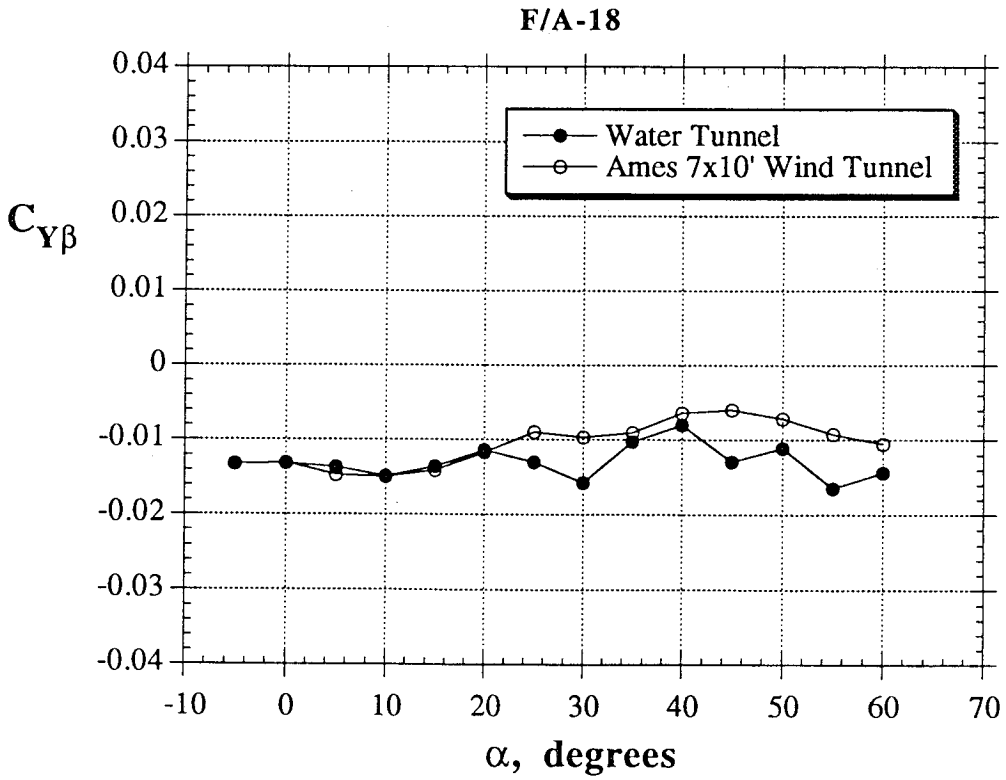

Figure 45 - Lateral-Directional Derivatives for the F/A-18 (Comparisons to Wind Tunnel Test, Ref. 16)

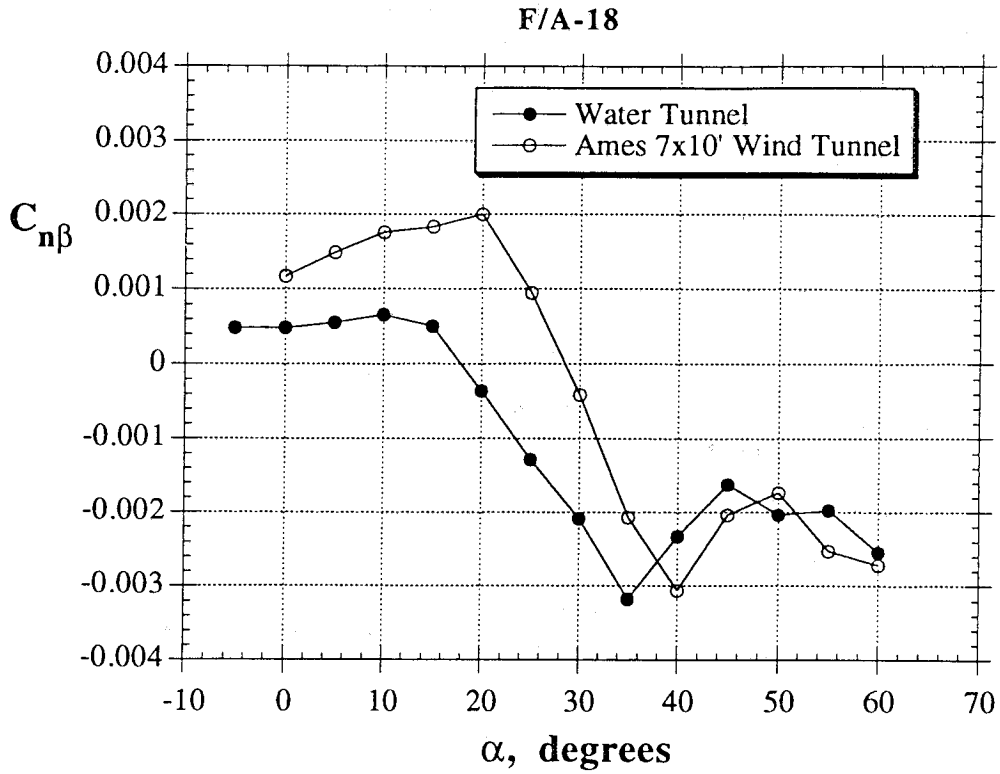

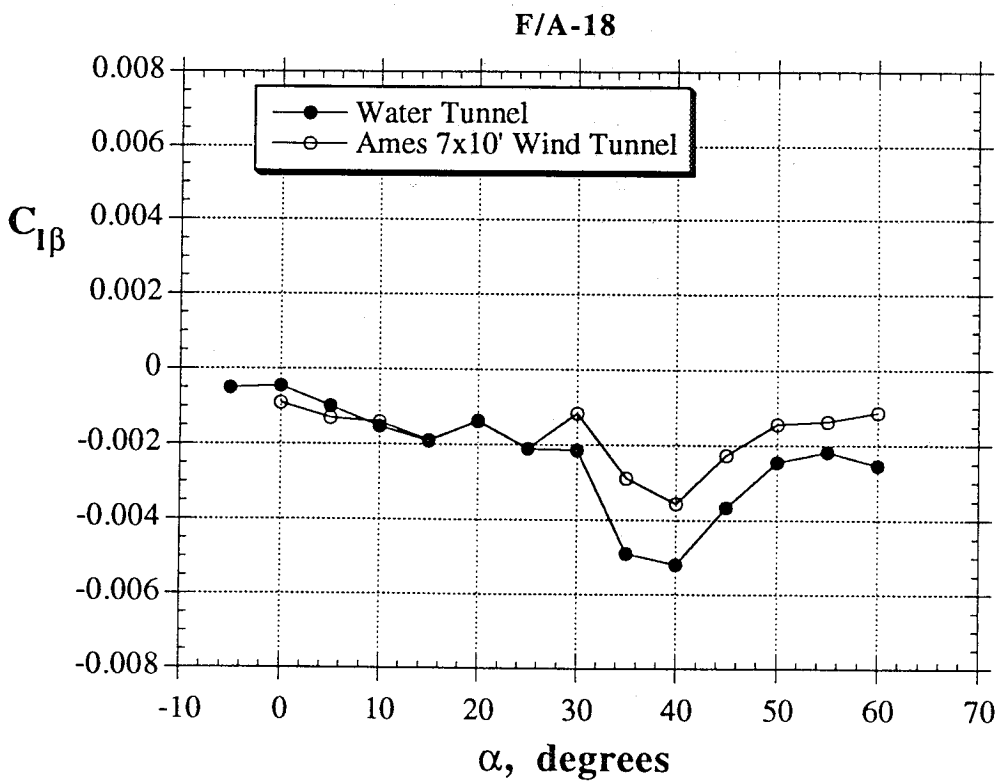

Figure 45 - Concluded

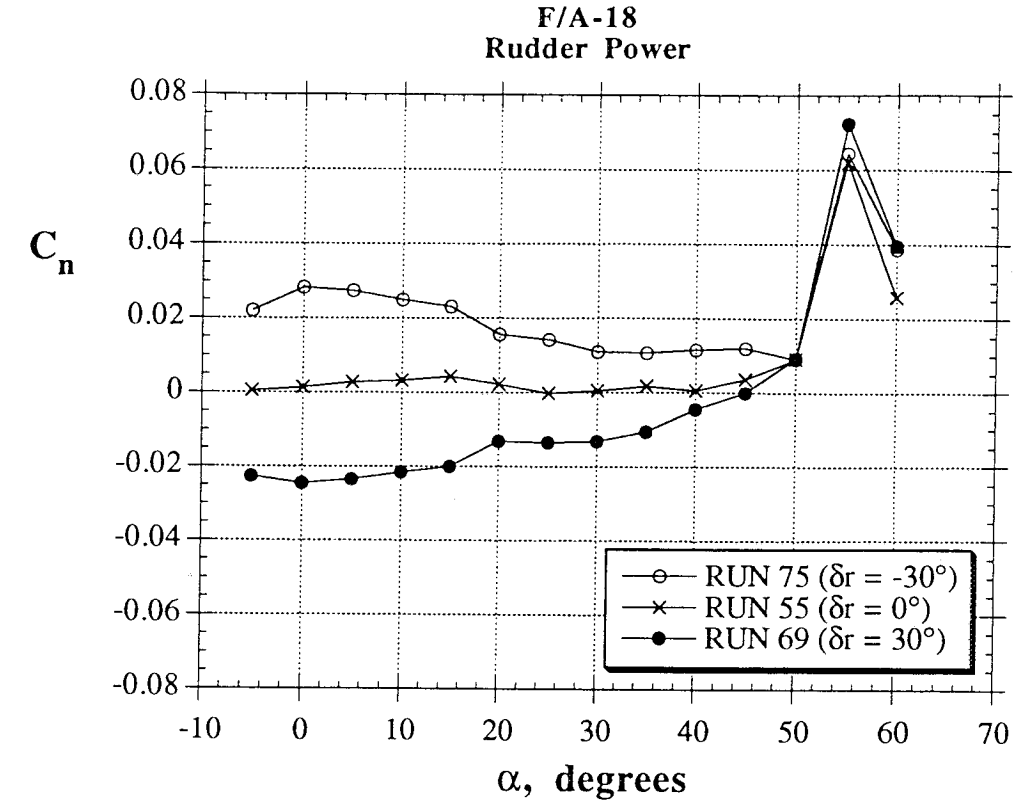

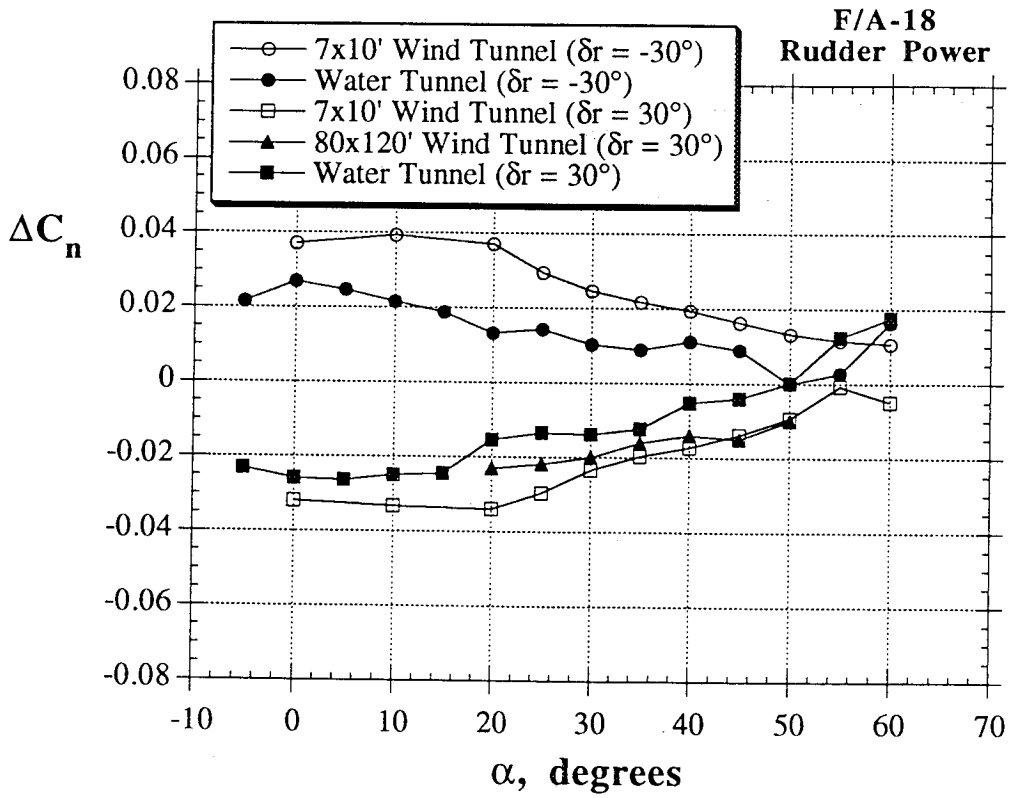

Figure 46 - Effect of Rudder Deflection on the F/A-18 Model
(Comparisons to Wind Tunnel Tests, Refs. 16 and 17)

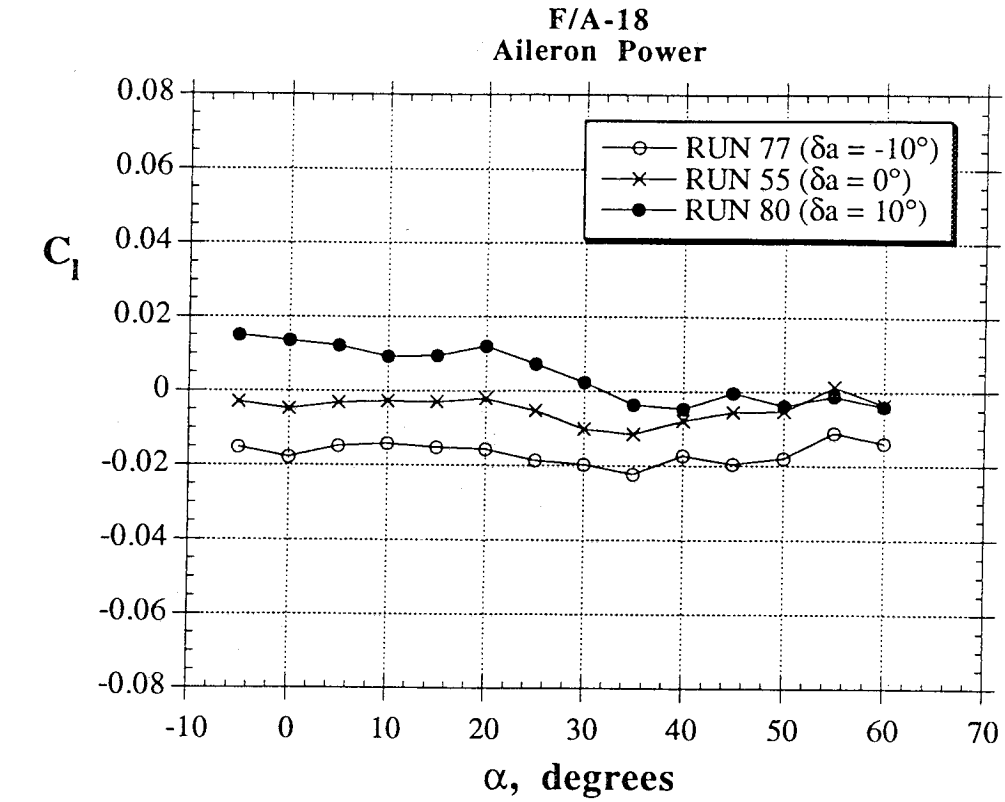

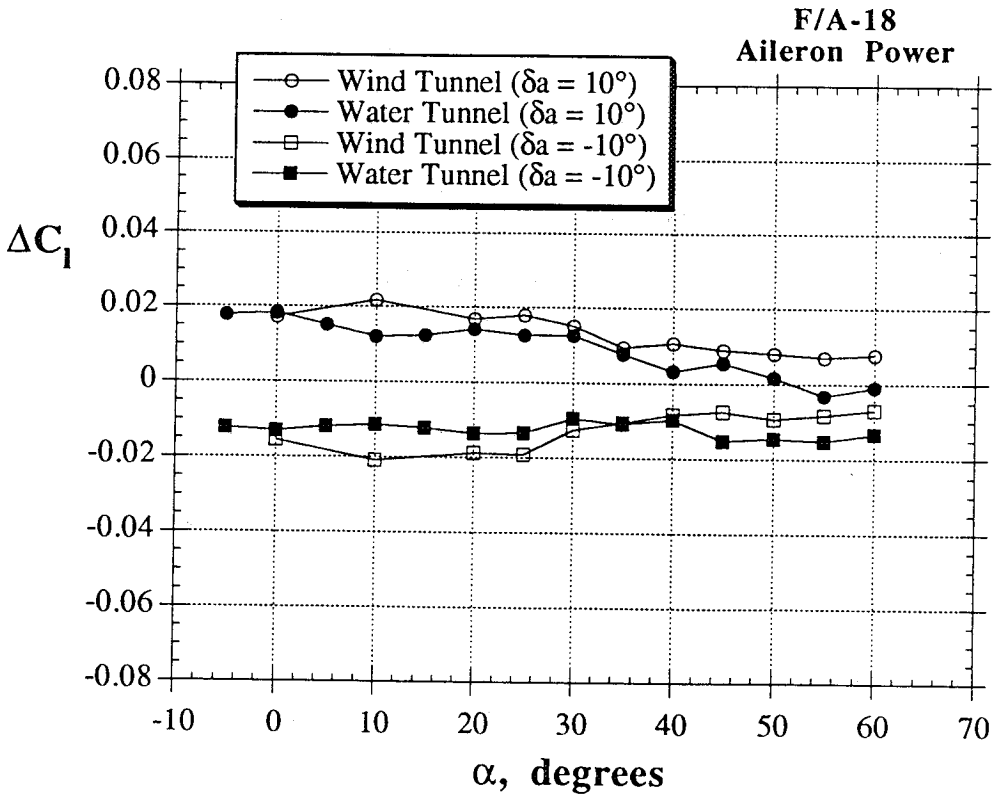

Figure 47 - Effect of Aileron Deflection on the F/A-18 Model (Comparisons to Wind Tunnel Tests, Ref. 16)

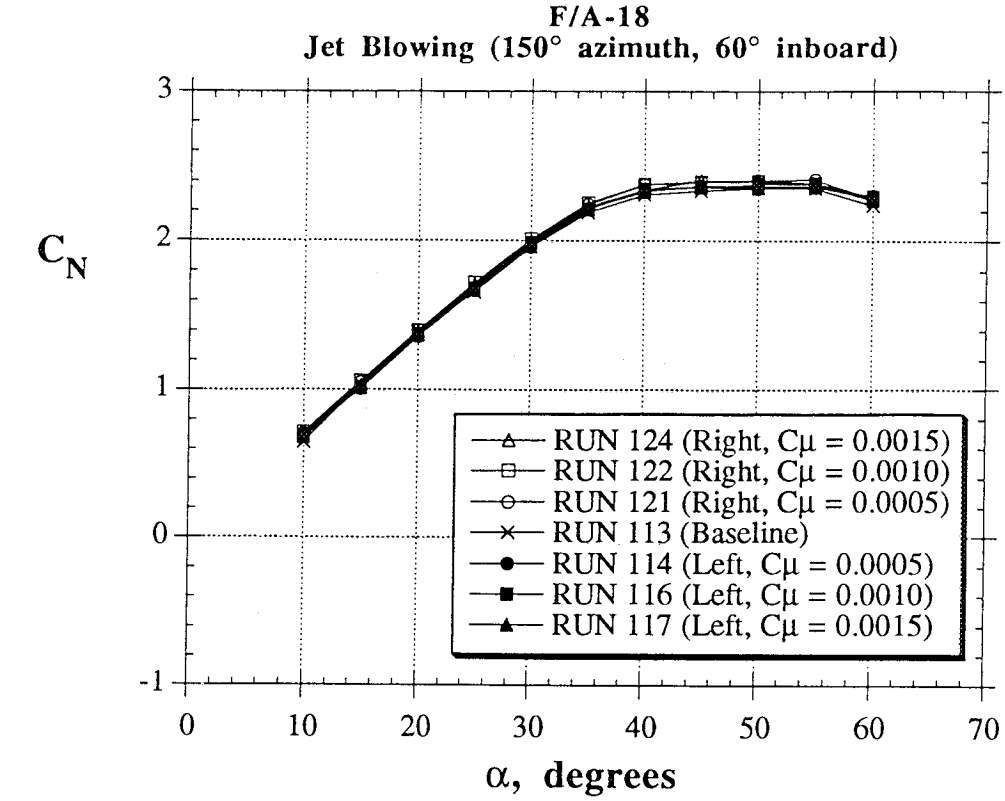

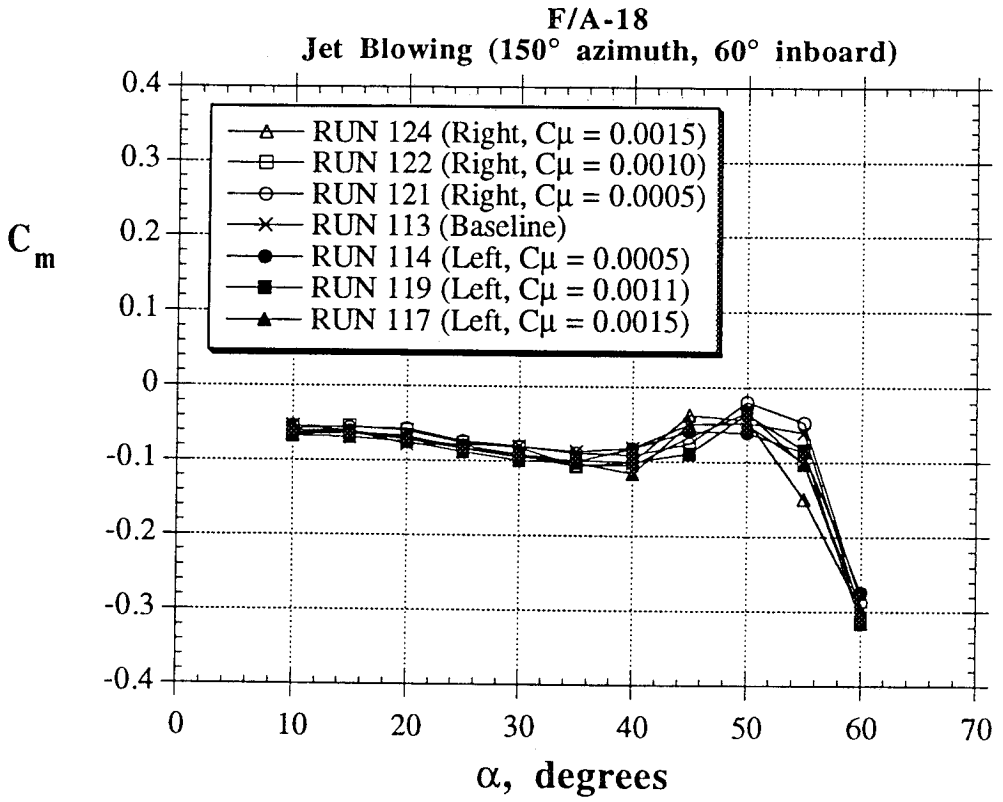

Figure 48 - Effect of Jet Blowing (60° inboard) on the F/A-18 Model (Comparisons to Wind Tunnel Test, Ref. 14)

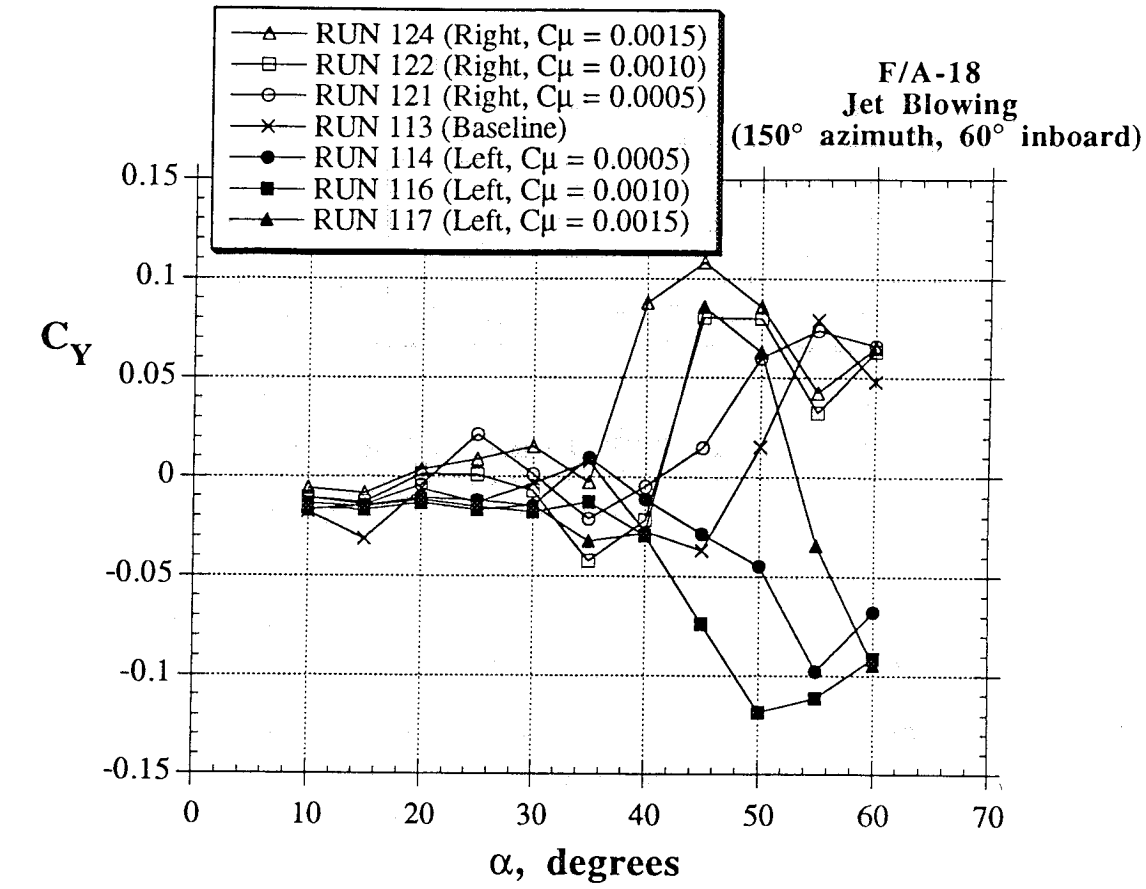

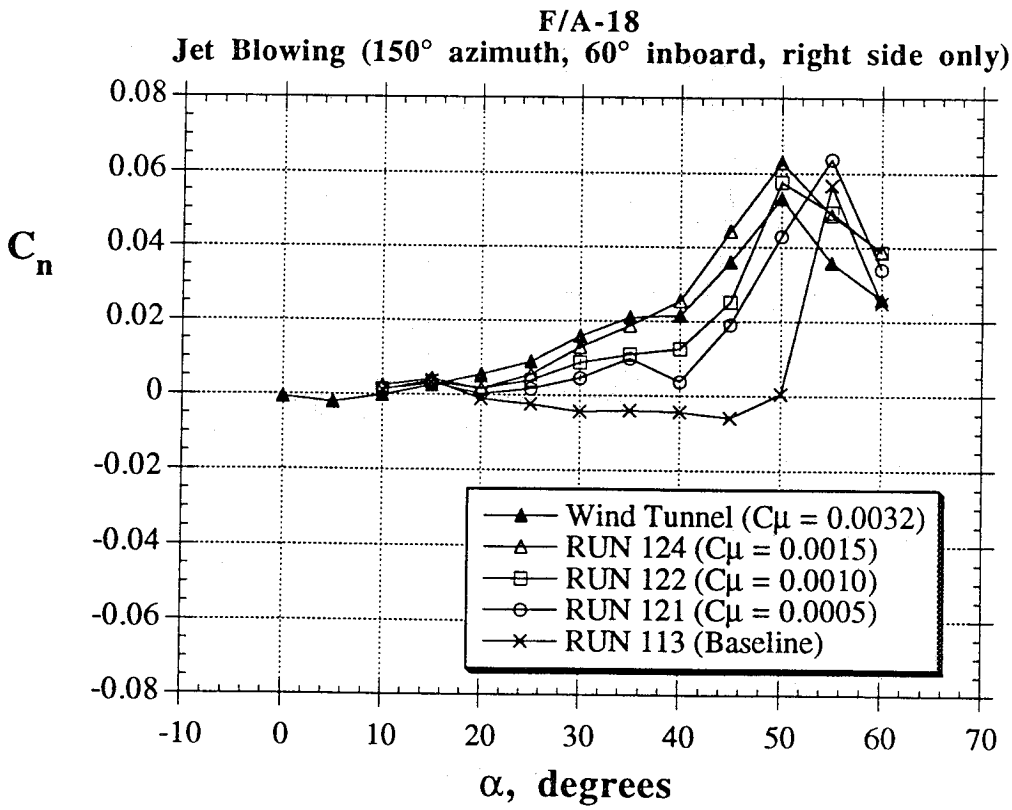

Figure 48 - Continued

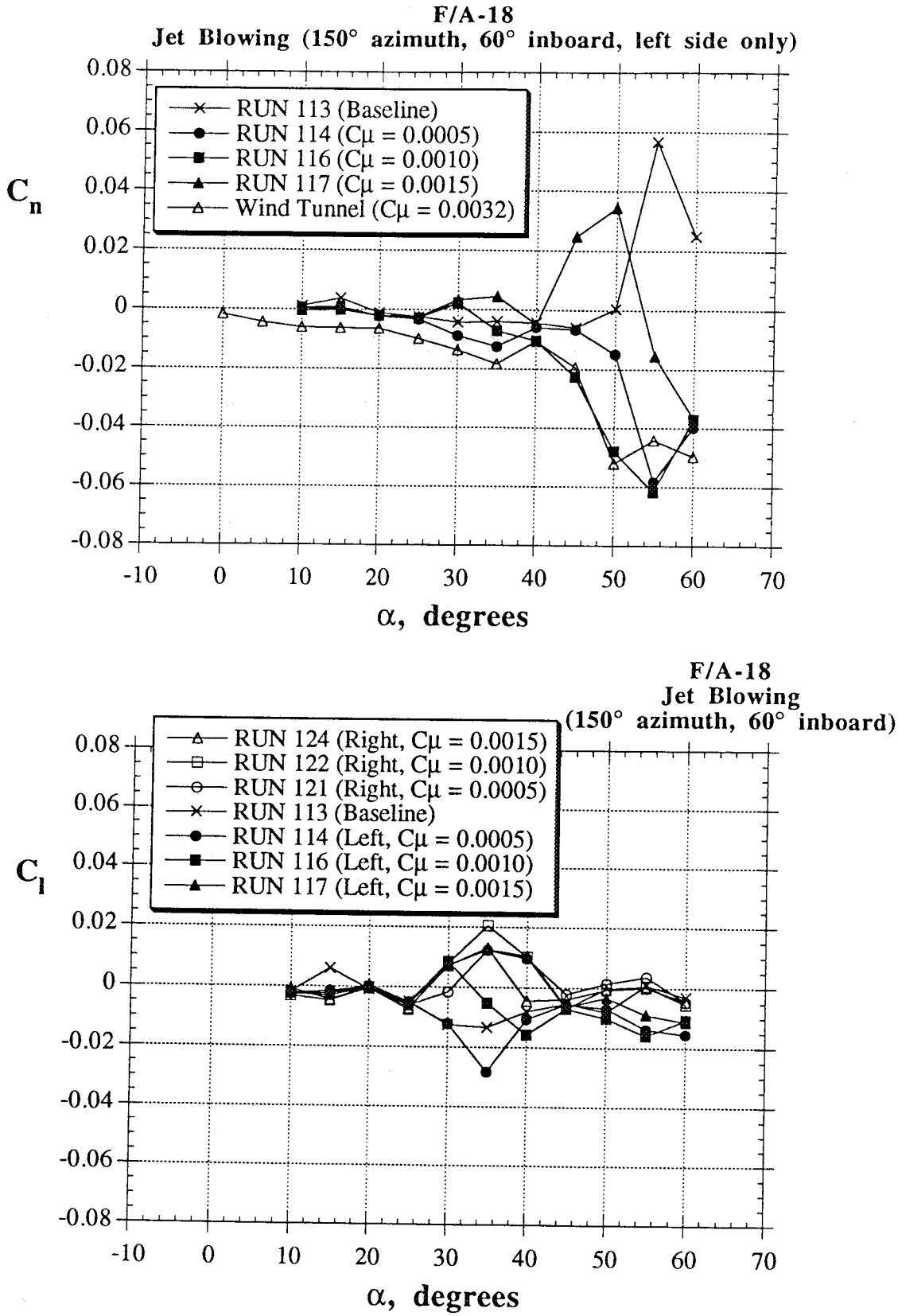

Figure 48 - Concluded

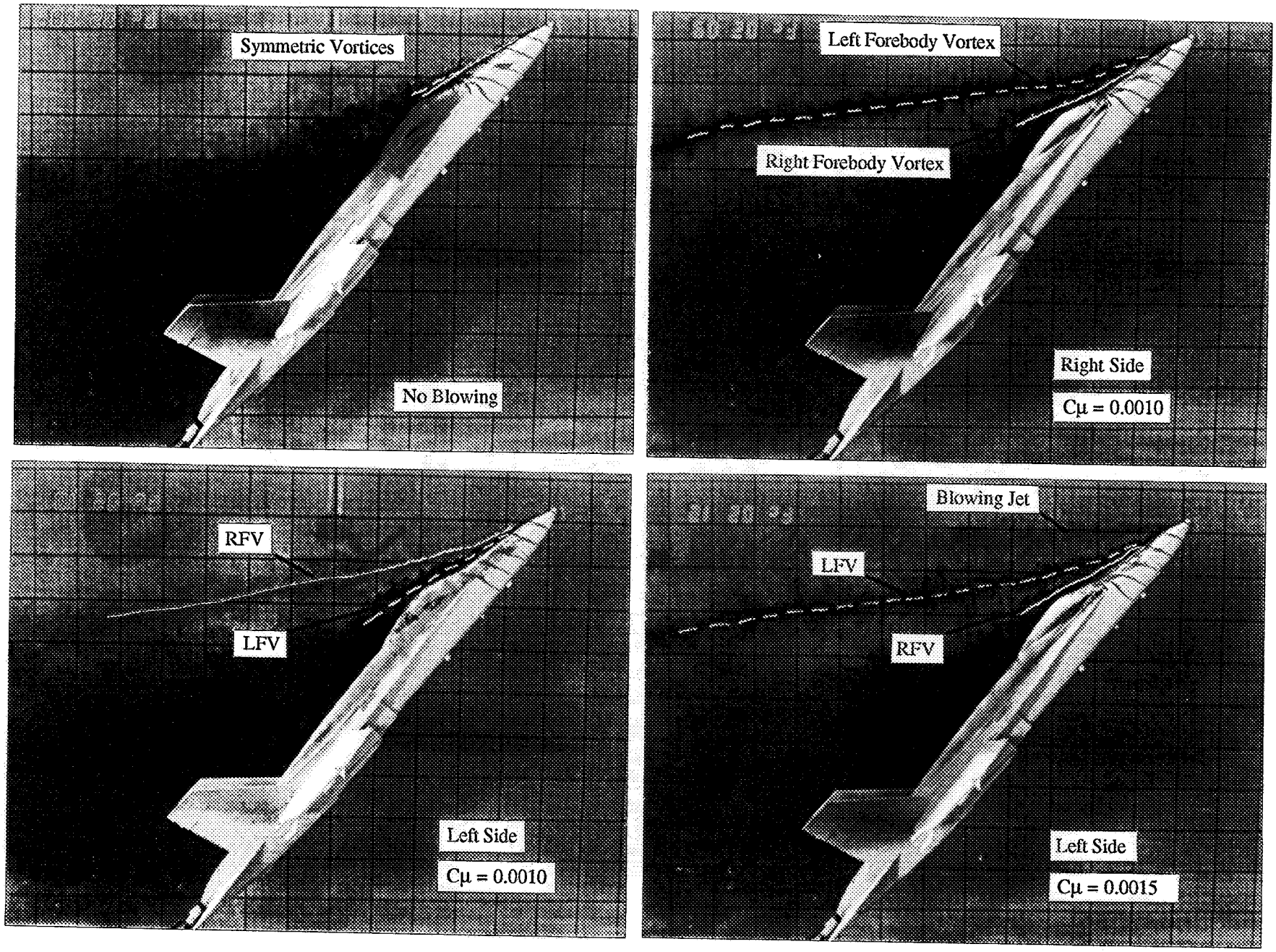

Figure 49 - Flow Visualization of Jet Blowing Effects ($\alpha = 50°$)

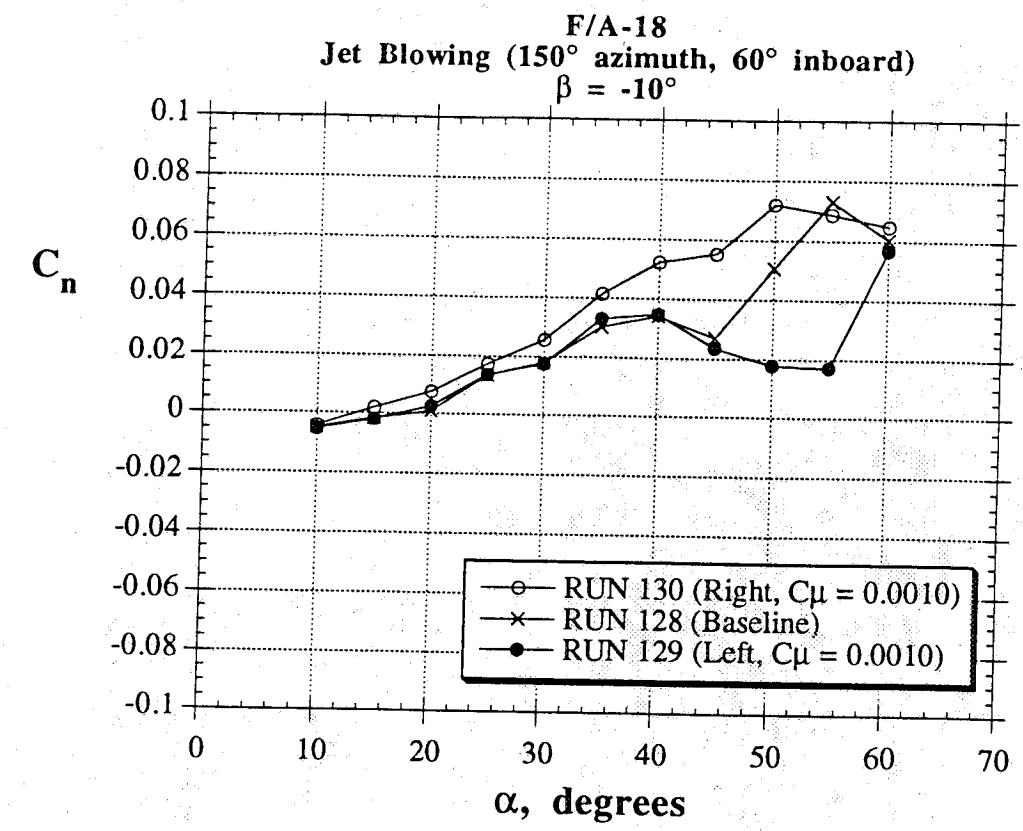

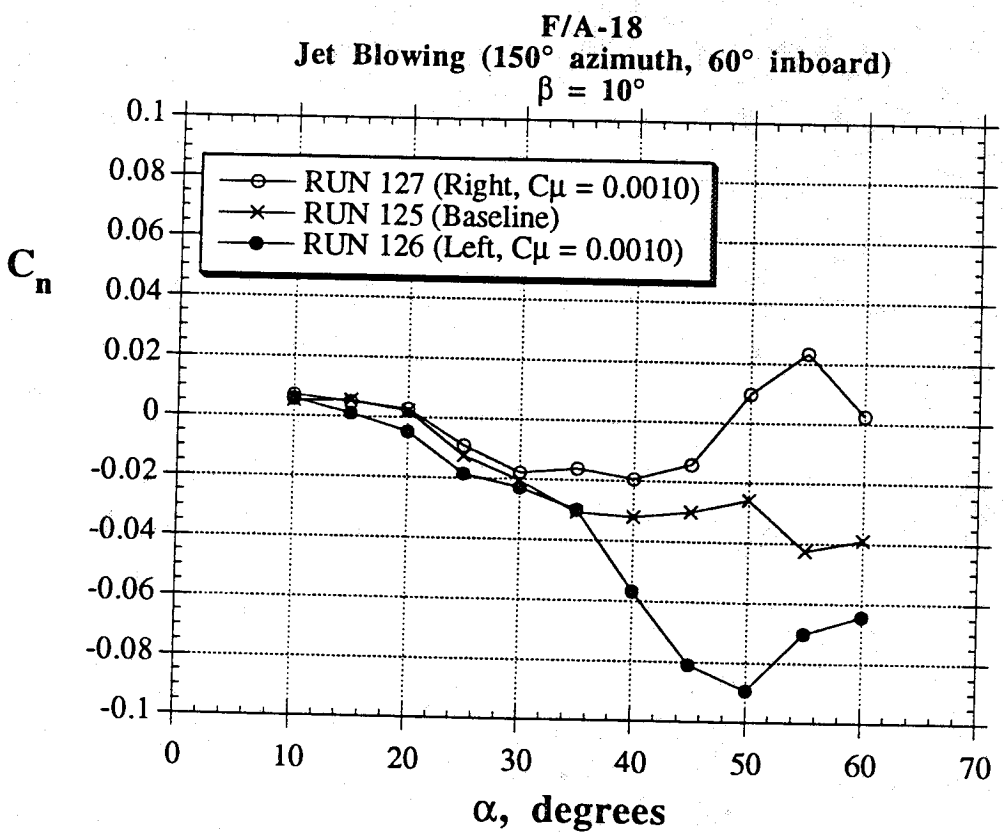

Figure 50 - Effect of Jet Blowing (60° inboard) on the F/A-18 Model at $\beta = \pm 10°$

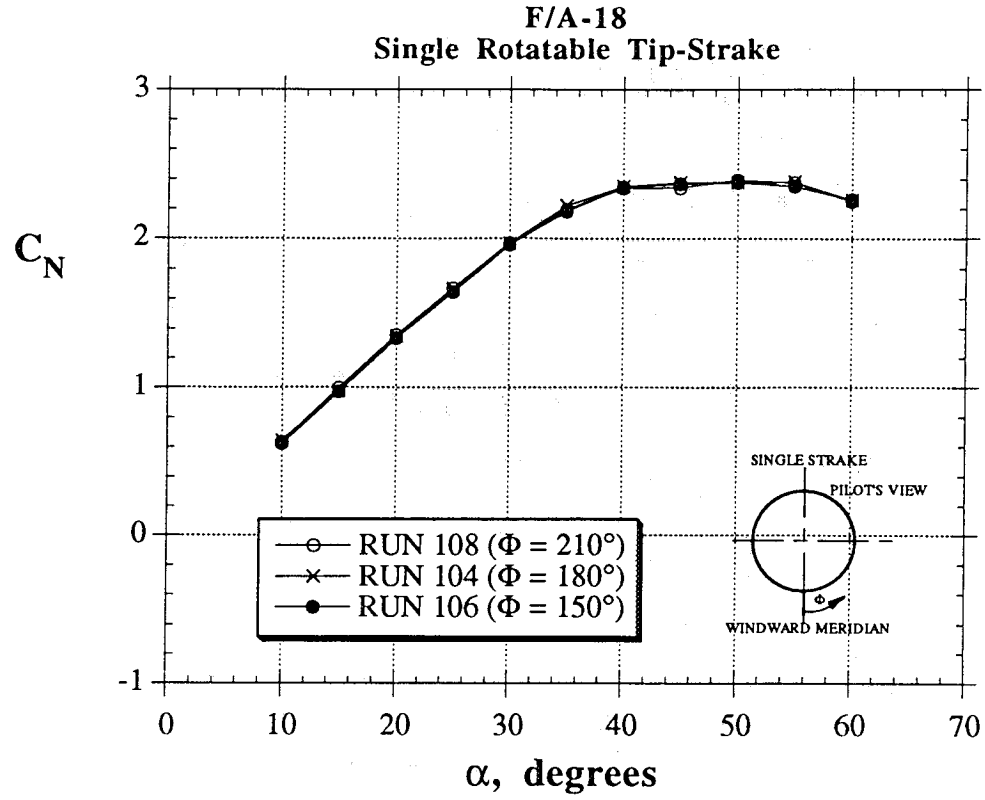

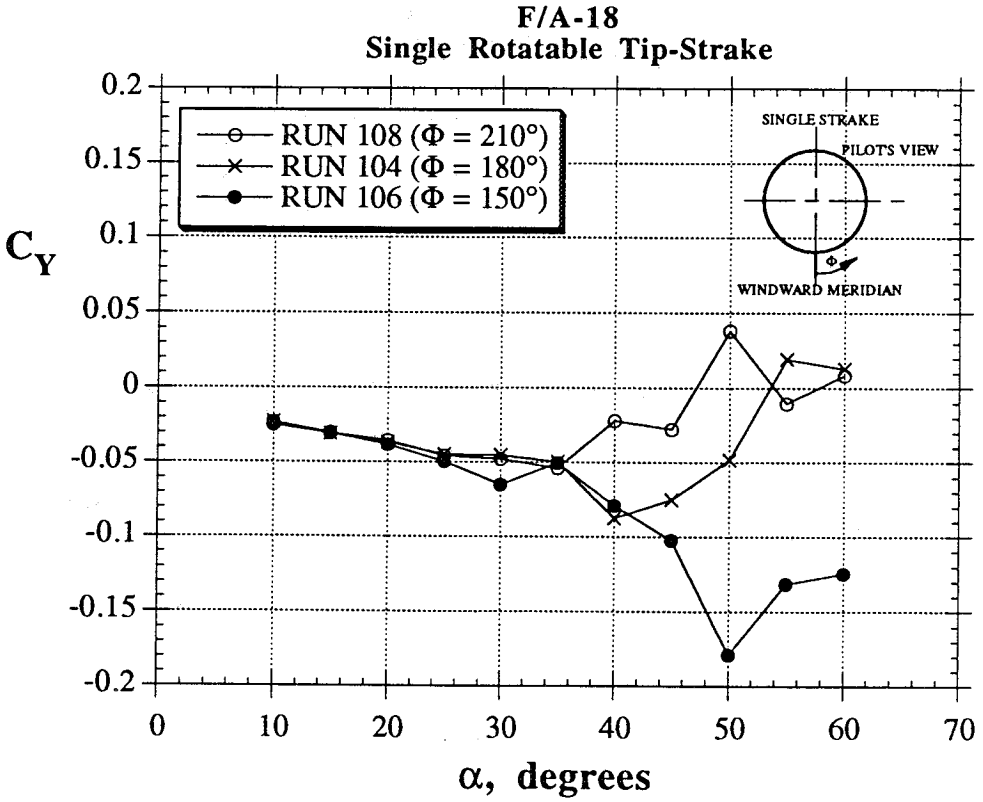

Figure 51 - Effect of Rotating a Single Tip-Strake on the F/A-18 (Comparisons to Wind Tunnel Test, Ref. 15)

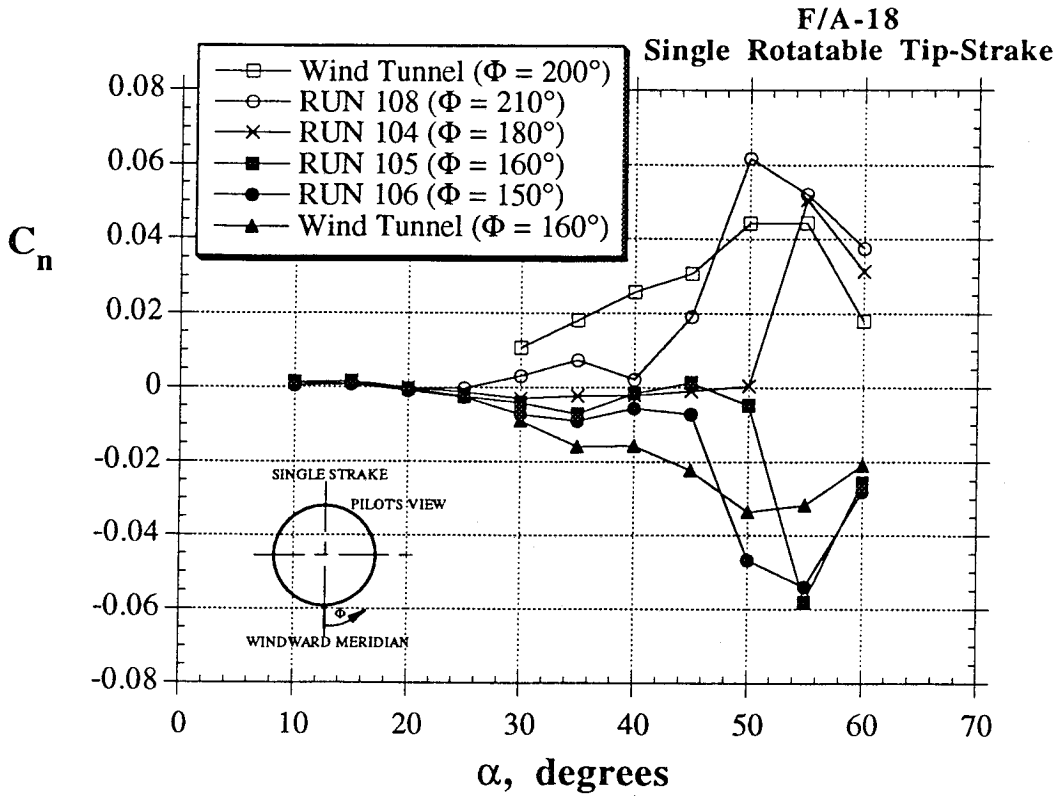

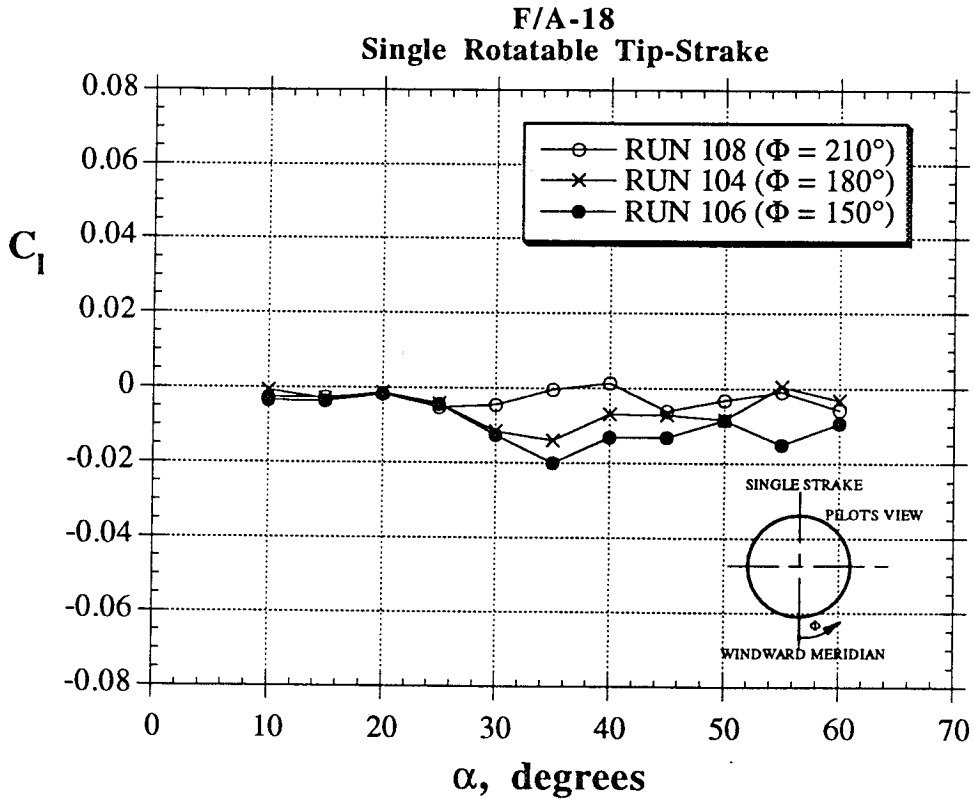

Figure 51 - Concluded

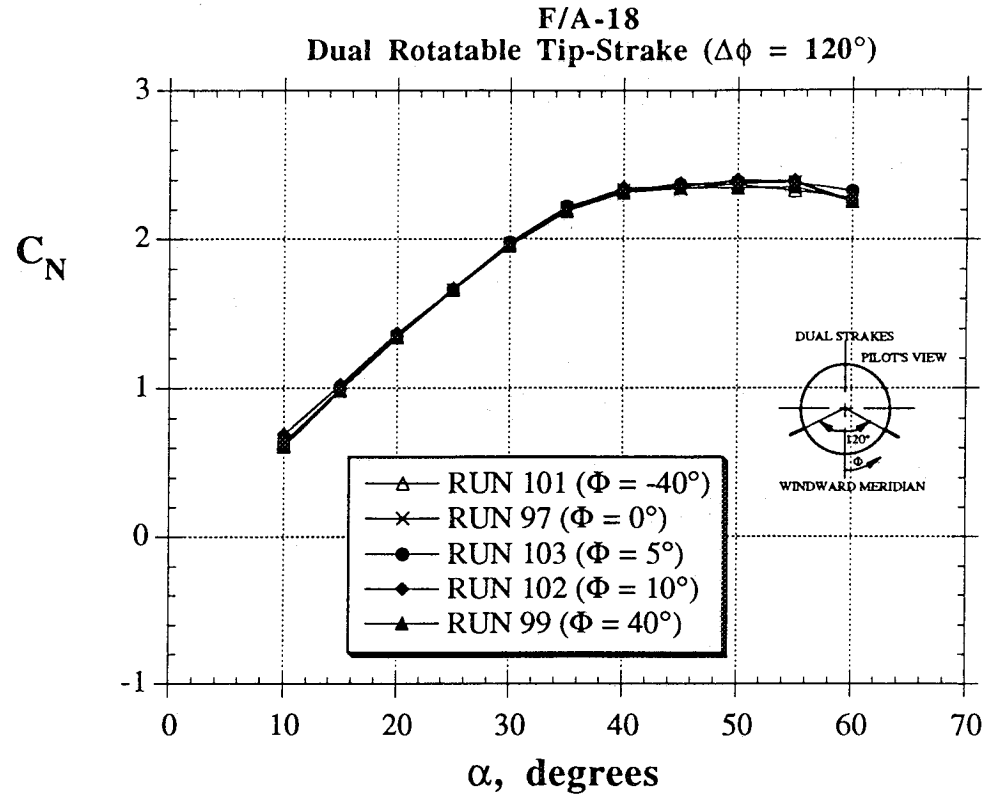

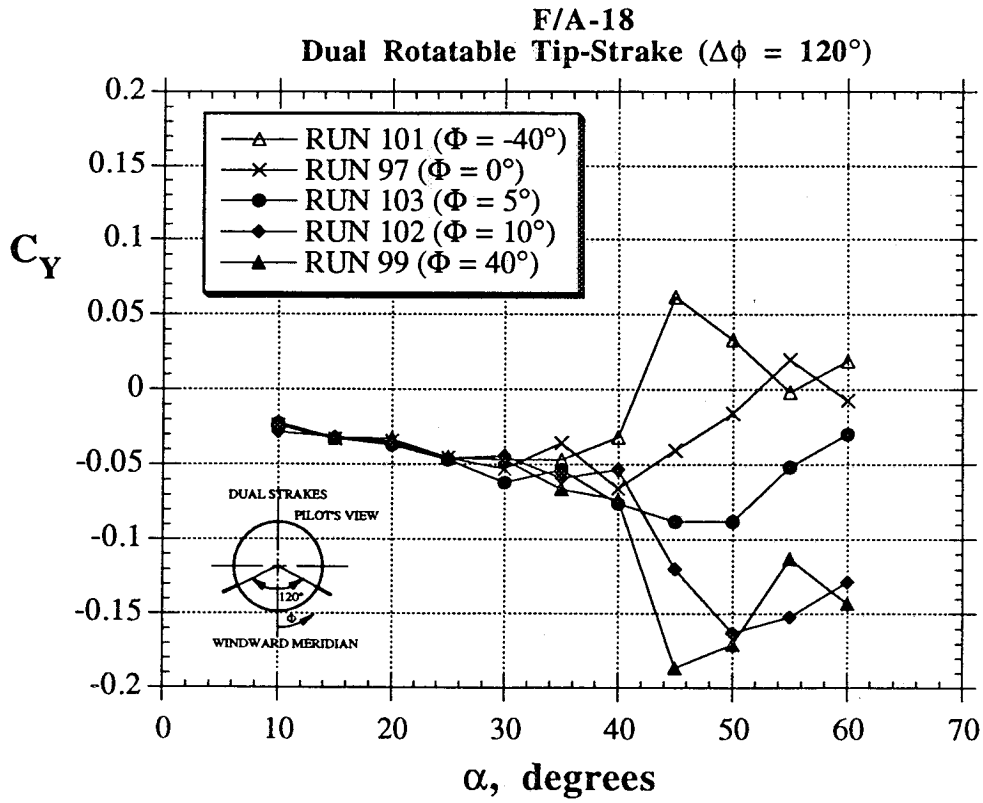

Figure 52 - Effect of Rotating Dual Tip-Strakes (ΔΦ = 120°) on the F/A-18 (Comparisons to Wind Tunnel Test, Ref. 15)

C-2

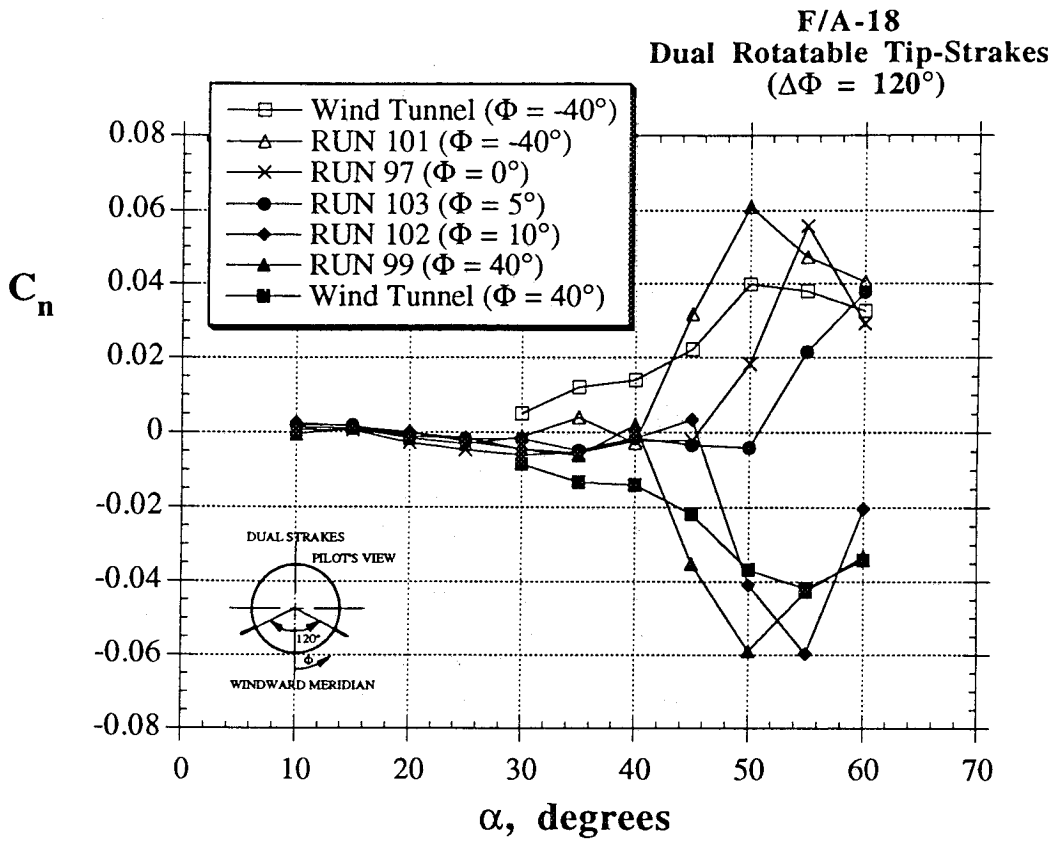

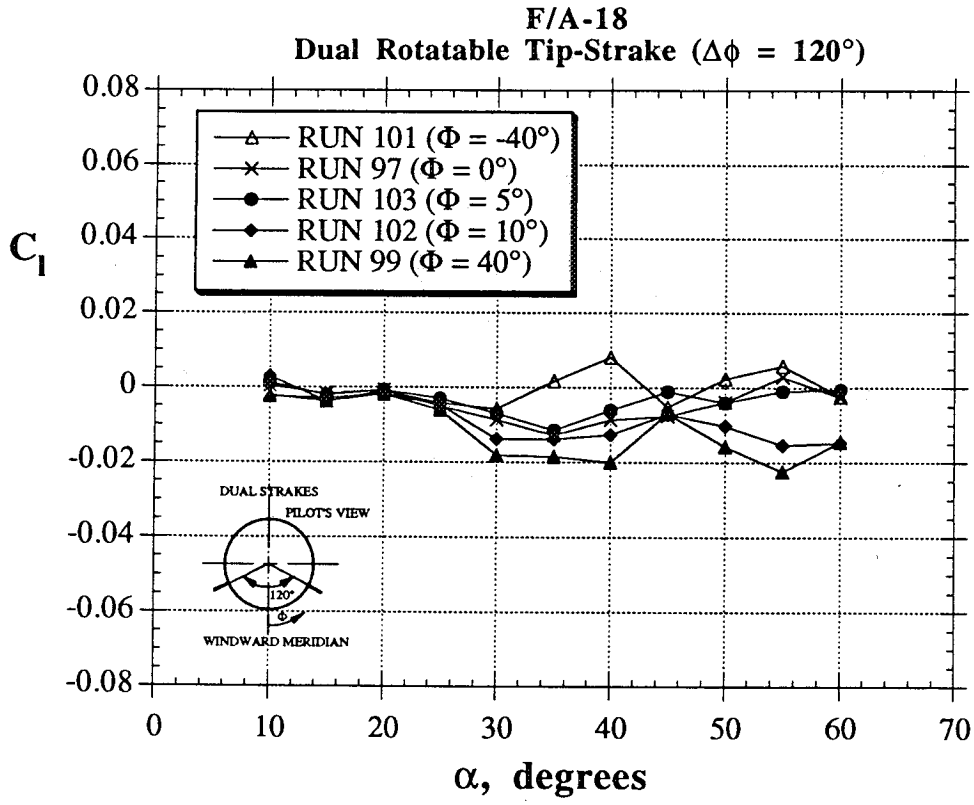

Figure 52 - Concluded

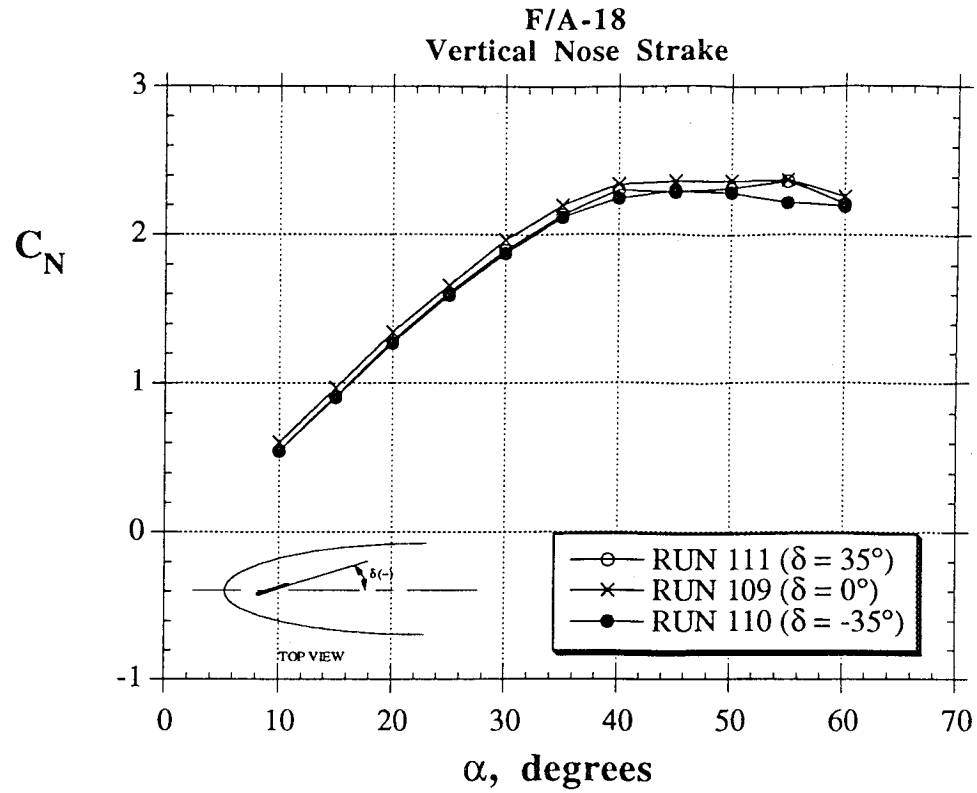

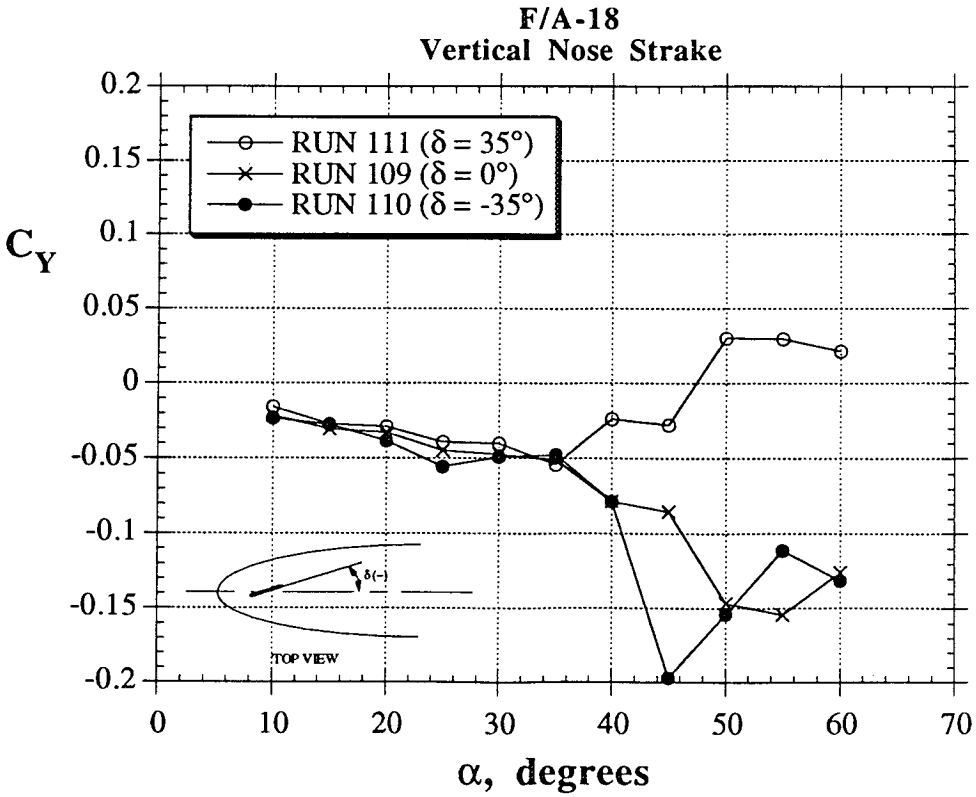

Figure 53 - Effect of Deflecting a Vertical Nose Strake on the F/A-18 (Comparisons to Wind Tunnel Test, Ref. 16)

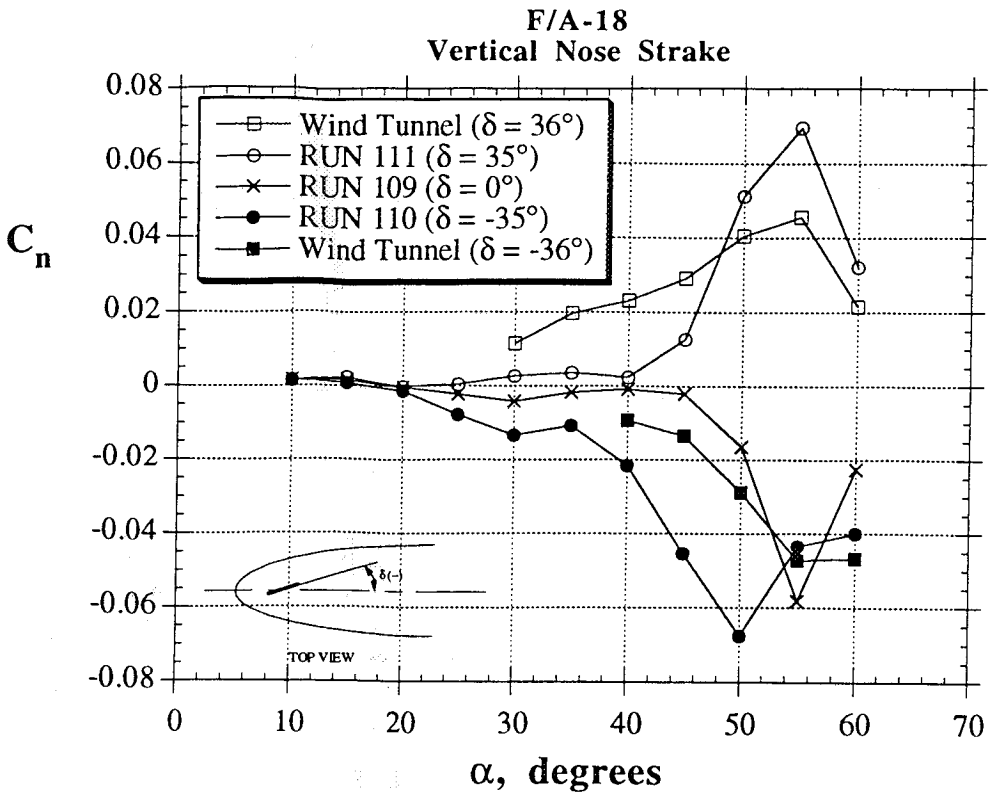

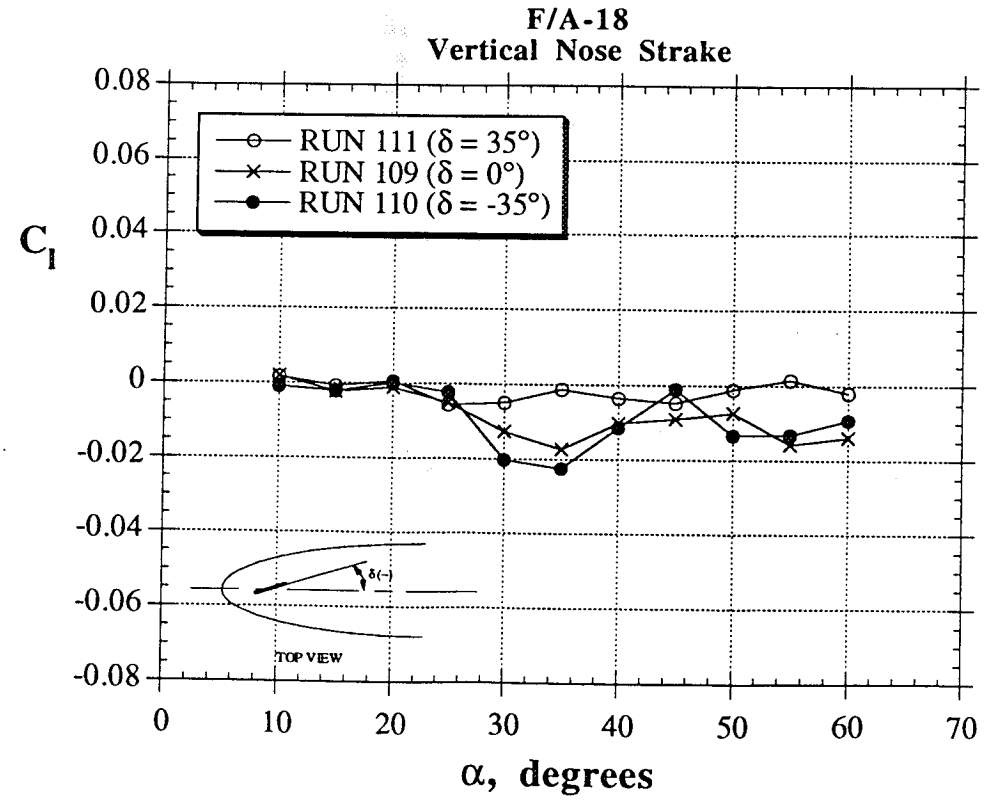

Figure 53 - Concluded

10.0 REFERENCES

1. Erickson, G. E., Peake, D. J., Del Frate, J., Skow, A. M., and Malcolm, G. N., "Water Facilities in Retrospect and Prospect - an Illuminating Tool for Vehicle Design," NASA TM 89409, November 1986.

2. Deane, J. R., "Wind and Water Tunnel Investigations of the Interaction of Body Vortices and the Wing Panels of a Missile Configuration," AGARD CP-2467, Jan. 1979.

3. Thompson, D. H., "A Water Tunnel Study of Vortex Breakdown Over Wings with Highly Swept Leading Edges," ARL/A-Note-356, Melbourne, May 1975.

4. Davies, A. G., "A Comparative Study of Vortex Flows in Wind and Water Tunnels," presented at the AGARD Fluid Dynamics Panel Symposium on Aerodynamic and Related Hydrodynamic Studies Using Water Facilities, October 1986.

5. Cunningham, A., "Steady and Unsteady Force Testing of Fighter Aircraft Models in a Water Tunnel," AIAA Paper 90-2815, presented at the AIAA 8th Applied Aerodynamics Conference, Portland, Oregon, Aug. 20-22,1990.

6. Malcolm, G.N. and Nelson, R.C., "Comparison of Water and Wind Tunnel Flow Visualization Results on a Generic Fighter Configuration at High Angles of Attack," AIAA Paper 87-2423, presented at the AIAA Atmospheric Flight Mechanics Conference, Monterey, CA, Aug. 1987.

7. Suárez, C. J., Ayers, B. F. and Malcolm, G. N., "Development of a Multiple-Component Force and Moment Balance for Water Tunnel Applications (Phase I)," Eidetics TR91-010, September 1991.

8. Wentz, W. H. Jr., "Wind Tunnel Investigations of Vortex Breakdown on Slender Sharp-Edged Wings," Ph.D. Dissertation, University of Kansas, Lawrence, KS.

9. Phillis, D.L., "Force and Pressure Measurements Over a 70° Delta Wing at High Angles of Attack and Sideslip," Master Thesis, Aeronautical Engineering Department, The Wichita State University, 1991.

10. Brandon, J. M. and Shah, G. H., "Effect of Large Amplitude Pitching Motions on the Unsteady Aerodynamic Characteristics of Flat-Plate Wings," AIAA Paper 88-4331, presented at the Atmospheric Flight Mechanics Conference, August 15-17, 1988.

11. Sprage, R., "Wind Tunnel & Water Channel High Angle of Attack Delta Wing Study and Comparison with Particular Reference to Vortex Core & Burst Location," Master Thesis, Aeronautical Engineering Department, The Wichita State University, August 1989.

12. Levin, D. and Katz, J., "Dynamic Load Measurements with Delta Wings Undergoing Self-Induced Roll-Oscillations," AIAA Paper 82-1320, presented at the AIAA 9th Atmospheric Flight Mechanics Conference, 1982.

13. Grismer, D. S., "An Experimental Study of the Steady and Unsteady Aerodynamics of Double Delta Wings for Zero and Non-zero Sideslip," Ph.D. Dissertation, University of Notre Dame, May 1994.

14. Kramer, B. R., Suárez, C. J., and Malcolm, G. N., "Forebody Vortex Control With Jet And Slot Blowing On An F/A-18," AIAA Paper 93-3449, presented at the 11th Applied Aerodynamics Conference, Monterey, California, Aug. 10-12, 1993.

15. Suárez, C. J., Kramer, B. R., and Malcolm, G. N., "Forebody Vortex Control On An F/A-18 Using Small, Rotatable Tip-Strakes," AIAA Paper 93-3450, presented at the 11th Applied Aerodynamics Conference, Monterey, California, Aug. 10-12, 1993.

16. Kramer, B. R., Suárez, C. J., Malcolm, G. N. and Ayers, B. F., "F/A-18 Forebody Vortex Control," Eidetics TR-93-003, Volume I (Static Tests), April 1993.

17. Lanser, W. R. and Murri, D. G., "Wind Tunnel Measurements on a Full-Scale F/A-18 With Forebody Slot Blowing or Forebody Strakes," AIAA Paper 93-1018, presented at the AIAA/AHS/ASEE Aerospace Design Conference, Irvine, CA, 1993.

18. Erickson. G. E., Hall, R. M, et. al., "Experimental Investigation of the F/A-18 Vortex Flows at Subsonic Through Transonic Speeds," AIAA Paper 89-2222 (invited), presented at the AIAA 7th Applied Aerodynamics Conference, Seattle, WA, 1989.

19. Brandon, J. M. and Shah, G. H., "Unsteady Aerodynamic Characteristics of a Fighter Model Undergoing Large-Amplitude Pitching Motions at High Angles of Attack," AIAA Paper 90-0309, 28th Aerospace Sciences Meeting, January, 1990, Reno, Nevada.

20. Ng, T. T., Malcolm, G.N., "Aerodynamic Control of the F/A-18 Using Forebody Vortex Control," AIAA Paper 91-0618, presented at the 29th Aerospace Sciences Meeting, Reno, NV, 1991.

REPORT DOCUMENTATION PAGE

Form Approved
OMB No. 0704-0188

1. AGENCY USE ONLY (Leave blank)	2. REPORT DATE	3. REPORT TYPE AND DATES COVERED
	December 1994	Contractor Report

4. TITLE AND SUBTITLE

Development of a Multicomponent Force and Moment Balance for Water Tunnel Applications, Volume I

5. FUNDING NUMBERS

WU 505-5-953
NAS2-13571

6. AUTHOR(S)

Carlos J. Suárez, Gerald N. Malcolm, Brian R. Kramer, Brooke C. Smith, Bert F. Ayers

7. PERFORMING ORGANIZATION NAME(S) AND ADDRESS(ES)

Eidetics International, Inc.
3415 Lomita Blvd.
Torrance, California 90505

8. PERFORMING ORGANIZATION REPORT NUMBER

H-2030

9. SPONSORING/MONOTORING AGENCY NAME(S) AND ADDRESS(ES)

National Aeronautics and Space Administration
Washington, DC 20546-0001

10. SPONSORING/MONITORING AGENCY REPORT NUMBER

NASA CR-4642

11. SUPPLEMENTARY NOTES

NASA Technical Monitor John Del Frate.

12a. DISTRIBUTION/AVAILABILITY STATEMENT

SBIR
Unclassified—Unlimited
Subject Category 34

12b. DISTRIBUTION CODE

13. ABSTRACT (Maximum 200 words)

The principal objective of this research effort was to develop a multicomponent strain gauge balance to measure forces and moments on models tested in flow visualization water tunnels. An internal balance was designed that allows measuring normal and side forces, and pitching, yawing and rolling moments (no axial force). The five-components to applied loads, low interactions between the sections and no hysteresis. Static experiments (which are discussed in this Volume) were conducted in the Eidetics water tunnel with delta wings and a model of the F/A-18. Experiments with the F/A-18 model included a thorough baseline study and investigations of the effect of control surface deflections and of several Forebody Vortex Control (FVC) techniques. Results were compared to wind tunnel data and, in general, the agreement is very satisfactory. The results of the static tests provider confidence that loads can be measured accurately in the water tunnel with a relatively simple multicomponent internal balance. Dynamic experiments were also performed using the balance, and the results are discussed in detail in Volume II of this report.

14. SUBJECT TERMS

Static and dynamic experiments; Water tunnel force/moment balance

15. NUMBER OF PAGES

101

16. PRICE CODE

A06

17. SECURITY CLASSIFICATION OF REPORT	18. SECURITY CLASSIFICATION OF THIS PAGE	19. SECURITY CLASSIFICATION OF ABSTRACT	20. LIMITATION OF ABSTRACT
Unclassified	Unclassified	Unclassified	Unlimited

Available from the NASA Center for AeroSpace Information, 800 Elkridge Landing Road, Linthicum Heights, MD 21090; (301)621-0390